Investigation of an Aeroelastic Model for a Generic Wing Structure

by

M.E. Cilliers

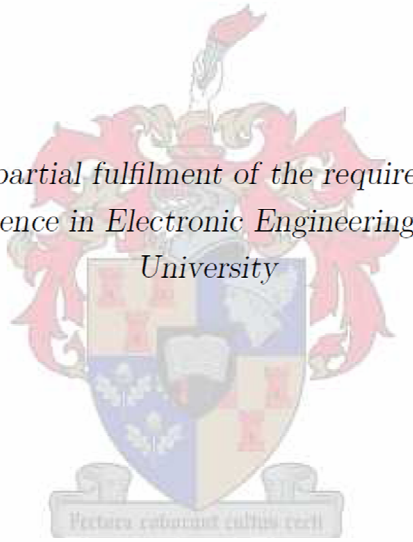

Thesis presented in partial fulfilment of the requirements for the degree of Master of Science in Electronic Engineering at Stellenbosch University

Supervisor: Prof T. Jones

Department of Electrical and Electronic Engineering,
University of Stellenbosch,
Private Bag X1, Matieland 7602, South Africa.

March 2013

Declaration

By submitting this thesis electronically, I declare that the entirety of the work contained therein is my own, original work, that I am the sole author thereof (save to the extent explicitly otherwise stated), that reproduction and publication thereof by Stellenbosch University will not infringe any third party rights and that I have not previously in its entirety or in part submitted it for obtaining any qualification.

Date: March 2013

Abstract

Investigation of an Aeroelastic Model for a Generic Wing Structure

M.E. Cilliers

Department of Electrical and Electronic Engineering,
University of Stellenbosch,
Private Bag X1, Matieland 7602, South Africa.

Thesis: MScEng (Electronic)

October 2012

Computational Aeroelasticity is a complex research field which combines structural and aerodynamic analyses to describe a vehicle in flight. This thesis investigates the feasibility of including such an analysis in the development of control systems for unmanned aerial vehicles within the Electronic Systems Laboratory at the Department of Electrical and Electronic Engineering at Stellenbosch University.

This is done through the development of a structural analysis algorithm using the Finite Element Method, an aerodynamic algorithm for Prandtl's Lifting Line Theory and experimental work. The experimental work was conducted at the Low-Speed Wind Tunnel at the Department of Mechanical and Mechatronic Engineering.

The structural algorithm was applied to 20-noded hexahedral elements in a wing-like structure. The wing was modelled as a cantilever beam, with a fixed and a free end. Natural frequencies and deflections were verified with the experimental model and commercial software.

The aerodynamic algorithm was applied to a Clark-Y airfoil with a chord of 0.1 m and a half-span of 0.5 m. This profile was also used on the experimental model.

Experimental data was captured using single axis accelerometers. All post-processing of data is also discussed in this thesis. Results show good correlation between the structural algorithm and experimental data.

Uittreksel

Ondersoek van 'n Aëroelastiese Model vir 'n Generiese Vlerk Struktuur

("Investigation of an Aeroelastic Model for a Generic Wing Structure")

M.E. Cilliers

Departement Elektries en Elektronies Ingenieurswese,
Universiteit van Stellenbosch,
Privaatsak X1, Matieland 7602, Suid Afrika.

Tesis: MScIng (Elektronies)

Oktober 2012

Numeriese Aeroelastisiteit is 'n komplekse navorsingsveld waar 'n vlieënde voertuig deur 'n strukturele en 'n aerodinamiese analise beskryf word. Hierdie tesis ondersoek die toepaslikheid van hierdie tipe analise in die ontwerp van beheerstelsels vir onbemande voertuie binne die ESL groep van die Departement Elektriese en Elektroniese Ingenieurswese by Stellenbosch Universiteit.

Die ondersoek bevat die ontwikkeling van 'n strukturele algoritme met die gebruik van die Eindige Element Methode, 'n aerodinamiese algoritme vir Prandtl se Heflynteorie en eksperimentele werk. Die eksperimentele werk is by die Department Meganiese en Megatroniese Ingensierswese toegepas in die Lae-Spoed Windtonnel.

Die strukturele algoritme maak gebruik van 'n 20-nodus heksahedrale element om 'n vlerk-tipe struktuur op te bou. Die vlerk is vereenvouding na 'n kantelbalk met 'n vasgeklemde en 'n vrye ent. Natuurlike frekwensies en defleksies is met die eksperimentele werk en kommersiële sagteware geverifieer.

Die aerodinamiese algoritme is op 'n Clark-Y profiel met 0.1 m koord lengte en 'n halwe vlerk length van 0.5 m geïmplementeer. Die profiel is ook in die eksperimentele model gebruik.

Die eksperimentele data is met eendimensionele versnellingsmeters opgeneem. Al die verdere berekeninge wat op ekperimentele data gedoen is, word in die tesis beskryf. Resultate toon goeie korrelasie tussen die strukturele algoritme en die eksperimentele data.

Acknowledgements

I would like to express my sincere gratitude to the following people and organisations. To Professor Thomas Jones for his role as study leader. To the late Professor Gerrie Thiart for his role as co-supervisor for the first two years on this project and his help with the aerodynamic components of this project. Mr Cobus Zietsman for his assistance at the Department of Mechanical and Mechatronic Engineering Low-speed Wind Tunnel. Mr Wessel Croukamp for his help building the experimental Model. Mr Ruan De Hart for his help with the electronics on the experimental model. Lastly I would like to thank friends and family for their support and encouragement for the duration of this project.

Contents

List of Figures

List of Tables

List of Algorithms

Nomenclature

Constants

$\pi =$ 3.141592654

e = 2.718281828

Variables - Latin

f	Frequency	[Hz]
f_s	Sampling frequency	[Hz]
t	Thickness	[m]
x	Coordinate or Displacement	[m]
$\dot{x}$	Velocity	[m/s]
$\ddot{x}$	Acceleration	[m/s^2]
u,v,w	Components of displacement of an arbitrary material point	[m]
E	Young's Modulus	[Pa]
G	Shear Modulus	[Pa]
I	Moment of Inertia of cross-sectional area	[m^4]
N	Shape Function	
P	Pressure	[Pa]
Q	Resolution	
$Re_{\,\mathrm{D}}$	Reynolds number with diameter as a reference length	
U	Displacement Vector	[m]
$\dot{U}$	Velocity Vector	[m/s]
$\ddot{U}$	Acceleration Vector	[m/s^2]
U_c	Overall Instrument Error	
V	Velocity	[m/s]
V_∞	Freestream Velocity	[m/s]
t	Time	[sec]

B	Strain-Displacement Matrix	
D	Damping Matrix	
E	Stress-Strain Matrix	[Pa]
F	Force Vector	[N]
J	Jacobian Matrix	
K	Stiffness Matrix	
M	Consistent Mass Matrix	
N	Element shape or interpolation function matrix	

Variables - Greek

α	Angle of Attack	[deg]
ξ,η,ζ	"Natural" Coordinates, used for Isoparametric Elements	
ν	Poisson's Ratio	
θ	Rotation angle	[rad]
τ	Moment	[N · m]
ρ	Mass Density	[kg/m^3]
ω	Natural frequency	[Hz]

Superscripts

X^{-1}	Matrix Inverse
X^{T}	Matrix Transpose

Abbreviations

AOA	Angle of attack
AVL	Athena Vortex Lattice
CoX	Centre of Expertise
DOF	Degrees of Freedom
ESL	Electronic Systems Laboratory
FDM	Finite Difference Method
FEM	Finite Element Method
FVM	Finite Volume Method
PSD	Power Spectral Density
SU	Stellenbosch University
UAV	Unmanned Aerial Vehicle
VLM	Vortice Lattice Method

Chapter 1

Introduction

This thesis describes the theoretical and experimental work that has been completed as required by the degree Master of Science in Electrical and Electronic Engineering. The aim of this project is to investigate the rigid body approximations currently used for the development of control systems for unmanned aerial vehicles (UAV's) and the feasibility of replacing them with more accurate aeroelastic approximations, specifically for the wing structure. The aeroelastic problem is to be broken up into structural and the aerodynamic components which, when combined loosely, will result in an aeroelastic model. This report documents all phases of the project, from Literature Study to Experimental Verification. This chapter provides an introduction to the project and describes the motivation and key objectives of the project.

1.1 Motivation

This project is to be developed in the Electronic Systems Laboratory (ESL) at the Department of Electrical and Electronic Engineering at Stellenbosch University. Within the ESL, a group called the CoX (Centre of Expertise) in Autonomous Systems, focuses on complex embedded control, automation and information systems. To be able to achieve their goal of autonomous control, a mathematical model of the system or plant that is to be controlled has been created. Currently, projects involving unmanned aircraft use a rigid body assumption. While this approach has been sufficient for preliminary studies, it has been decided that a more accurate model of the aircraft dynamics would expand the capabilities of CoX which will in turn lead to higher fidelity control systems.

There are commercial packages available that either perform an aerodynamic analysis or a structural analysis, each a complex research field on their own. However, the interactions on a wing-like structure are not independent. The aim of this project is to investigate the feasibility of combining these two analysis types into a single

mathematical model that takes the flexibility of the wing into consideration when performing analyses and developing control systems.

Under flight conditions, aerodynamic forces are applied to the wing structure in the form of lift and drag. If we assume the wing can be simplified into a cantilever beam, it is clear that the lift and drag forces will cause a deflection in the wing structure, i.e. the structure is not rigid. These deflections lead to a change in angle of attack, which will in turn lead to a change in the lift and drag forces. This interaction of force and deflection makes the problem a dynamic aeroelastic one and leads to the conclusion that a replacement of the currently used rigid body assumptions is, therefore, a valid step in the advancement of the University's capabilities.

1.2 Objectives

This section describes the various phases that were proposed for the project. Each phase can be described as a unit with its own set of aims and results. Where necessary the appropriate chapter and section in the remainder of this document will be indicated, where further discussion of the phase can be found.

Literature Study The aim of the literature study is to gather knowledge from a variety of fields and consolidate the information so as to influence the project in a constructive and positive way. There are a number of topics that were reviewed and where relevant, brought to the attention of the reader in Chapter 2. These topics include the Finite Element Method, Computational Fluid Dynamics, Aerodynamics, Aeroelasticity and Wind-Tunnel Testing.

Implementation of Aeroelastic Equations Once the appropriate aerodynamic and structural equations are identified, by means of the literature study, it is necessary to implement them. The structural and aerodynamic equations are investigated separately to ensure their individual correctness. The environment chosen for the numerical analysis was the program language C. This language can be integrated within the Matlab environment which is the main mathematical tool used in the ESL. The advantages of using C code, instead of creating the simulation in the Matlab environment, include the duration of the simulation and the flexibility to include it in a variety of other platforms. In a typical Finite Element Software package a model may contain many thousands of elements which implies very large matrix manipulations. To this end, the C code would be the most cost effective solution. However, linear algebra matrix manipulations are not embedded in the C code and functions for each type of manipulation will need to be created. Further details regarding the implementation of the aeroelastic equations can be found in Chapters 3 and 4.

Create an Experimentation Plan In order to verify any numerical calculations or simulations, we need to create a guideline or experimental plan for the execution of any experimental work. This will ensure safe testing methods and that all the necessary data about the defining parameters will be gathered.

This plan will include the following

- the building of the experimental model, refer to Section 5.2
- necessary arrangements with the Department of Mechanical and Mechatronic Engineering for the use of their wind tunnel facilities
- the choice of desired parameters that are to be characterised, refer to Section 5.2.2
- the calibration of equipment and the procedures for each specific experiment, refer to Section 5.4

Obtain Test Data This phase refers to the implementation of the Experimentation Plan. The raw data obtained needs to be reduced to usable parameters. They should also be in a form that can easily be used to verify the numerical simulation results. Techniques used for data reduction can be seen in Section 5.5 while verification of the results with the numerical solutions can be seen in Chapter 6.

Verify Results of Experimentation and Code The comparison of the experimental results with the solution from the simulation should prove the implementation of the aeroelastic equations valid. To aid the verification process, the model being analysed numerically should be the same as that used during experimentation [5]. The test example and results can be found in Chapter 6.

A second method that will be used to verify the validity of the simulation, would be to implement the model in a structural analysis code, like Nastran, and an aerodynamic code like AVL. There are also the inherent inaccuracies involved with any numerical simulation that must be considered when using their results as a form of verification.

Chapter 2

Literature Study

2.1 Introduction

At the start of any research project it is necessary to review relevant literature on the chosen topic. The literature study provides a solid basis on which further work and appropriate decisions can be made. This chapter describes some basic concepts that will aid the reader with regard to the context of the research problem and aided the author during various stages in the development of the project. Some topics discussed in this literature study include aeroelasticity, which is sub-divided into a structural and aerodynamic component. Experimental work in general is also discussed.

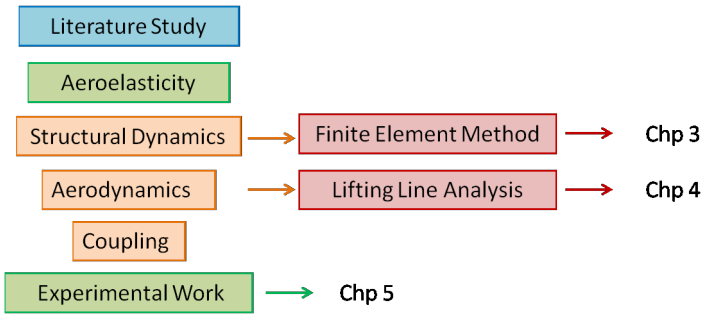

Figure 2.1: Literature Study Information Structure.

2.2 Aeroelasticity

Aeroelasticity is defined as a phenomenon which exhibits appreciable reciprocal interaction (static or dynamic) between aerodynamic forces and the deformations induced thereby in the structure of a flying vehicle, its control mechanisms, or its propulsion

system [6]. An aeroelastic analysis is one that investigates this interaction. Simply put, aeroelasticity is the combination of the structural and aerodynamic components to create a more complete, accurate and realistic model.

Traditionally, aeroelastic behaviour was considered a negative result and research was focused on the avoidance of this type of behaviour. Initial models only considered aerodynamics, and the structures were assumed to be rigid. With the advances in materials technology the shortcomings of the rigid body model become evident with the faster, lighter and more flexible aircraft now in production. The focus in industry has, therefore, shifted from a negative slant to that of a positive one when it became evident that the aeroelastic behaviour can be used to enhance the performance of the vehicle and is a necessary design parameter.

The aeroelastic formulation, or generalised aeroelastic equation of motion [7] is described as follows

$$[\mathbf{M}]\{\ddot{q}(t)\} + [\mathbf{D}]\{\dot{q}(t)\} + [\mathbf{K}]\{q(t)\} = \{\mathbf{F}(t)\} \tag{2.1}$$

with $\mathbf{M}$, $\mathbf{D}$ and $\mathbf{K}$ the mass, damping and stiffness matrices of the structure respectively. The force vector, $\mathbf{F}(t)$, comprises the aerodynamic forces on the wing surface.

Computational aeroelasticity is a complex research field that implements the above equation numerically. As with any computational analysis, there are many aspects that can influence the accuracy of a solution. These can be the simplifications or approximations the user makes when creating the model which lead to limitations in the model. The applicability of the model to the specific type of problem also needs to be assessed. There are many formulations that can be used to solve the aeroelastic equations and the validity of the solver or solution method will need to be quantified. Computational cost versus the accuracy of the solution is another influencing factor in deciding which solution method to use. Finally, the results from the analysis need to be verified with experimental results [8].

A model that is based on rigid body assumptions implies a wide separation between the frequencies of the rigid body modes and the elastic modes of the structure. This often leads to a decoupling of the problem [9]. However, due to the dynamic and complex behaviour of an aerodynamic vehicle, a flutter analysis might be necessary, in which case the rigid body modes and elastic modes cannot be separated.

Flutter is defined by Hancock [10] as the condition when an aircraft component (e.g. wing or tailplane) exhibits self-sustained oscillations at a certain forward speed. Hancock also demonstrates the derivation of the flutter equations. The flutter problem corresponds to an Eigenvalue problem where the solution corresponds to the minimum flight speed that renders the system to transit from stable to unstable mo-

tion [11]. This has lead to the development of two types of aeroelastic models which allow us to analyse the effects of flutter experimentally. The first is a dynamic stability test. The dynamic stability tests look at the dynamic behaviour by rigid body modes of motion. The second model is a flutter test. Flutter tests look mainly at the elastic modes (dynamic instability). The support structure must allow the model to deform elastically without influencing the results. From the experimental data it is possible to determine the period of motion, the time to damp to one-half the amplitude and number of oscillations to damp to one-half amplitude. The flutter analysis is more common than dynamic stability analysis in the low-speed wind-tunnel.

There are many approaches to solving this aeroelastic problem numerically. The method used is dependent on the formulation of the equations describing the system and how the system has been modelled. The first option is to couple the separately defined fluid and structural components which means a reformulation of the defining equations. The complete aeroelastic equation of motion (Equation 2.1) can then be solved simultaneously in a strongly coupled fashion by a fully implicit time-marching method [12]. The Runga-Kutta Method can be used to implement the time-marching. It calculates the differential equation at strategic points and then combines them to give a higher order of accuracy [13]. The Global Newton Method could also be used to solve the system of equations by iteration with modifications to find a solution from any starting value [14]. The Keller-box Finite Difference Scheme is another method of discretizing the fluid-structure problem [15]. One of the basic ideas of the procedure is to write the governing partial differential equations in the form of a first-order system. Then using simple central difference quotients and averages, second order accurate difference equations can be obtained.

Secondly, the aerodynamic and structural components can be kept independent with separate solvers for each environment, however, a suitable interfacing technique or sub-routine is needed to transfer loads [15]. This is only effective for moderate to low aspect ratio wings where the deflections are small and have little effect on the aerodynamic component. The linearised structural deflections are combined with a linear aerodynamic solution. Most commercial codes make use of different computational grids for fluids and structures. Therefore, interpolation of computational grids and aerodynamic loads must be performed. A structural grid is usually made up of a combination of elements and can be related to the aerodynamic grid by using one of a variety of splining methods [12].

The third option is to maintain the two different solvers but couple them into one module, i.e. exchanging information at the boundaries and mapping the information between environments. At this stage the third option is the most appealing due to its modular nature and ease of implementation. It was decided that this would be

the approach taken by the author for this thesis.

Once the aeroelastic behaviour of a structure can be modelled, the information can be used to produce a more efficient lifting surface.

The next sections look at some of the possible analytical solution methods for each of the components, structural and aerodynamic, as well as some interfacing methods.

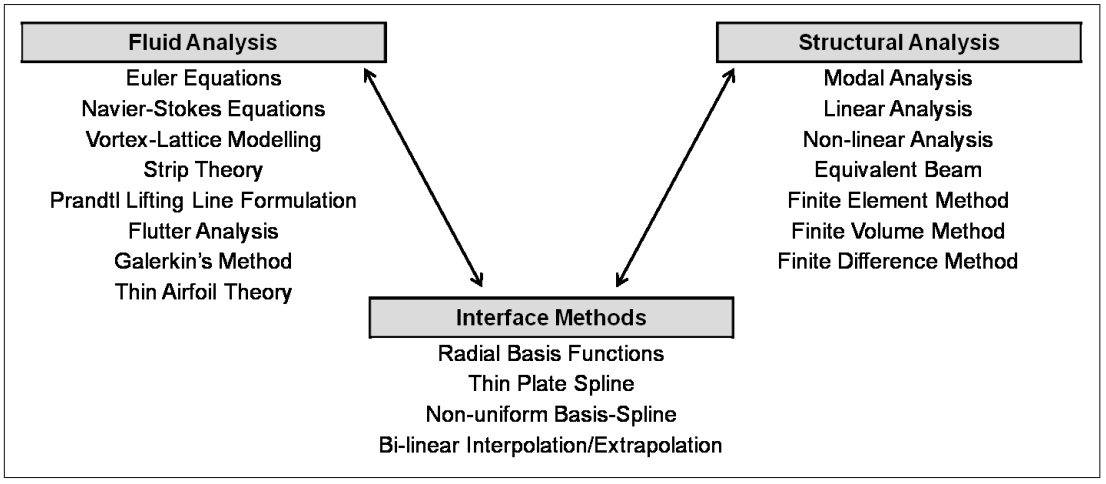

Figure 2.2: Aeroelastic areas of discussion.

2.2.1 Structural Component

Structural dynamics describes the behaviour of a structural component under a dynamic load. This section divides this field of research into the typical approximations made and solution methods used to obtain sufficient accuracy in the results.

The first step in any analysis is the definition of the problem. This leads to the approximations and simplifications that can reduce a highly complex problem to one that can be calculated by hand. However, there are many situations where it is not possible to obtain an exact solution to a numerical problem and we need to resort to approximations to achieve a discrete solution.

Typically the problem or system is described by a set of partial differential equations. There are three typical choices for the numerical solution of these equations when the number of equations to be solved becomes large; FEM, FVM and FDM. Each of these are briefly described below along with descriptions of other typical approaches.

Modal Approach This approach makes use of a structure's natural mass and stiffness to evaluate the frequencies at which it will resonate. These natural fre-

quencies can be used as a base for evaluating dynamic or frequency behaviour in a structure [3].

Linear Analysis This approach assumes that all aspects of the structure behave in a linear fashion and excludes aspects such as contact and anisotropic material properties.

Non-Linear Analysis This approach assumes that there is some non-linear behaviour in the structure that cannot be accurately approximated with a linear analysis. These typically include very large displacements and contact simulations.

Equivalent Beam This approach would assume that the structure can be simplified to an equivalent beam structure without compromising the accuracy of the results. This approach provides a quick and easy way to get a rough estimate of the solution and guide the user to areas of concern which can at a later stage be modelled in more detail.

Finite Element Method (FEM) This method can be described as a piecewise polynomial interpolation over elements of a model. A parameter, like displacement, is interpolated between nodes of the element and by connecting elements we can interpolate over the entire structure.

Finite Volume Method (FVM) This method is based on the integral conservation law which is enforced for small control volumes as defined by the mesh of the model.

Finite Difference Method (FDM) Derivatives in the partial differential equation are approximated by linear combinations of the function values at the grid points. Depending on which grid points are used, there are three forms of the FDM; forward difference, backward difference and central difference. This method lends itself to problems with regular geometries and time dependencies.

The Finite Element Method was chosen for the structural component of this project. Further details describing the method and its approximations can be seen in Chapter 3.

2.2.2 Aerodynamics

Aerodynamics is the study of the forces, moments and heat-transfer rates acting on a vehicle in flight. In order to determine these parameters the pattern of the flow around the vehicle needs to be described [16]. This may lead to several assumptions and approximations which may produce a more manageable set of equations to

solve. For example, if the temperature variations are small, we can assume that the density of the fluid will remain constant. Several of the more common approaches to aerodynamic simplifications and assumptions are described below.

The two most often used and widely spread sets of equations, which describe the behaviour of a fluid, are the Euler and the Navier-Stokes equations.

Euler Equations: These equations describe the relationship between the velocity, pressure and density of a moving fluid while assuming inviscid conditions. They describe conservation of mass, momentum and energy and are valid for compressible fluids but can be reduced for incompressible fluids. The Euler Equations are a simplified form of the more general Navier Stokes Equation. Equations 2.2 to 2.4 show the 2-dimensional, steady form of the Euler Equations.

$$\text{Continuity: } \frac{\delta(\rho u)}{\delta x} + \frac{\delta(\rho v)}{\delta y} = 0 \tag{2.2}$$

$$\text{X - Momentum: } \frac{\delta(\rho u^2)}{\delta x} + \frac{\delta(\rho uv)}{\delta x} = -\frac{\delta p}{\delta x} \tag{2.3}$$

$$\text{Y - Momentum: } \frac{\delta(\rho uv)}{\delta x} + \frac{\delta(\rho v^2)}{\delta y} = -\frac{\delta p}{\delta y} \tag{2.4}$$

Navier Stokes Equation: This equation describes the motion of a fluid, both turbulent and laminar, the solution of which is called a velocity or flow field. It assumes that the fluid is a continuum and does not consist of particles.

$$\text{Continuity: } \frac{\delta p}{\delta t} + \frac{\delta(\rho u)}{\delta x} + \frac{\delta(\rho v)}{\delta y} + \frac{\delta(\rho w)}{\delta z} = 0 \tag{2.5}$$

$$\text{X - Momentum: } \frac{\delta(\rho u)}{\delta t} + \frac{\delta(\rho u^2)}{\delta x} + \frac{\delta(\rho uv)}{\delta y} + \frac{\delta(\rho uw)}{\delta z} = -\frac{\delta p}{\delta x} + \frac{1}{Re_r}\left\{\frac{\delta \tau_{xx}}{\delta x} + \frac{\delta \tau_{xy}}{\delta y} + \frac{\delta \tau_{xz}}{\delta z}\right\} \tag{2.6}$$

$$\text{Y - Momentum: } \frac{\delta(\rho v)}{\delta t} + \frac{\delta(\rho uv)}{\delta x} + \frac{\delta(\rho v^2)}{\delta y} + \frac{\delta(\rho vw)}{\delta z} = -\frac{\delta p}{\delta y} + \frac{1}{Re_r}\left\{\frac{\delta \tau_{xy}}{\delta x} + \frac{\delta \tau_{yy}}{\delta y} + \frac{\delta \tau_{yz}}{\delta z}\right\} \tag{2.7}$$

$$\text{Z - Momentum: } \frac{\delta(\rho w)}{\delta t} + \frac{\delta(\rho uw)}{\delta x} + \frac{\delta(\rho vw)}{\delta y} + \frac{\delta(\rho w^2)}{\delta z} = -\frac{\delta p}{\delta z} + \frac{1}{Re_r}\left\{\frac{\delta \tau_{xz}}{\delta x} + \frac{\delta \tau_{yz}}{\delta y} + \frac{\delta \tau_{zz}}{\delta z}\right\} \tag{2.8}$$

$$\begin{aligned}\text{Energy:} \quad & \frac{\delta E_T}{\delta t} + \frac{\delta u E_T}{\delta x} + \frac{\delta v E_T}{\delta y} + \frac{\delta w E_T}{\delta z} = -\frac{\delta(up)}{\delta x} - \frac{\delta(vp)}{\delta y} - \frac{\delta(wp)}{\delta z} \\ - \quad & \frac{1}{Re_r Pr_r}\left\{\frac{\delta q_x}{\delta x} + \frac{\delta q_y}{\delta y} + \frac{\delta q_z}{\delta z}\right\} + \frac{1}{Re_r}\left[\frac{\delta}{\delta x}(u\tau_{xx} + v\tau_{xy} + w\tau_{xz})\right] \\ + \quad & \frac{1}{Re_r}\left[\frac{\delta}{\delta y}(u\tau_{xy} + v\tau_{yy} + w\tau_{yz}) + \frac{\delta}{\delta z}(u\tau_{xz} + v\tau_{yz} + w\tau_{zz})\right] \end{aligned} \tag{2.9}$$

Through the use of simplifications and assumptions, several theories and approaches have been developed for specific use with airfoils.

Vortex Lattice Modelling [15]: This method is based on the assumption of a vortex singularity as the solution of Laplace's equation. Using the Biot-Savart law (2.10) it is possible to create expressions for three special cases of vortex generation [17]. These special cases are combined to form horse-shoe vortices. This horse-shoe vortex is then applied to a lattice of quadrilateral panels. The circulation strengths of each panel is determined by solving a system of linear equations that satisfy the boundary conditions.

$$\overrightarrow{\delta B} = \frac{\mu_0 \overrightarrow{I dL} \times \overrightarrow{l_r}}{4\pi r^2} \tag{2.10}$$

Strip Theory: Three-dimensional aerodynamics are approximated by section-wise two-dimensional flow. This approximation is good for long slender wings. Since the analysis is two-dimensional, the aerodynamic forces are over predicted, which leads to conservative results [5].

Prandtl Lifting Line Formulation: This method models the wing as a combination of bound vortex sheets (pressure difference) and free vortex sheets (no pressure difference). If the wing has a large aspect ratio, the bound vortex sheet can be approximated as a bound vortex line, also known as the lifting line [17]. This method assumes an incompressible, inviscid and irrotational flow. It is only valid for planar unswept wings as it does not account for spanwise flow. However, for small sweep angles it is still considered a valid approximation [5].

Flutter Analysis: This analysis is not strictly an aerodynamic approach but rather a combination of structural and aerodynamic interactions that defines the dynamic stability of the aeroelastic system [18]. There are three primary methods of solution for flutter, i.e. the K-method, the KE-method and the PK-method.

Galerkin's Method: Delivers an approximate solution of the boundary-value problem. Obtain a set of simultaneous linear algebraic equations [6].

Thin airfoil theory: This theory assumes the flow around an airfoil to be two dimensional and applied to a wing with an infinite span. It is valid for inviscid, incompressible flows and relates the angle of attack to lift for a specific airfoil.

The Prandlt Lifting Line Formulation was chosen for the aerodynamic component of this project. Further details describing the method and its approximations can be seen in Chapter 4.

2.2.3 Coupling

In most cases, the coupling between the structural and aerodynamic components is performed by means of interpolation along the interface between these two regions. There are several methods for the determination of the interface surface and interpolation functions a few of which are described below.

Radial Basis Function: This is a function that is used to approximate a multivariable function by linear combinations of a single variable function.

Thin Plate Spline: This spline is a special case of a polyharmonic spline which is a commonly used radial basis function. It is useful for the interpolation of surfaces over scattered data [19].

Non-uniform Basis-Spline: This is a mathematical model used to generate curves and surfaces which have high precision and flexibility to handle both analytic and freeform shapes.

Bi-linear Interpolation/Extrapolation This method is an extension of linear interpolation or extrapolation designed for two variables. This function is not linear but a combination of two linear functions.

2.3 Experimental Work

Experimentation is used as a form of verification of results obtained by other means, either using analytical calculations or numerical simulations [20]. For this project, the results obtained numerically will need to be verified by wind tunnel tests. This section further discusses typical experimental and wind tunnel procedures.

Parameters that are typically measured during wind tunnel testing include pressure, deflection and forces on the structure. Additionally, the characteristics and capabilities of the testing equipment available will influence the accuracy of the experimental work. Two papers in particular review wind-tunnel test procedures as well as list good experimental habits [21], [22], [23].

Possible methods for modelling the experimental wing structure include mounting the panel on a turntable (for changes in angle of attack). A setup with a small gap between the inboard end and the tunnel wall creates an air seal between the wing and the tunnel wall which models that between a wing and the fuselage.

2.3.1 Experimental Model

Typical wind tunnel testing with a wing-like structure aims to evaluate the flow field around a specific aerofoil. For this type of problem the wing spans the width of the test section and the problem becomes a two dimensional one. Our problem, however, needs the wing to be free at one end so that the deflection of the wing due to aerodynamic forces becomes visible. This makes the problem three dimensional, which is more realistic but also more complex to analyse. Additionally, we will only be testing a component of the aircraft. This is another reason the configuration of the model must be as realistic and representative as possible.

The approach used by Heinze [5], is to create a semispan model made up of a load carrying beam of carbon-fiber. Aerodynamic sections are rigidly clamped to the beam in such a way so as not to add stiffness to the beam structure. Scaled airfoil profiles were used and slots between the wing and control surfaces are sealed with elastic polymer strips.

There are many ways that a parameter can be modelled; for example, stiffness of the wing can be modelled by a solid material with a stiffness K or a thin-walled frame with the same stiffness could be used. While the stiffness parameter has remained constant, the effect on other parameters is undefined. In this case, the investigator must focus on achieving quality results for the most critically defining parameters.

2.3.2 Use of Wind-Tunnel data

Wind-tunnel test data always suffer from a great number of unknowns. One of these unknowns is a parameter that can play a large role in the behaviour of the air flow and is called the boundary layer. The boundary layer is defined as the region around the wing where there is a velocity gradient. The velocity near the wing reaches zero due to friction on the surface. The thickness of the layer is defined as the region between the surface and the point where the velocity reaches 99% of the free-stream velocity. Thickness and drag associated with the boundary layer are related to the Reynolds number If the Mach Number, M_a, is smaller than 0.3, which is the case in the low-speed wind tunnel, the flow can be assumed to be incompressible [24].

Laminar flow has less energy with which to surmount roughness or corners and separates from the surface of the wing more easily than turbulent flow. As the Reynolds number increases, it becomes harder to maintain the laminar boundary

layer. The model created for this project will not be scaled to a full wing since the results will only be used for verification purposes. However, there are several concerns if this were not the case, one of them being appropriate scaling of the structures characteristics.

The following equations are very useful when scaling models and comparing subsequent experimental runs.

$$\text{Reynolds Number:} \quad Re = \frac{\rho}{\mu} V l \tag{2.11}$$

$$\text{Mach Number:} \quad M_a = \frac{V}{a} \tag{2.12}$$

$$\text{Froude Number:} \quad Fr = \sqrt{\frac{V^2}{lg}} \tag{2.13}$$

If a model has the same Re and M_a numbers as the real situation, then these forces and moments can be directly scaled and the flow patterns will be similar [23]. The Froude number is generally used when scaling partially submerged objects when analysing the effects of free-surfaces.

To ensure that the effects of the walls of the wind tunnel on the flow field around the model are negligible, the model span should be smaller than 0.8 of the width of the test-section [23]. Additional experiments could be conducted to evaluate the velocity profile of the flow area which would also give an indication of the uniformity of the air flow.

Chapter 3

Structural Model

3.1 Introduction

This chapter looks at the specific formulation of the structural component of the aeroelastic analysis. We will start by reviewing simple Beam theory and then look at the Finite Element Method in general with some technical definitions.

The first model that was investigated, was a simple one dimensional beam model. The limitations and approximations of this model are also discussed. The beam model is then further developed until a three-dimensional model is created and verified using commercial software. The algorithm for this implementation is also discussed.

3.2 Beam Theory

Beam theory is only valid if the following prerequisites are met [25].

- The minimum cross-section of the beam is much smaller than the length of the beam.
- The center of gravity of the section forms a straight line when in an unloaded state through the length of the beam.
- Displacements and deformations are small.
- The resultants of the applied loads must lie in one plane.
- The cross-section of the beam must be symmetric around one of its axes which must also lie in the plane in which the loads are applied.

Beam theory is applied through the following set of general equations:

$$\frac{d^2v}{dx^2} = \frac{M}{EI} \tag{3.1}$$

$$\theta = \frac{dv}{dx} = \int \frac{M}{EI}dx + k_1 \tag{3.2}$$

$$v = \int \theta dx + k_2 \tag{3.3}$$

with M the bending moment defined as a function of distance x from the origin and the externally applied force. θ is the gradient of the displacement line at any position x from the origin and v is the vertical displacement at any position x from the origin. E represents the Young's Modulus of the material. I is defined as the moment of inertia for the cross-section around the neutral axis. k_1 and k_2 are integration constants that are dependent on boundary conditions.

This general case can be reduced to special cases with predefined boundary conditions. For example, a cantilever beam is defined as having a fixed-end and a free end with the boundary conditions for gradient and displacement as $\theta = 0$ and $v = 0$ at the fixed end.

3.2.1 Worked Example

Let us briefly take a look at a worked example for calculating the deflection for a cantilever beam with a varying cross-section. This hand calculation is later used to verify preliminary structural code results.

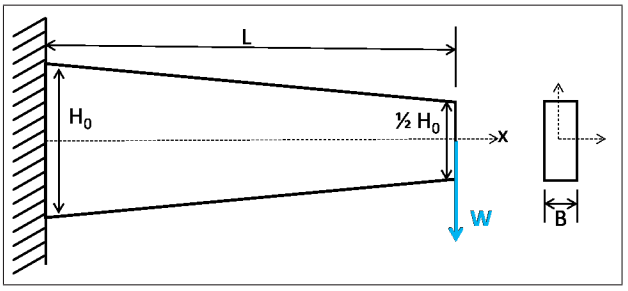

Figure 3.1: Worked Example.

We are given the length of the beam, L, the breadth, B, and the load, W. The height of the cross-section varies from H_0 at the fixed end to $\frac{1}{2}H_0$ at the free end, refer to Figure 3.1. The height at any point can therefore be given by:

$$H = H_0\left(1 - \frac{x}{2L}\right) \tag{3.4}$$

Due to the change in height, the second moment of inertia, I, will vary along the length of the beam.

$$\begin{aligned} I &= \frac{BH^3}{12} \\ \text{therefore } I &= I_0\left(1 - \frac{x}{2L}\right)^3 \text{ with } I_0 = \frac{BH_0^3}{12} \end{aligned} \tag{3.5}$$

Then by making use of Equation 3.1 and including boundary conditions we can integrate to get both the displacement and rotation at any position along the length of the beam.

$$\frac{d^2v}{dx^2} = \frac{W(L-x)}{EI} = \frac{W(L-x)}{EI_0}\left(1 - \frac{x}{2L}\right)^{-3} \tag{3.6}$$

$$\theta = \frac{dv}{dx} = \frac{WL^2}{EI_0}\left(4\left\{1 - \frac{x}{2L}\right\}^{-1} - \left\{1 - \frac{x}{2L}\right\}^{-2} - 3\right) \tag{3.7}$$

$$v = \frac{WL^3}{EI_0}\left(-8\ln\left\{1 - \frac{x}{2L}\right\} - 2\left\{1 - \frac{x}{2L}\right\}^{-1} - \frac{3x}{L} + 2\right) \tag{3.8}$$

3.3 The Finite Element Method

The main purpose of the Finite Element Method (FEM), is to solve numerically complex continuous systems for which it is not possible to construct any analytical solution [3],[1]. Before the development of the digital computer, the implementation of such a solution method was nearly impossible and extremely time consuming. In the 1950's, the development of delta wings, which could not accurately be defined by beam theory, led to the further development of this method. The FEM is now implemented in a variety of applications including heat transfer, groundwater flow, magnetic field and structural analysis.

Let us start the discussion with some basic definitions used is this field of study.

3.3.1 Definitions

Discrete and continuous systems can be subdivided into three typical problem types [1].

- Equilibrium or Boundary Value Problems
- Eigenvalue Problems and
- Propagation or Initial Value Problems

Boundary Value Problem is a system defined by a set of differential equations along with a set of restraints or conditions applied to the boundary of the system. A solution to the boundary value problem satisfies the differential equations as well as the boundary conditions (Equation 3.9).

Eigenvalue Problem for a structure is one that determines the natural frequencies at which the structure would begin to resonate.It makes use of a structures mass and stiffness (Equation 3.10).

Initial Value Problem is also a system defined by a set of differential equations but has conditions specified at a specific point in time. (Equation 3.11)

$$[\mathbf{K}]\{U\} = \{F\} \tag{3.9}$$

$$[\mathbf{K}]\{U\} = \lambda[\mathbf{M}]\{U\} \tag{3.10}$$

$$[\mathbf{M}]\{\ddot{U}\} + [\mathbf{C}]\{\dot{U}\} + [\mathbf{K}]\{U\} = \{F(t)\} \tag{3.11}$$

Finite Element Method The essence of the FEM is that a continuous structure or model is broken up into a finite number of elements. Each element has a set of properties describing its behaviour and how it connects to surrounding elements. The properties are then interpolated across the element. Since the conditions at the boundaries of the elements are known, the properties can be interpolated across the entire structure. Unfortunately, unless the problem is a very simple one with an exact formula, the solution will be approximate. However, by increasing the number of elements, i.e. decreasing their size, we can achieve a very good approximation.

Degrees of Freedom are independent quantities that govern the spatial variation of a field [2]. Since we are typically working in a Cartesian co-ordinate system, any point on a structure could move in any number of the six possible manners, i.e. six DOF. The figure below shows the three displacements and three rotations that are possible. Every node of every element in the discretized structure has these six DOF unless constrained by boundary conditions [26].

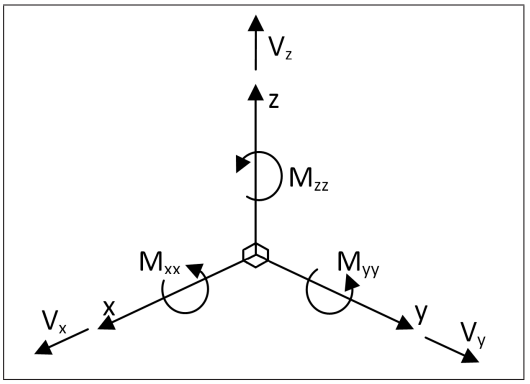

Figure 3.2: Six Degrees of Freedom represented in a Cartesian co-ordinate system

Elements and Element Types A complex structure can be simplified by making use of appropriate element types. The number of nodes describing the element varies according to the application in which it is to be used. Element types include bars, beams, shells, planes or plates and solids or hexahedral elements. The most obvious difference between these element types is the number of degrees of freedom of each. An example of such a simplification would be a truss structure that can be constructed from beam elements, with perhaps only 2 or 3 DOF per element instead of three dimensional elements which might have up to 60 DOF per element. This greatly reduces the DOF that need to be solved and reduces the chance of user error. For this structure, the beam element is a good representative for the type of behaviour of the structure.

It is important that the correct element type is used for a specific application. A bar element would not be able to accurately represent a plate like structure. Similarly, a plate element might not be accurate for a beam like structure. Obviously, the more complex an element is, the larger the cost of calculation so there is a fine line between choosing a large number of simple elements, or fewer more complex elements.

The user of the FEM must have a good understanding of each of the element types so that the limitations of each type can be taken into consideration when modeling the structure. This includes the interpreting of results and evaluating their applicability. The specifics of each element type is discussed later in this section.

Mesh A mesh is the grid of elements that combine to form the structure to be analysed. Two distinct elements can have common points only on their common boundaries if such boundaries exist; no overlapping is allowed. Common

boundaries can be points, lines, or surfaces [1]. The assembled elements should leave no holes within the domain and approximate the geometry of the real domain as closely as it is possible to do. When the boundary of a domain cannot be exactly represented by the elements selected, an error cannot be avoided. Such an error is called the geometrical discretization error and it can be decreased by reducing the size of the elements or by using elements allowing boundaries to become curved [1].

Isoparametric Formulation The isoparametric formulation is a method of mathematically describing an element of any type in a local co-ordinate system in such a manner that it can easily be incorporated into a complex structure. This is further discussed as part of the Structural Algorithm in Section 3.5.

Bars A bar is the simplest element type available. It is defined as a uniform elastic bar with a length L, elastic modulus E and a cross-sectional area A. A node is situated at each edge. This element has only two DOF that are unconstrained, i.e it can only move in the axial direction. Due to this limitation, this element can only be used to model structures where the behaviour in the axial direction is dominant and the others can be considered negligible [2].

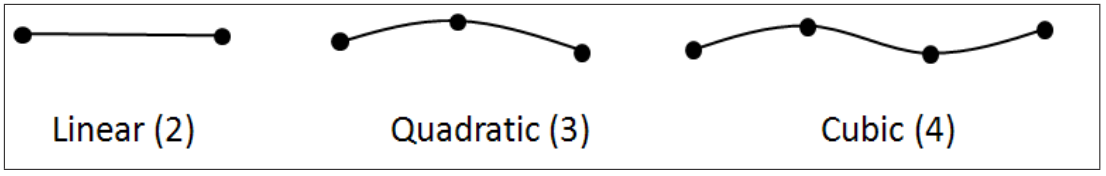

Figure 3.3: Bar and Beam Elements [1].

Beams A beam element is similar to a bar element but has at least two DOF at each node, one being a displacement and the other a rotation. This means that a beam is able to model bending in the structure while the bar is not. This is one of the advantages of the beam element, refer to Figure 3.3. Additional displacement and rotation DOF may be unconstrained to improve the model. This element is based on the Euler-Bernoulli beam theory. The beam element also has a constant cross-section, however, the profile may vary. For example, structures with I cross-sections can typically be constructed using beam elements [2].

Shell elements This element is a two dimensional element that can displace and rotate within the plane, refer to Figure 3.4. This implies a maximum of three DOF per node. There are several sub-types in the plane elements group. They

are the linear triangle (Constant Strain Triangle), the Quadratic triangle (Linear Strain Triangle), the Bilinear rectangle (Quad4) and the Quadratic rectangle (Quad8, Quad9). The difference between the linear and quadratic triangular elements is the number of nodes with the linear triangle only having three nodes, one at each apex, while the quadratic triangle has six nodes, one at each apex and then a node mid-side. This means that while the linear triangle can only represent a linear displacement field the quadratic triangle can represent a quadratic displacement field. In problems where bending would occur, the linear triangle would not be suitable and the result would be an overly stiff structure. The quadratic triangle would be more suitable. Similarly, the bilinear rectangle can only represent a linear displacement field while the quadratic rectangle can represent a quadratic displacement field. The shell element is defined by its thickness and the location of its midsurface [3].

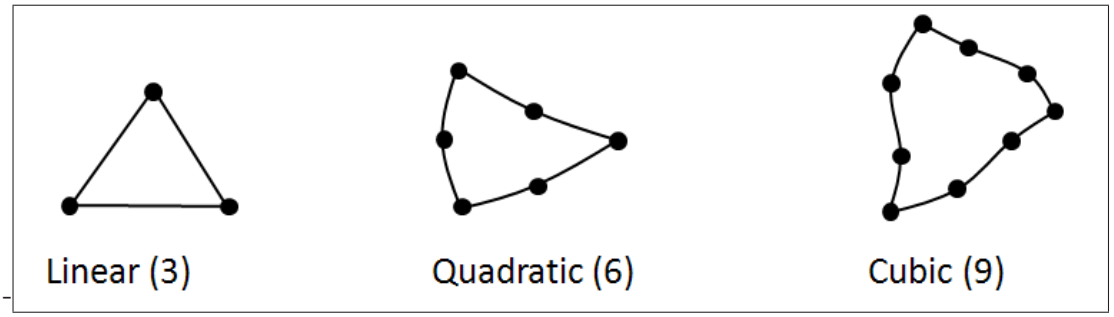

(a) Triangular Shell Elements.

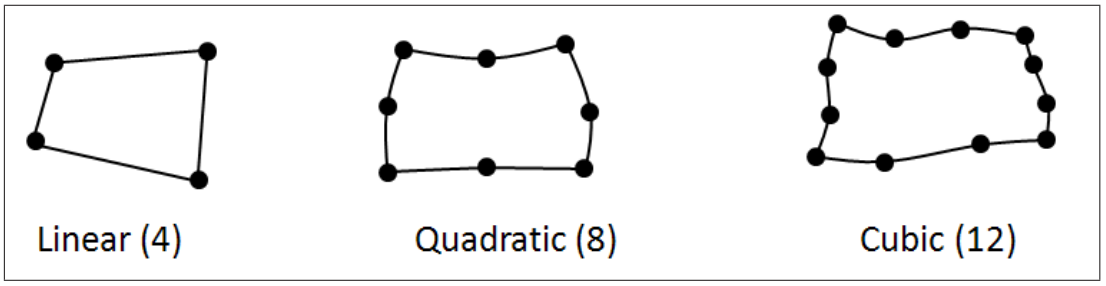

(b) Rectangular Shell Elements

Figure 3.4: Common Element configurations for Shell element types [1].

Solid elements A solid element is a plane element that has been extended to three dimensions. Each node can represent all six DOF. Like the plane elements there are linear and quadratic elements. The linear elements are not suitable for problems that need to represent bending of the structure. Solid elements of a triangular nature are called tetrahedral and those based on rectangles are called hexahedral. With the increased DOF the computational cost for solid

elements is much higher than that needed for plane or beam elements. Often, a problem can be simplified to make use of a less costly element and reasonably accurate results can still be obtained [1].

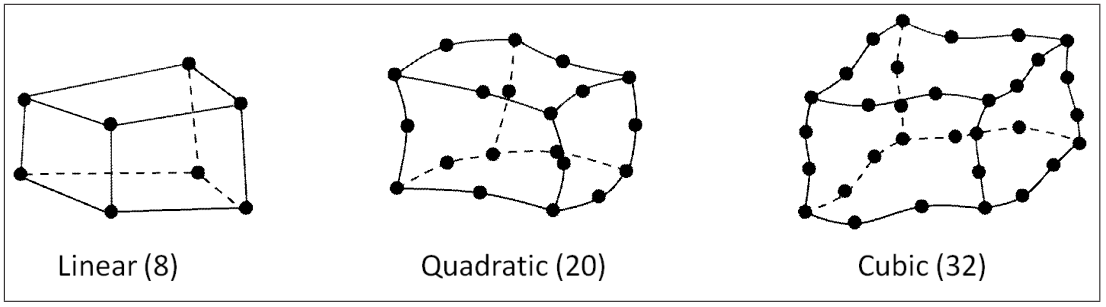

Figure 3.5: Hexahedral elements [1].

Plates A plate is defined as an element whose thickness is much smaller than its height or width [2]. Under these circumstances, a solid elements can not be used since their formulation becomes ill-conditioned when the aspect ratio becomes large. The formulation of this type of element is based on either the Kirchoff theory or the Mindlin theory. A plate also remains flat, while a beam for example can bend.

3.4 Structural Approximations

During the literature study there were a number of modelling approximations suggested for the structural component of an aeroelastic analysis. Those most relevant are described below:

The Rectangular Beam where the wing-like structure is modelled by a simple solid beam and the effects of displacements and forces are evaluated using beam-theory [8].

A 2D Aeroelastic Model where integrals represent all the wing properties [27].

Thin Walled Anisotropic Beam method is very similar to beam-theory, however, the thin wall approximation provides a more realistic stiffness model which is harder to create [27]

Mode Shapes can be used to obtain structural response which reduces the number of equations that need to be solved [28].

Eigenvalue and Eigenfunction Approach which neglects terms that do not depend on elastic twist [8].

Each of these proposed methods have their own advantages, but the rectangular beam representation was chosen as a first step due to its ease of implementation.

Initially a one-dimensional rigid-jointed structure [29] was used as a first approximations for the wing-like structure. This type of structure reacts to bending and torsion loads as well as tension and compression loads. The continuous structure was broken up into a small number of beam elements and the behaviour of each element was evaluated. This was done as a hand calculation like that seen in Section 3.2.1 but at discrete points along the length of the structure. The limitations of this first approximation were quickly identified, the most important of which being that only the simplest of configurations could be analysed. The next step would be to implement three-dimensional elements.

3.4.1 Element Type

Once it was determined that a three-dimensional model is the most suitable way to capture all the relevant behaviour of the structure, the next step is to determine the type of element to use to accurately model the structure. As seen in Section 3.3, the three dimensional elements include brick-like elements, called hexahedrals, and triangular elements, called tetrahedrals. Since the first approximation we make is that we can represent the wing with a beam, the hexahedral elements are the natural choice.

The next decision regarded the number of node points on the element. As a first step the linear, or 8-noded element was considered. This element has a node at every corner of the element. Since there are only eight nodes and therefore only eight shape functions , this meant implementation would be easier and the correct method of calculation could be tested before trying to implement a higher order element.

However, this type of element can only represent linear displacement, as the name implies, and when implemented would not converge to a correct answer, even with mesh refinement. The next option was to make use of a quadratic hexahedral element, i.e. 20 nodes as seen in Figure 3.5. The order in which the nodes are numbered are relevant when defining the shape functions and the ensuing calculations.

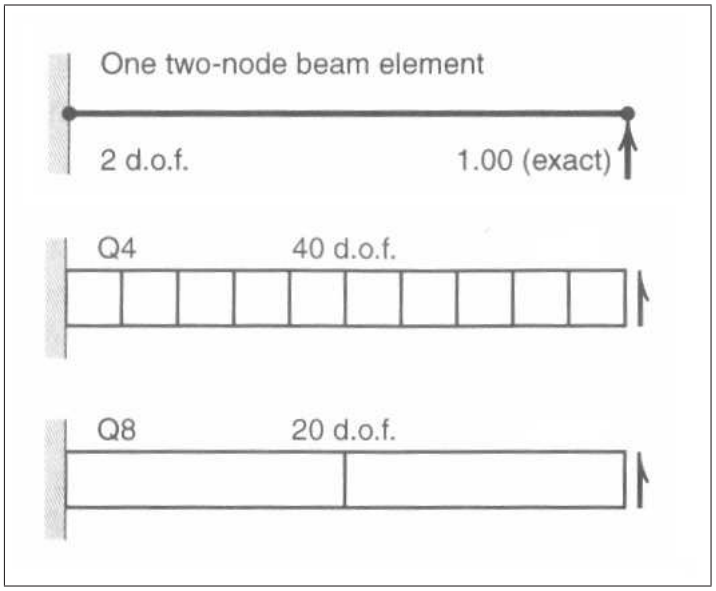

Figure 3.6: The effect of number of nodes on the degrees of freedom of a system [2].

3.4.2 Meshing

Deciding on the coarseness of a mesh is a compromise between the complexity of the element type to be used and the cost of the computation. The structure being analysed can either be modelled by lots of simple elements or fewer complex elements, refer to Figure 3.6. The displacement at a node is the same for all elements touching that node, however, the stresses are not.They are discontinuous. A check for the convergence of the mesh is to quantify the discontinuity at the nodes. Refinement of the mesh can lead to more acceptable discontinuities.

Let us look at Figure 3.7. The element on the left represents a continuous beam and we see that the response of the beam to a moment produces both a displacement and a rotation. The element on the right is a linear element and can not model the quadratic behaviour of the top and bottom surfaces of the real element. The accuracy of the solution can be increased by using many more, smaller elements, however, the solution will always represent an upper bound on the stiffness of the structure. Another way to improve the solution would be to add nodes mid-side of the element. The edge can then represent quadratic or higher order curves. An example of this would be to replace the 8-noded elements chosen above with 20-noded elements. The implementation of 20-noded elements is discussed as part of the structural algorithm (Section 3.5).

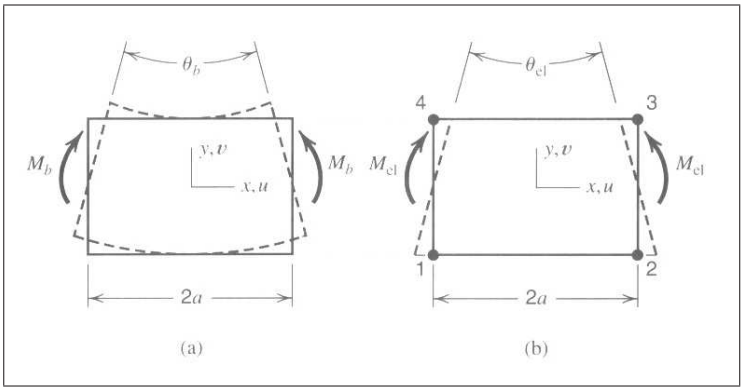

Figure 3.7: Comparison of continuous ideal element (a) and finite element representation (b)[3].

3.4.3 Isoparametric Formulation

The general formulation of an element is defined in global co-ordinates, however, a structure is usually made up of many elements and the orientation will differ for each element. An isoparametric element is an element that has a reference shape defined in the natural Cartesian coordinate system, $[\xi, \eta, \zeta]$, as seen in Figure 3.8. This element is transformed to the global co-ordinate system by means of shape functions. The shape function of a specific node is described as the behaviour of a nodal DOF when it is given a unit value while the other DOF's are zero. This allows quadrilateral and hexahedral elements to have non-rectangular shapes since it is difficult to mesh a curved surface with only rectangular elements.

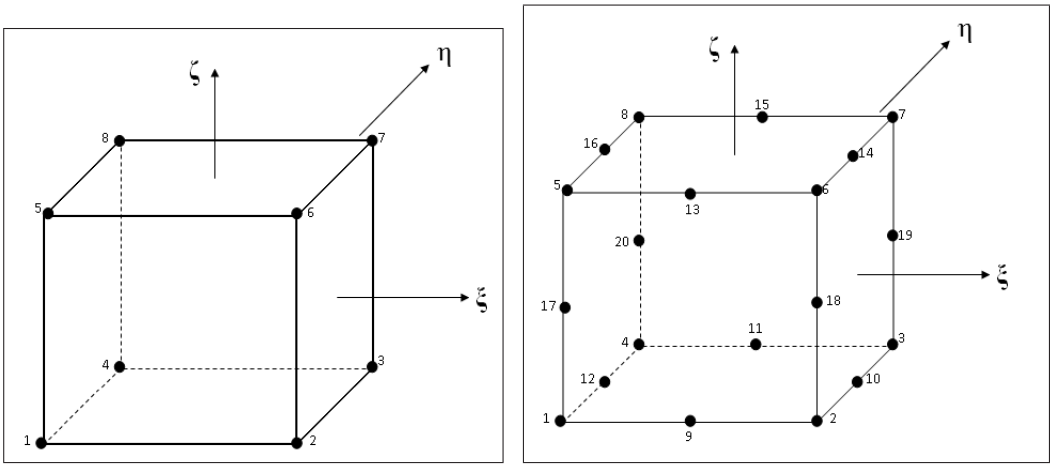

(a) 8-Noded Isoparametric Hexahedral Element (b) 20-Noded Isoparametric Hexahedral Element

Figure 3.8: Natural Co-ordinate system for 8- and 20-noded elements.

The same shape functions used to determine node co-ordinates are also used to calculate the node displacements. These displacements must then be differentiated with respect to the global co-ordinates x, y, and z [2] in order to obtain a global isoparametric formulation for the stiffness matrix of a structure, seen in Equation 3.12 below.

$$\mathbf{K} = \int_V \mathbf{B}^T \mathbf{E} \mathbf{B} dV \tag{3.12}$$

with $\mathbf{K}$ the stiffness matrix of the element, $\mathbf{B}$ is the strain-displacement matrix and $\mathbf{E}$ is the stress-strain matrix. Further development of the strain-displacement matrix can be seen in Section 3.5.

3.4.4 Interpolation Techniques

Equation 3.12 indicates that numerical integration needs to be performed to develop the stiffness matrix. The most common method used in a FEM environment is the Gauss Quadrature method. This method evaluates the function at specific points, multiplies the resulting number by an appropriate weighting factor, and a summation of the results over the entire body [2]. Let us assume that the function to be integrated is $\phi()$ over the natural co-ordinates $[\xi, \eta, \zeta]$, i.e. a three-dimensional element.

$$\mathbf{I} = \int_{-1}^{1}\int_{-1}^{1}\int_{-1}^{1} \phi(\xi, \eta, \zeta)\ d\xi\ d\eta\ d\zeta \tag{3.13}$$

$$\approx \sum_i \sum_j \sum_k W_i W_j W_k \phi(\xi_i \eta_j \zeta_k) \tag{3.14}$$

The weightings, $W_{i,j,k}$, are dependent on the number of integration points to be used which in turn are dependent on the type of element, the matrix to be constructed (either $\mathbf{K}$ or $\mathbf{M}$) and the geometry of the real element. General guidelines regarding the number of integration points when integrating using Gauss Quadrature can be seen in the Table 3.1. Figure 3.9 shows the location of the integration points for a 2×2 and 3×3 Gauss Quadrature rule in natural co-ordinates.

Gauss Quadrature Rule		
Element Type	**Full**	**Reduced**
4-node plane	2×2	1-point
8-node plane	3×3	2×2
9-node plane	3×3	2×2
8-node solid	$2 \times 2 \times 2$	1-point
20-node solid	$3 \times 3 \times 3$	$2 \times 2 \times 2$

Table 3.1: The number of integration points needed to ensure convergence when integrating using the Gauss Quadrature rule [2].

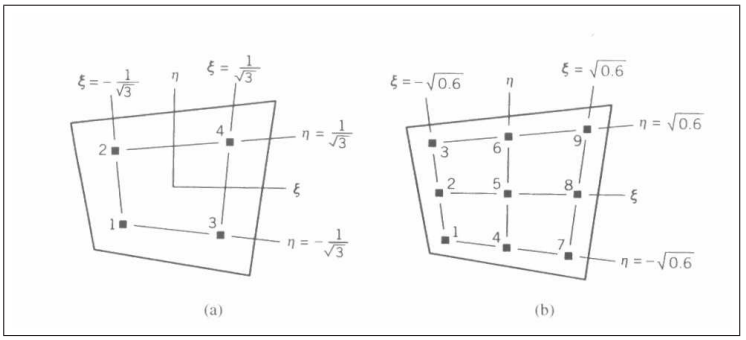

Figure 3.9: Gauss Point locations for integration in 2 dimensions using a 2×2 and a 3×3 rule.

3.4.5 Solution methods

Once the Mass matrix, Stiffness matrix and force vectors have been defined, the linear static problem can be solved using a simple Gauss Elimination as seen is Section 4.4.3. For larger problems which might include damping, have sparse matrices or may be nearly non-linear there are more complex methods for solving the system which are more time and cost effective.

3.4.6 Numerical Precision

During the development of the structural algorithm it was felt that the precision provided by a number of double format (32bit) would be insufficient to produce accurate results when it eventually improved to include a time analysis. The difference in order of magnitude for the mass and stiffness matrix meant that very large numbers would be multiplied by very small numbers and the chances for round off error become very large. To improve these results, an infinite precision mathematical library was implemented on the whole algorithm [30].

This would allow the programmer to decide, based on the application and need at that point in the code, the appropriate precision in all calculations. However, this

also meant that every action, including addition, subtraction. assigning values etc were all implemented as functions. This greatly increased processing time and the storage requirements for any simple action. Due to the fact that this simulation is to be used in a control system environment, this process is much too slow to provide any possible improvement on results generated using a double number format. It was, therefore, decided that the double precision math functions would be sufficient.

3.5 Stuctural Algorithm

The structural algorithm describes the processes of creating the isoparametric stiffness matrix, Equation 3.12, for the given structure and then solving the set of linear equations to produce resulting displacements. The algorithm starts with the inputs necessary from the user. These include general geometric and material properties. Additionally, the user must prescribe the number of elements in each axis of the global co-ordinates. Table 3.2 lists these inputs and the typical values used in the analysis of our experimental model.

Property	**Typical Value**
Youngs Modulus	79 GPa
Poisson Ratio	0.33
Material Density	2650 kg/m^3
Half Wing span	0.5 m
Root Chord	0.1 m
Tip Chord	0.1 m
Thickness	0.001 m
Number of elements in global X	20
Number of elements in global Y	2
Number of elements in global Z	1
Percentage Chord	0.25

Table 3.2: Typical inputs for the Stuctural component

The percentage chord indicated in Table 3.2 refers to the application point of the applied load. For wing-like structures it is valid to assume that all forces acting on the structure occur a the quarter chord position. This implies twisting and displacement of the structure. Initially the load was a single point load at the free end of the structure so that hand calculations could be used to verify the resulting deflections.

Once the inputs have been accepted as valid, the total number of elements, total number of unique nodes and number of equations is determined. The number of elements being the multiplication of the user inputs for number of elements in X, Y and Z. Each element is defined as having 20-nodes, however many of the elements

share boundaries. Therefore, only one node at a specific global co-ordinate will be counted. A solid element requires that only the translation DOF are necessary to capture the behaviour of the structure. Therefore, the number of equations is three times the number of unique nodes.

The structure is then broken up into elements. Each element is made up of a structure which contains all the relevant information for every node of that element.

Algorithm 3.1: Element Structure.

struct node

```
x ;                                  /* Global X - co-ordinate of node */
y;                                   /* Global Y - co-ordinate of node */
z;                                   /* Global Z - co-ordinate of node */
num;                                       /* Global numbering of node */
rest;                          /* Restraint condition applied to node */
δN/δξ;                       /* Nodal shape function derivative wrt ξ */
δN/δη;                       /* Nodal shape function derivative wrt η */
δN/δζ;                       /* Nodal shape function derivative wrt ζ */
δN/δx;                       /* Nodal shape function derivative wrt X */
δN/δy;                       /* Nodal shape function derivative wrt Y */
δN/δz;                       /* Nodal shape function derivative wrt Z */
```

struct element = 20×node

The next step is determining the global material properties. With the information provided by the user, we create a 6×6 Stress/Strain matrix as seen below.

$$\mathbf{E} = \begin{bmatrix} (1-\nu)c & \nu c & \nu c & 0 & 0 & 0 \\ \nu c & (1-\nu)c & \nu c & 0 & 0 & 0 \\ \nu c & \nu c & (1-\nu)c & 0 & 0 & 0 \\ 0 & 0 & 0 & G & 0 & 0 \\ 0 & 0 & 0 & 0 & G & 0 \\ 0 & 0 & 0 & 0 & 0 & G \end{bmatrix} \tag{3.15}$$

with $c = \frac{E}{(1+\nu)(1-2\nu)}$ and $G = \frac{E}{2(1+\nu)}$

At this stage we can start the integration to develop the isoparametric stiffness matrix. The structural algorithm currently makes provision for a $3 \times 3 \times 3$ and a $4 \times 4 \times 4$ Gauss Quadrature rule. This implies 27 and 64 points of integration for each element respectively. The rest of the algorithm is documented with a $3 \times 3 \times 3$ rule.

As seen in Figure 3.9 the values of the Gauss Point vary between $[-\sqrt{0.6},\ 0.0,\ \sqrt{0.6}]$ in each natural co-ordinate axis. The weighting is then based on the location of the integration point as seen in the table below.

ξ	η	ζ	**Weight**
$\sqrt{0.6}$	$\sqrt{0.6}$	$\sqrt{0.6}$	W_2
$\sqrt{0.6}$	$\sqrt{0.6}$	0	W_3
$\sqrt{0.6}$	$\sqrt{0.6}$	$-\sqrt{0.6}$	W_2
$\sqrt{0.6}$	0	$\sqrt{0.6}$	W_3
$\sqrt{0.6}$	0	0	W_4
$\sqrt{0.6}$	0	$-\sqrt{0.6}$	W_3
$\sqrt{0.6}$	$-\sqrt{0.6}$	$\sqrt{0.6}$	W_2
$\sqrt{0.6}$	$-\sqrt{0.6}$	0	W_3
$\sqrt{0.6}$	$-\sqrt{0.6}$	$-\sqrt{0.6}$	W_2
0	$\sqrt{0.6}$	$\sqrt{0.6}$	W_3
0	$\sqrt{0.6}$	0	W_4
0	$\sqrt{0.6}$	$-\sqrt{0.6}$	W_3
0	0	$\sqrt{0.6}$	W_4
0	0	0	W_5
0	0	$-\sqrt{0.6}$	W_4
0	$-\sqrt{0.6}$	$\sqrt{0.6}$	W_3
0	$-\sqrt{0.6}$	0	W_4
0	$-\sqrt{0.6}$	$-\sqrt{0.6}$	W_3
$-\sqrt{0.6}$	$\sqrt{0.6}$	$\sqrt{0.6}$	W_2
$-\sqrt{0.6}$	$\sqrt{0.6}$	0	W_3
$-\sqrt{0.6}$	$\sqrt{0.6}$	$-\sqrt{0.6}$	W_2
$-\sqrt{0.6}$	0	$\sqrt{0.6}$	W_3
$-\sqrt{0.6}$	0	0	W_4
$-\sqrt{0.6}$	0	$-\sqrt{0.6}$	W_3
$-\sqrt{0.6}$	$-\sqrt{0.6}$	$\sqrt{0.6}$	W_2
$-\sqrt{0.6}$	$-\sqrt{0.6}$	0	W_3
$-\sqrt{0.6}$	$-\sqrt{0.6}$	$-\sqrt{0.6}$	W_2

Table 3.3: Gaussian Quadrature Weights and Abscissae for Integration over a Cube [4] with $W_2 = 0.171467764060357$, $W_3 = 0.274348422496571$, $W_4 = 0.438957475994513$ and $W_5 = 0.702331961591221$

The algorithm for the integration of a single element can then be described as follows:

Algorithm 3.2: Development of Isoparametric Stiffness Matix for an Element.

for $\xi = -\sqrt{0.6} : 0.0 : \sqrt{0.6}$ **do**
  for $\eta = -\sqrt{0.6} : 0.0 : \sqrt{0.6}$ **do**
    for $\zeta = -\sqrt{0.6} : 0.0 : \sqrt{0.6}$ **do**
      evaluate $N_{Shape}(1:20)$; `/* Refer to Section 3.5.1 */`
      evaluate $\frac{\delta N}{\delta \xi,\eta,\zeta}(1:20)$; `/* Refer to Section 3.5.1 */`
      evaluate $Jacobian(\frac{\delta x,y,z}{\delta \xi,\eta,\zeta})$; `/* Refer to Section 3.5.2 */`
      evaluate $B(1:20)$; `/* Refer to Section 3.5.3 */`
      evaluate $K = Weight_{\xi,\eta,\zeta} \cdot B^T \cdot E \cdot B \cdot Jacobian$; `/* Refer to Section 3.5.4 */`
    end
  end
end

3.5.1 Shape Functions

The shape functions for a 20-noded isoparametric hexahedral element and its derivatives with regard to the natural co-ordinate system can be seen below [1].

Corner Nodes:

$$N_i = \frac{1}{8}(1+\xi\xi_i)(1+\eta\eta_i)(1+\zeta\zeta_i)(-2+\xi\xi_i+\eta\eta_i+\zeta\zeta_i) \tag{3.16}$$

$$\frac{\delta N_i}{\delta \xi} = \frac{1}{8}\xi_i(1+\eta\eta_i)(1+\zeta\zeta_i)(-1+2\xi\xi_i+\eta\eta_i+\zeta\zeta_i) \tag{3.17}$$

$$\frac{\delta N_i}{\delta \eta} = \frac{1}{8}\eta_i(1+\xi\xi_i)(1+\zeta\zeta_i)(-1+\xi\xi_i+2\eta\eta_i+\zeta\zeta_i) \tag{3.18}$$

$$\frac{\delta N_i}{\delta \zeta} = \frac{1}{8}\zeta_i(1+\xi\xi_i)(1+\eta\eta_i)(-1+\xi\xi_i+\eta\eta_i+2\zeta\zeta_i) \tag{3.19}$$

Node i	1	3	5	7	13	15	17	19
ξ_i	-1	1	1	-1	-1	1	1	-1
η_i	-1	-1	1	1	-1	-1	1	1
ζ_i	-1	-1	-1	-1	1	1	1	1

Nodes parallel to ξ axis:

$$N_i = \frac{1}{4}(1-\xi^2)(1+\eta\eta_i)(1+\zeta\zeta_i) \tag{3.20}$$
$$\frac{\delta N_i}{\delta \xi} = -\frac{1}{2}\xi(1+\eta\eta_i)(1+\zeta\zeta_i) \tag{3.21}$$
$$\frac{\delta N_i}{\delta \eta} = \frac{1}{4}\eta_i(1-\xi^2)(1+\zeta\zeta_i) \tag{3.22}$$
$$\frac{\delta N_i}{\delta \zeta} = \frac{1}{4}\zeta_i(1-\xi^2)(1+\eta\eta_i) \tag{3.23}$$

Node i	2	6	14	18
$(\xi_i = 0)\eta_i$	-1	1	-1	1
ζ_i	-1	-1	1	1

Nodes parallel to η axis:

$$N_i = \frac{1}{4}(1+\xi\xi_i)(1-\eta^2)(1+\zeta\zeta_i) \tag{3.24}$$
$$\frac{\delta N_i}{\delta \xi} = \frac{1}{4}(1-\eta^2)(1+\zeta\zeta_i) \tag{3.25}$$
$$\frac{\delta N_i}{\delta \eta} = -\frac{1}{2}(1+\xi\xi_i)(1+\zeta\zeta_i) \tag{3.26}$$
$$\frac{\delta N_i}{\delta \zeta} = \frac{1}{4}(1+\xi\xi_i)(1-\eta^2) \tag{3.27}$$

Node i	4	8	16	20
$(\eta_i = 0)\xi_i$	1	-1	1	-1
ζ_i	-1	-1	1	1

Nodes parallel to ζ axis:

$$N_i = \frac{1}{4}(1+\xi\xi_i)(1+\eta\eta_i)(1-\zeta^2) \tag{3.28}$$
$$\frac{\delta N_i}{\delta \xi} = \frac{1}{4}(1+\eta\eta_i)(1-\zeta^2) \tag{3.29}$$
$$\frac{\delta N_i}{\delta \eta} = \frac{1}{4}(1+\xi\xi_i)(1-\zeta^2) \tag{3.30}$$
$$\frac{\delta N_i}{\delta \zeta} = -\frac{1}{2}(1+\xi\xi_i)(1+\eta\eta_i) \tag{3.31}$$

Node i	9	10	11	12
$(\zeta_i = 0)\xi_i$	-1	1	1	-1
η_i	-1	-1	1	1

3.5.2 Jacobian

Once the shape functions have been derived we need to calculate the partial derivatives with respect to the Cartesian coordinates. Let us start by defining the Jacobian matrix,

$$\mathbf{J} = \frac{\delta(x,y,z)}{\delta(\xi,\eta,\zeta)} = \begin{bmatrix} \frac{\delta\xi}{\delta x} & \frac{\delta\eta}{\delta x} & \frac{\delta\zeta}{\delta x} \\ \frac{\delta\xi}{\delta y} & \frac{\delta\eta}{\delta y} & \frac{\delta\zeta}{\delta y} \\ \frac{\delta\xi}{\delta z} & \frac{\delta\eta}{\delta z} & \frac{\delta\zeta}{\delta z} \end{bmatrix} \tag{3.32}$$

The inverse of the Jacobian is used with the derivative of the shape functions with regard to natural coordinates, as seen in the equation below, to determine the derivatives with regard to the Cartesian coordinates. In matrix form

$$\begin{bmatrix} \frac{\delta N_i}{\delta x} \\ \frac{\delta N_i}{\delta y} \\ \frac{\delta N_i}{\delta z} \end{bmatrix} = \begin{bmatrix} \frac{\delta x}{\delta\xi} & \frac{\delta x}{\delta\eta} & \frac{\delta x}{\delta\zeta} \\ \frac{\delta y}{\delta\xi} & \frac{\delta y}{\delta\eta} & \frac{\delta y}{\delta\zeta} \\ \frac{\delta z}{\delta\xi} & \frac{\delta z}{\delta\eta} & \frac{\delta z}{\delta\zeta} \end{bmatrix} \begin{bmatrix} \frac{\delta N_i}{\delta\xi} \\ \frac{\delta N_i}{\delta\eta} \\ \frac{\delta N_i}{\delta\zeta} \end{bmatrix} \tag{3.33}$$

3.5.3 Strain-Displacement Matrix

Once the shape function derivatives are obtained it is necessary to calculate the strain displacement matrix for the hexahedral element.

$$\mathbf{B} = \begin{bmatrix} \frac{\delta N_1}{\delta x} & 0 & 0 & \dots & \frac{\delta N_n}{\delta x} & 0 & 0 \\ 0 & \frac{\delta N_1}{\delta y} & 0 & \dots & 0 & \frac{\delta N_n}{\delta y} & 0 \\ 0 & 0 & \frac{\delta N_1}{\delta z} & \dots & 0 & 0 & \frac{\delta N_n}{\delta z} \\ \frac{\delta N_1}{\delta y} & \frac{\delta N_1}{\delta x} & 0 & \dots & \frac{\delta N_n}{\delta y} & \frac{\delta N_n}{\delta x} & 0 \\ 0 & \frac{\delta N_1}{\delta z} & \frac{\delta N_1}{\delta y} & \dots & 0 & \frac{\delta N_n}{\delta z} & \frac{\delta N_n}{\delta y} \\ \frac{\delta N_1}{\delta z} & 0 & \frac{\delta N_1}{\delta x} & \dots & \frac{\delta N_n}{\delta z} & 0 & \frac{\delta N_n}{\delta x} \end{bmatrix} \tag{3.34}$$

3.5.4 Isoparametric Stiffness Matrix

The element stiffness matrix is then given by

$$\mathbf{K} = \int_V \mathbf{B}^T \mathbf{E} \mathbf{B} dV \tag{3.35}$$

which in numerically integrated using a Gauss Quadrature integration method with three Gauss points in each of the natural coordinate directions which implies 27 integration points. It is also assumed that the stress-strain matrix is constant.

$$\mathbf{K} = \sum_{i=1}^{p_1} \sum_{i=1}^{p_3} \sum_{i=1}^{p_3} w_i w_j w_k \mathbf{B}_{ijk}^T \mathbf{E} \mathbf{B}_{ijk} J_{ijk} \tag{3.36}$$

In the initial stage of the algorithm development, a software package called CalculiX was used to verify the Isoparametric Stiffness Matrix. CalculiX performs the same functions as commercial FEM software, however, it gives the user the option to output the mass and stiffness matrices for the structure being analysed. This feature was used to verify the matrices produced by the algorithm for a very small model with only one or two elements.

3.5.5 Solution Method

Once the isoparametric stiffness matrix has been created for each element, a global stiffness matrix is created by combining the element matrices according to the global node numbering. This set of linear equations along with the applied force vector, Equation 3.9, now need to be solved to provide us with nodal displacements. As mentioned previously, Gauss Elimination was applied to obtain these results. Refer to Chapter 6 for verification of the displacement results.

Chapter 4

Aerodynamic Model

4.1 Introduction

This chapter discusses all aspects pertaining to the Aerodynamic Component of the Aeroelastic analysis. We start by looking at the aerodynamic assumptions made when creating the aerodynamic model of the generic wing-like structure.The airfoil chosen for the experimental work is characterized and the aerodynamic algorithm discussed.

4.2 Aerodynamic Assumptions

- Density and viscosity are altitude and temperature dependent. Let us, therefore, initially assume that the simulation will occur under conditions that match the experimental testing facility. Therefore, we assume standard temperature and pressure, i.e. 20℃ and 101.325 kPa
- Assume incompressible flow, i.e. constant density. The condition for incompressible flow is that the mach number, M_a, is smaller that 0.3, with $M_a = \frac{V}{a}$ [24]. As an initial approximation this is a valid assumption since experimental facilities will limit the range of verifiable data. This also implies that the flow remains subsonic. Later developments can add a component for compressible flow which will need to be verified by relevant literature.
- Assume inviscid flow, i.e. no viscosity or no friction.
- As a result of the above assumptions, the following form of Bernoulli's equation can be used: $P_2 + \frac{1}{2}\rho_2 V_2^2 = P_1 + \frac{1}{2}\rho_1 V_1^2$. This is a form of the Law of Conservation of Energy [17].

- As a first step in this investigation, let us assume that a rectangular, straight wing-like structure, with an airfoil profile is used. The profile itself is discussed in Section 4.3.
- It is assumed that all surfaces are perfectly smooth.
- The effects of a fuselage will be ignored during this investigation.
- It is assumed that the aeroplane is statically stable with the nose pointing into the relative airflow. Static stability is the vehicles ability to remain in a state of equilibrium at a given trim setting [31].
- Any resultant forces on the wing-structure will translate or rotate the airfoil profile but not change the shape of the profile.
- Initially, control surfaces will be excluded from the structural analysis.
- Investigations near and at flutter regions are very complex, and while important will not be considered at this stage.

4.2.1 Lifting Line Theory

An explanation of Prandtl's Lifting Line Theory starts with a discussion of Helmholtz's theorems for vortex filaments [32].

1. If a fluid is irrotational, it must remain irrotational
2. The circulation strength of a vortex filament remains constant
3. A vortex filament extends downstream to infinity or remains in a closed loop

As an initial estimation, the flowfield can be represented by a single horseshoe vortex. However, to adhere to Helmholtz's theorems, this would imply a constant circulation strength along the span of the wing and this is an incorrect assumption. The lift actually decreases to zero at the tips of the wing, Figure 4.1. This leads to Prandtl's Lifting Line Theory where several horseshoe vortices of varying spans are superimposed to gain a more accurate circulation distribution. All the horseshoe vortices are bound to the lifting line which lies on the quarter chord position.

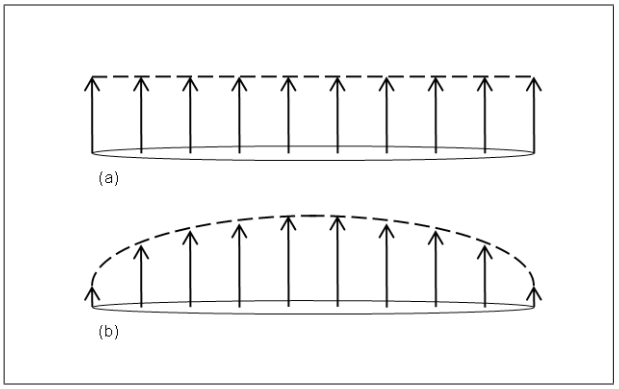

Figure 4.1: Lift Distribution over wing span. (a) Initial estimate with only one horseshoe vortex. (b) Prandtl Lifting Line Theory with multiple horseshoes.

If we assume the span-wise lift distribution to be elliptical in shape, we can represent the vortex line strength using a Fourier series, Equation 4.1.

$$\Gamma(y) = \Gamma(\Theta) = 4sV_\infty \sum_{n=1}^{\infty} A_n \sin(n\Theta) \tag{4.1}$$

Vortices occurring at the tip of the wing produce a downwash velocity which implies that a finite wing will experience less lift at a specific angle of attack. The downwash can be described by the Biot-Savart law mentioned in Section 2. Making use of Helmholtz's second theorem we can describe the local sheet strength by Equation 4.3. Combining these two equations and integrating over all the trailing sheets we can determine the downwash velocity distribution over the span of the wing, Equation 4.4,

$$dw = -\frac{\gamma \delta y}{4\pi(y_0 - y)} \tag{4.2}$$

$$\gamma = \frac{\delta \Gamma}{\delta y} \tag{4.3}$$

$$w_{ind} = -\frac{1}{4\pi} \int_{-b/2}^{b/2} \frac{\delta \Gamma}{\delta y} \frac{\delta y}{y_0 - y} \tag{4.4}$$

with w the downwash velocity,γ the local sheet strength, b the wing span and y the distance along the span being measured from the wing root. By mapping an angle, Θ, to the semi-span position (Equation 4.5), and substituting Equation 4.1, we can transform the downwash equation into a Fourier Series, see Equation 4.6.

$$y = s\cos(\Theta) \tag{4.5}$$

$$w_{ind} = V_\infty \sum_{n=1}^{\infty} \frac{nA_n \sin(n\Theta)}{\sin(\Theta)} \tag{4.6}$$

Finite wings have two velocity components, the freestream velocity and the downwash velocity described above. The relationship between these two velocities results in an induced angle of attack seen in Equation 4.7. However, the downwash is generally small in comparison with the freestream velocity and we can approximate Equation 4.7 with Equation 4.8 [33].

$$\alpha_i = \tan^{-1}\frac{w_{ind}}{V_\infty} \tag{4.7}$$

$$\alpha_i = \frac{w_{ind}}{V_\infty} \tag{4.8}$$

The three dimensional angle of attack can therefore be defined according to Equation 4.9, which is the sum of the two dimensional angle of attack (α_{2D}), the induced angle of attack (α_i) and the geometric wing twist angle (θ_t).

$$\alpha_{2D} = \alpha_{3D} - \alpha_i + \theta_t \tag{4.9}$$

It is then possible to write the section lift coefficient as follows:

$$C_l = a_0(\alpha_{2D} - \alpha_0) = \frac{\Gamma}{V_\infty c} \tag{4.10}$$

where a_0 is the section lift slope and α_0 is the section zero lift angle. Rearranging the terms and including Equation 4.9 the vortex line strength can be written as:

$$\Gamma = \frac{1}{2}a_0 V_\infty c(\alpha_{3D} - \alpha_i + \theta_t - \alpha_0) \tag{4.11}$$

The next step is to combine Equations 4.6, 4.8 and 4.11 into Equation 4.12 and to solve for the Fourier Coefficients.

$$\sum_{n=1}^{\infty} A_n \sin(n\Theta)\left(\sin(\Theta) + \frac{na_0 c}{8s}\right) = \frac{a_0 c}{8s}\sin(\Theta)(\alpha_{3D} + \theta_t - \alpha_0) \tag{4.12}$$

If the loading on the wing is symmetric about the wing root then all even Fourier Coefficients are zero. Using Gauss Elimination to solve for the Fourier Coefficients, we can find the Lift and Drag Coefficients as seen in Equations 4.13 and 4.14,

$$C_L = \pi \text{Æ} A_1 \tag{4.13}$$

$$C_{Di} = \pi \text{Æ} \sum_{n=1}^{\infty} n A_n^2 \tag{4.14}$$

$$\text{Æ} = \frac{b^2}{S} \tag{4.15}$$

$$e = \frac{1}{1 + \sum_{n=2}^{\infty} (n A_n^2 / A_1^2)} \tag{4.16}$$

with S the planform area of the wing.

The implementation of this theory can be seen in Section 4.4

4.3 Airfoil Characterisation

As with the structural component, we need to make use of an aerodynamic model that can be used for verification of the aerodynamic algorithm as well as experimental work. To this end, an airfoil profile was chosen for its simple profile and ease of manufacture; specifically, the Clark-Y airfoil. This airfoil is defined with the bottom surface forming a straight line after the 30% chord position. The Clark-Y airfoil is a well known profile which has been used in many experimental investigations, and there is therefore, a large amount of characterisation and documentation on this specific airfoil.

The profile was obtained of a Clark-Y airfoil with a unit chord length. This could then be scaled to suit the experimental or analysis needs.

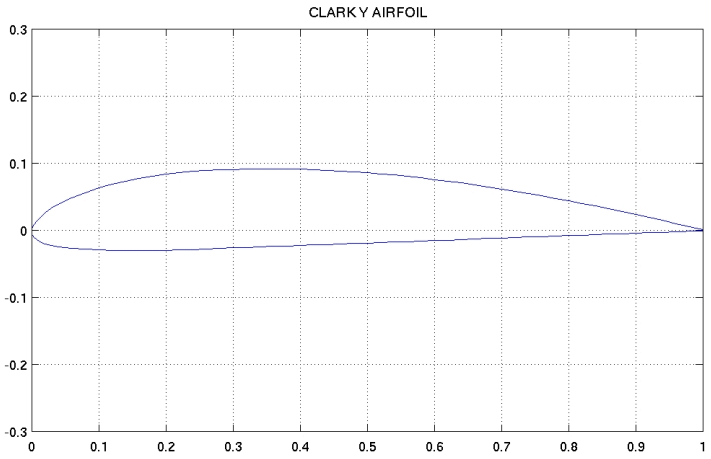

Figure 4.2: Clark-Y airfoil profile with a unit chord length.

The airfoil profile was characterised using freeware called AVL (Athena Vortex Lattice). This software makes use of Vortex Lattice Modelling as described in Chapter 2. It is suitable for the analysis of thin lifting surfaces undergoing small changes in angle of attack and side slip.

This Vortex Lattice formulation represents the wing surfaces and wakes as single layer vortex sheets which have been discretized into horseshoe filaments. Discretization occurs chordwise and spanwise with either a sine or cosine distribution. The effect of the grid density was investigated by doubling the number of horseshoe filaments in both the chordwise and spanwise directions. Figure 4.3 shows that the results have converged with a 32 x 40 grid. Figure 4.4 shows the converged horseshoe filament distribution.

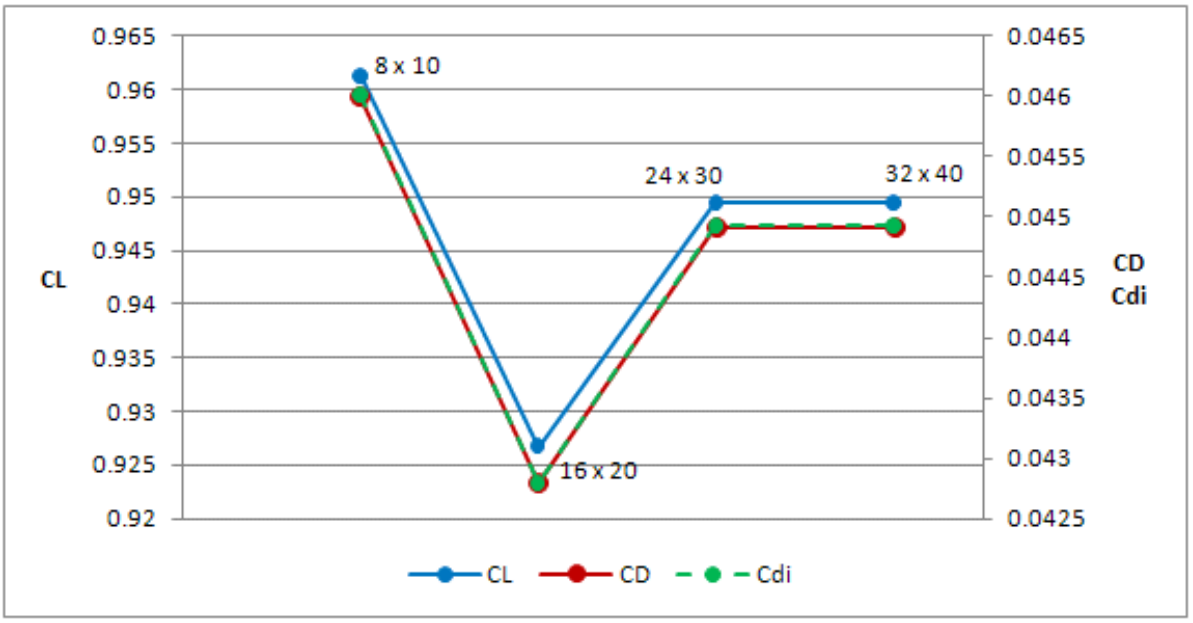

Figure 4.3: Mesh Convergence study performed in AVL.

Five models were evaluated in AVL, corresponding to the five experimental setups to be evaluated at the low-speed wind tunnel. The Clark-Y profile was evaluated at angles of attack varying from $-10°$ to $+10°$ at intervals of $5°$. Figures 4.6 to 4.8 show the coefficients of lift and induced angle of attack distribution along the wing span. These parameters are calculated on the Trefftz plane.

The Trefftz plane is defined as a plane perpendicular to the wake at an infinite distance downstream from the airfoil. Figure 4.5 summarises the effect of angle of attack on the lift and drag coefficients. We see that for $-10°$ AOA the lift coefficient is very small, implying no lift force on the wing under this condition. This corresponds to Figure 4.8 where the lift distribution is not elliptical over the span as it would be under ideal conditions. We can also see from Figure 4.5 that there is an optimum AOA where the lift coefficient is high while the drag coefficient is small, between $0°$ and $5°$ AOA.

The input files used to generate the geometry in AVL can be seen in Appendix A.

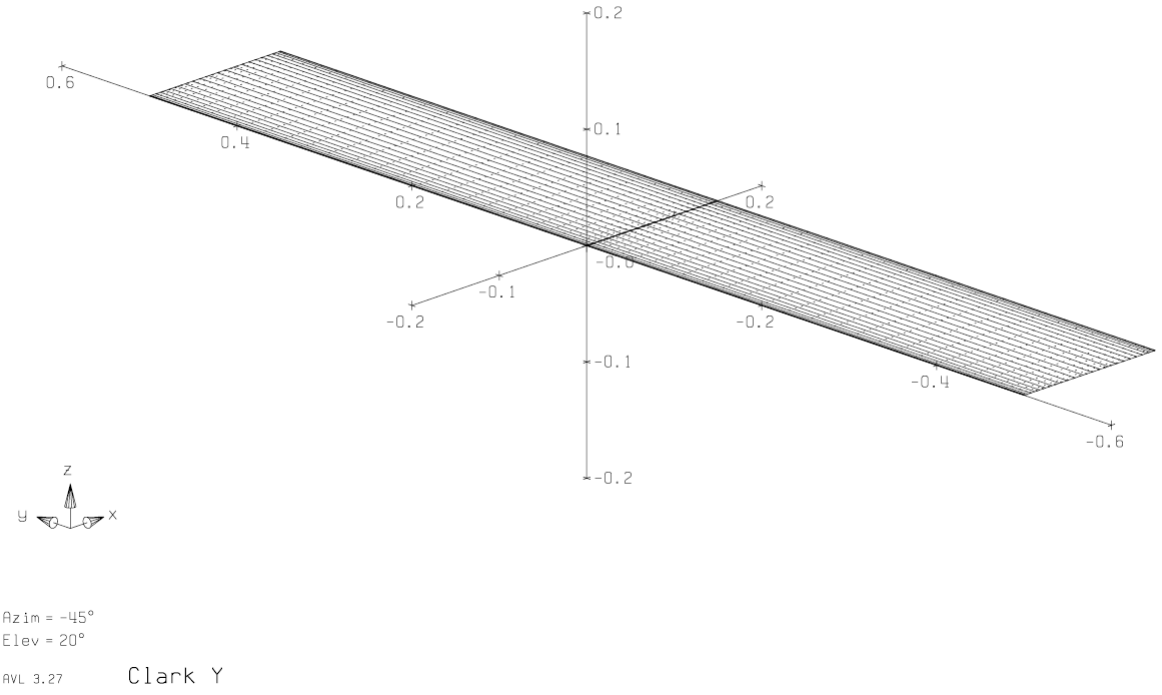

(a) Lifting Surface (32 x 40 grid)

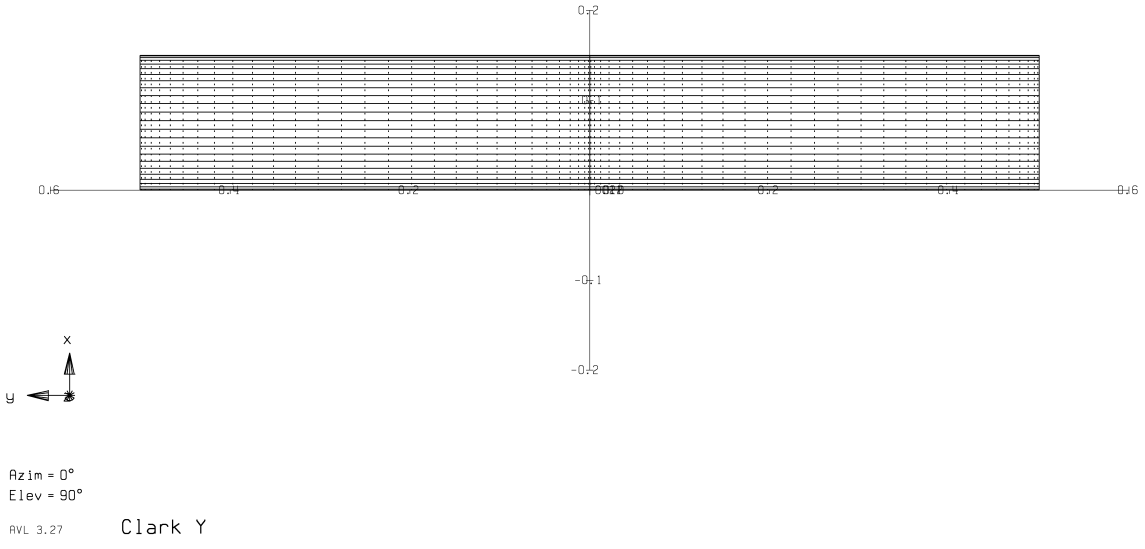

(b) Lifting Surface (32 x 40 grid) - Top View

Figure 4.4: Lifting Surface Geometry for a 32 x 40 grid co-sine distribution.

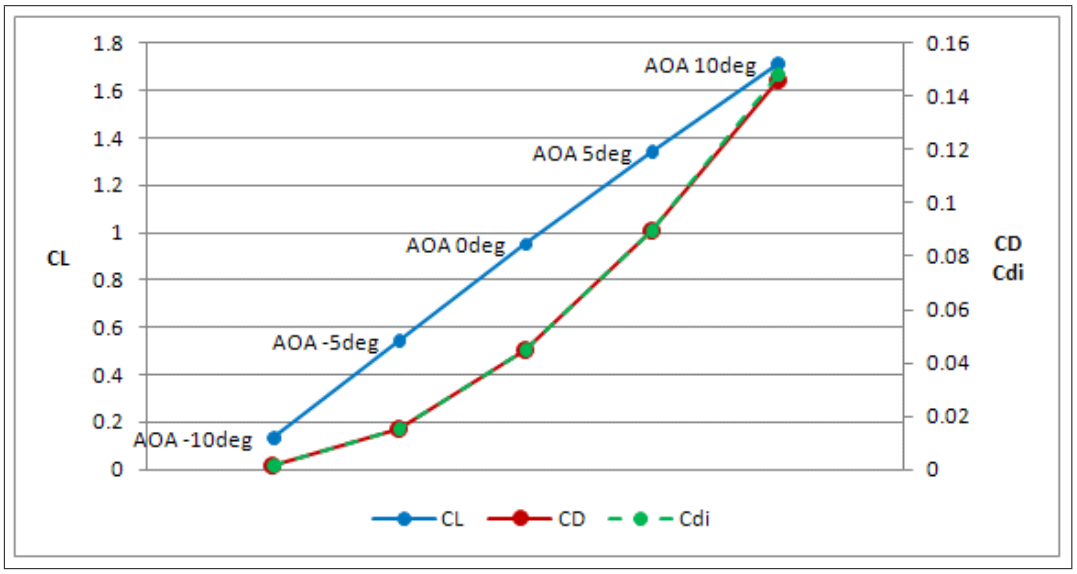

Figure 4.5: Summary of Clark Y Airfoil Characteristics (32 x 40 grid).

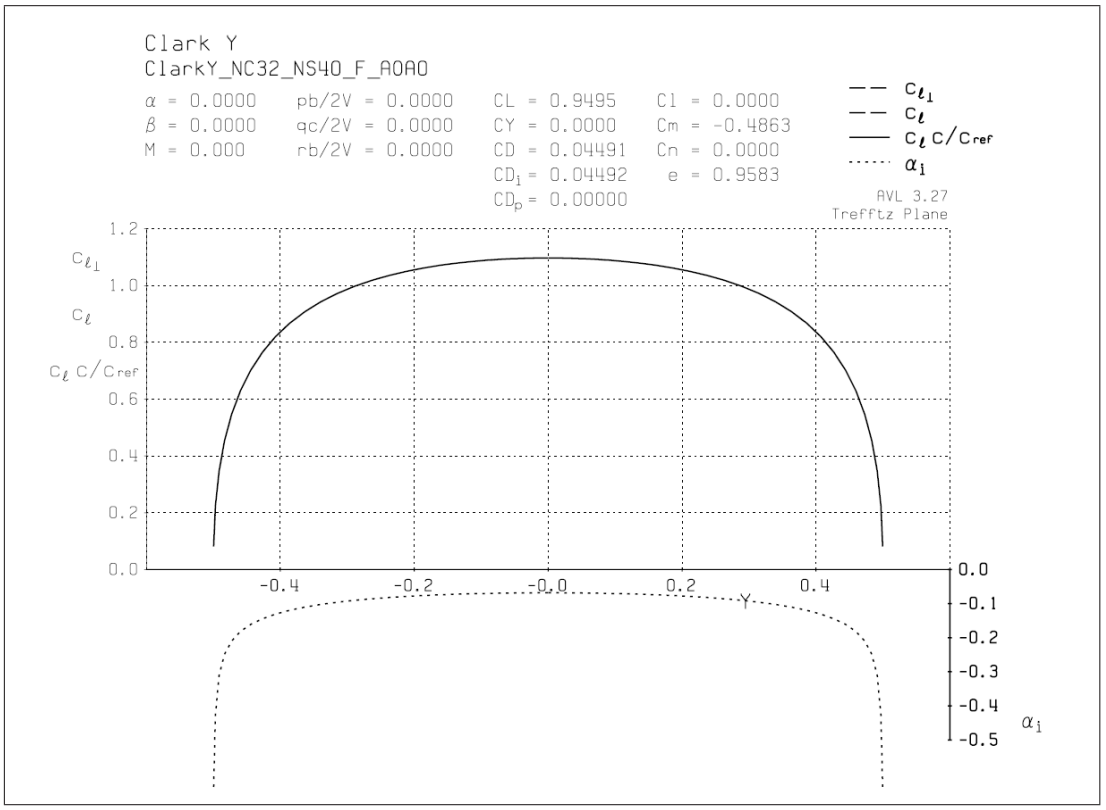

Figure 4.6: Clark Y Airfoil Characteristics at 0° angle of attack (32 x 40 grid).

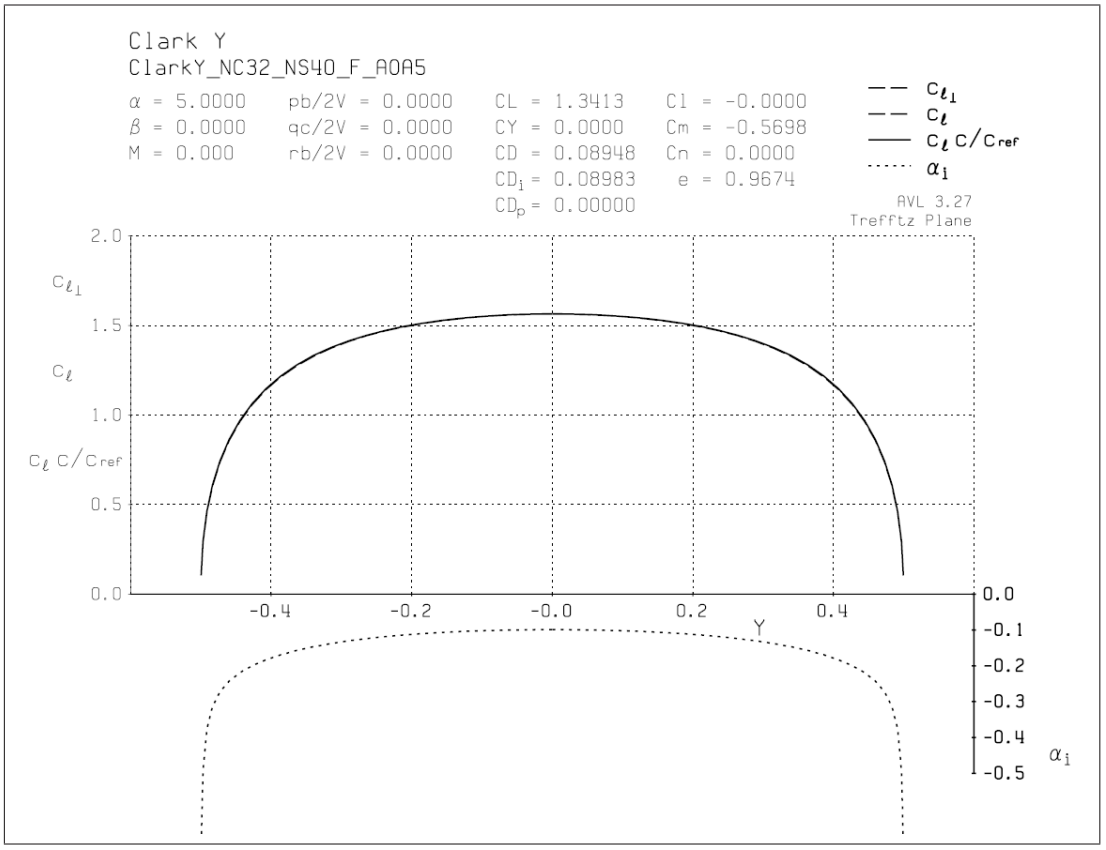

(a) 5° angle of attack

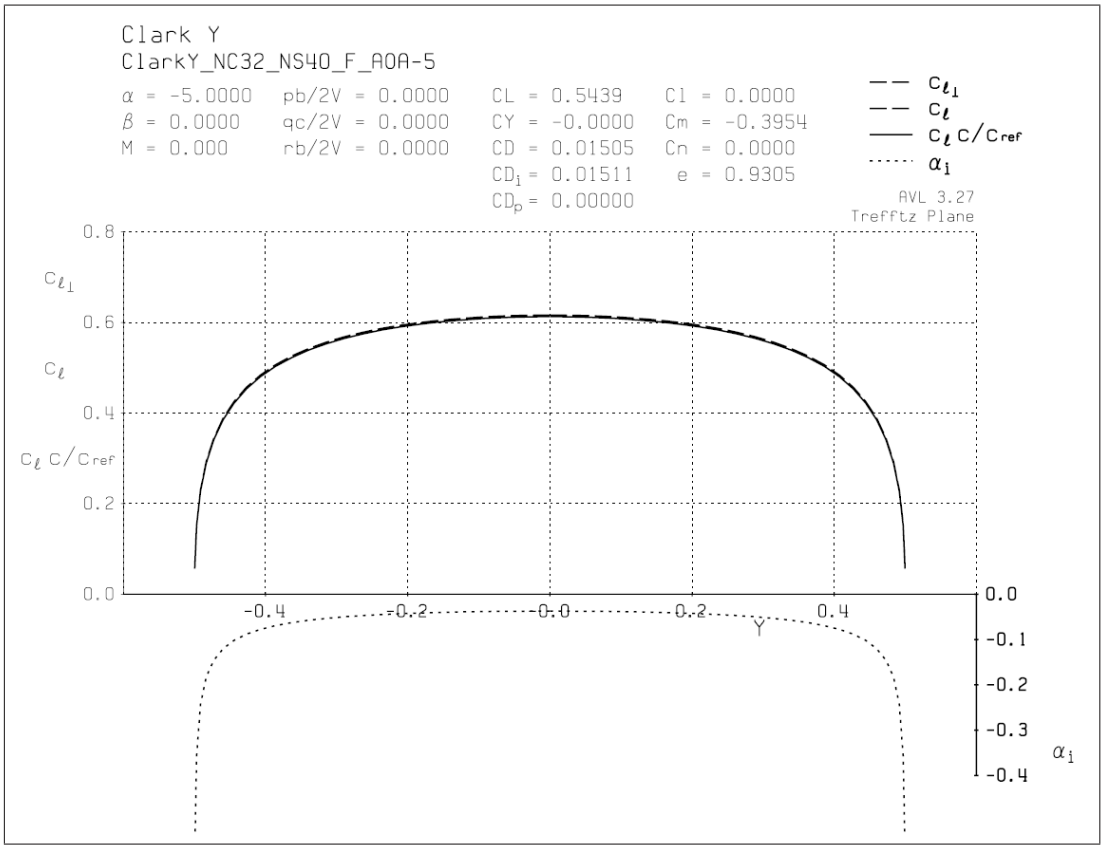

(b) −5° angle of attack

Figure 4.7: Clark Y Airfoil Characteristics at ±5° angle of attack (32 x 40 grid).

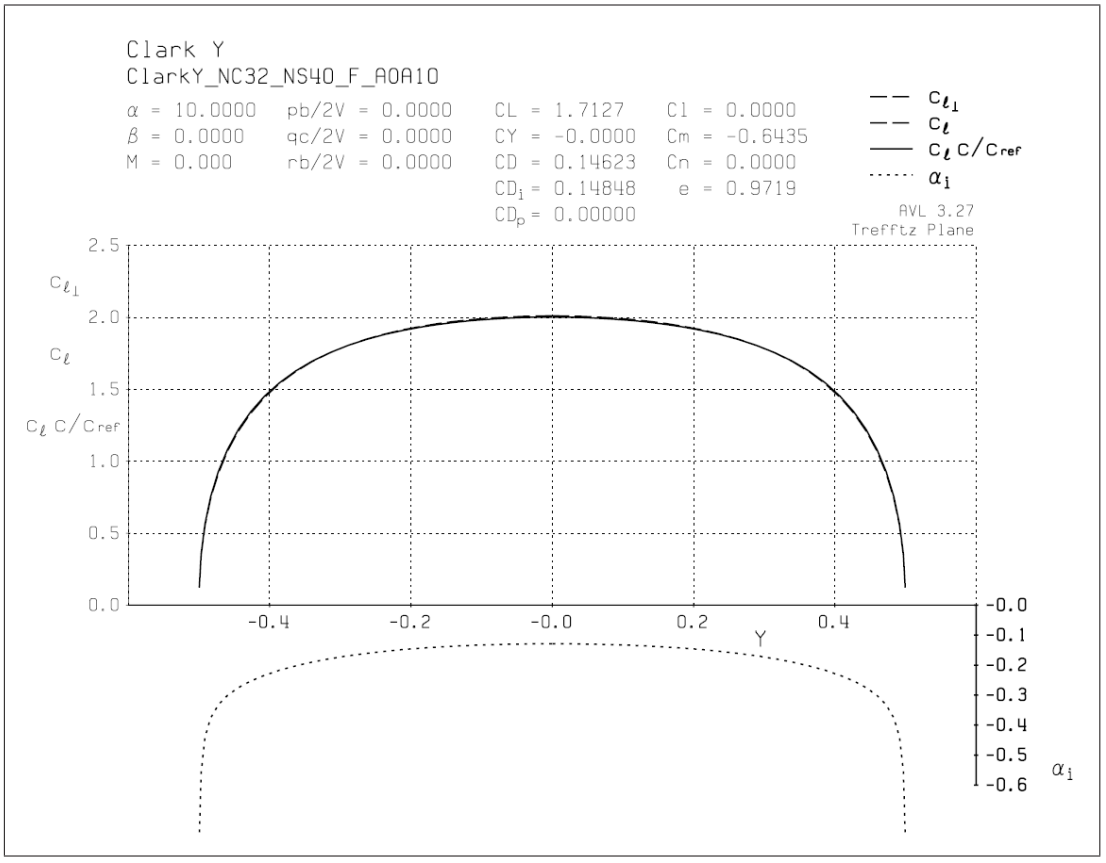

(a) 10° angle of attack

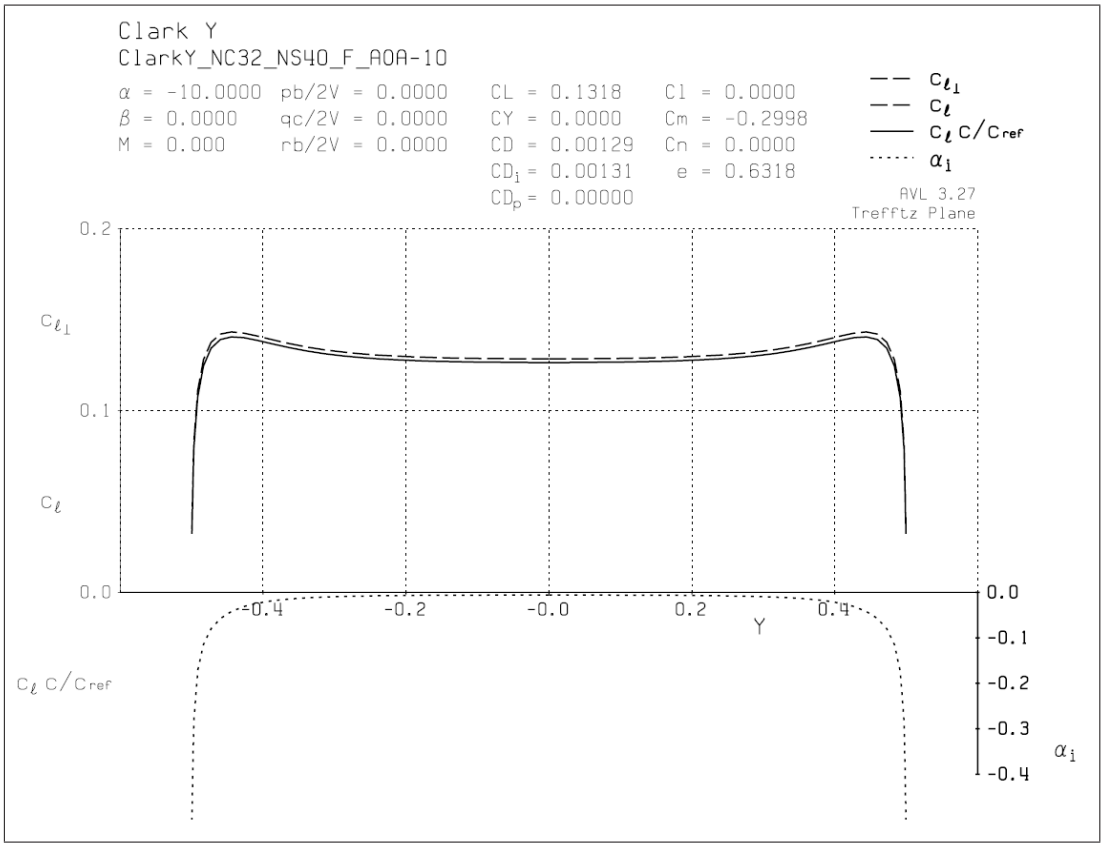

(b) −10° angle of attack

Figure 4.8: Clark Y Airfoil Characteristics at ± 10° angle of attack (32 x 40 grid).

4.4 Aerodynamic Algorithm

This section describes the aerodynamic algorithm that was used to determine the loading on the wing structure for a given air speed and angle of attack. The structure of the aerodynamic model can be seen in Figure 4.9. Each of the indicated subdivisions will be discussed.

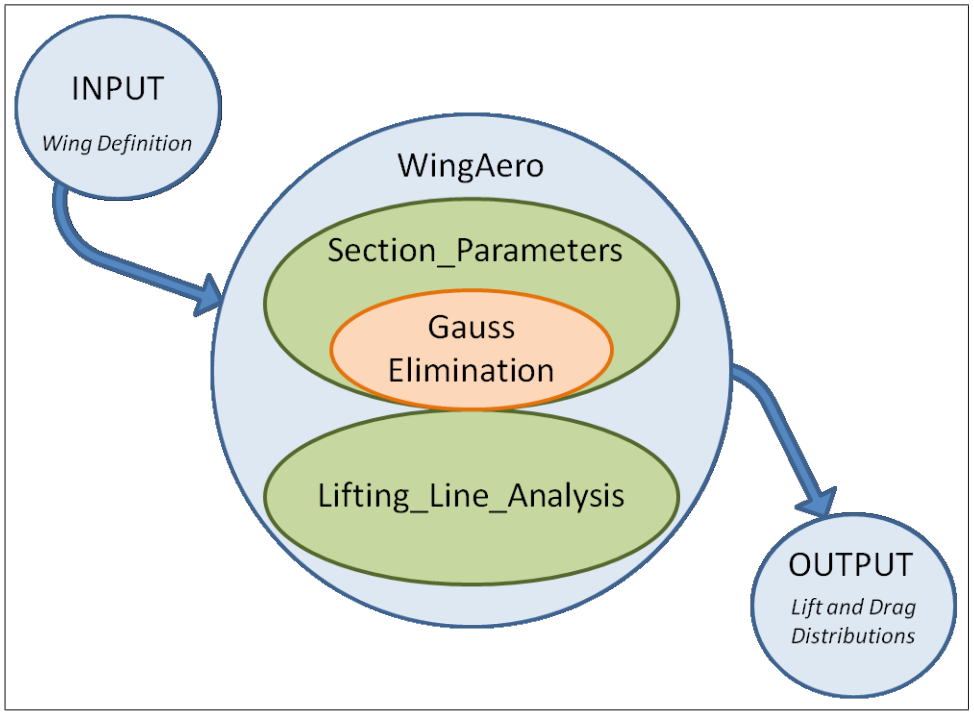

Figure 4.9: Aerodynamic Model function Flow.

The aerodynamic model is based on code developed by the late Professor G. Thiart. Originally coded in Fortran, the author transcribed the code to C since this program language was more familiar to the author. The code was verified using a sample results set generated by the Fortran version. The aerodynamic model has two main functions, the first calculates section properties while the second performs a lifting line analysis and determines the lift and drag on all sections of the wing as well as the induced angle of attack. Let us start by looking at the inputs to the aerodynamic model.

4.4.1 Input

The input file is prepared by the user and contains the following information regarding the airfoil profile, refer to Figure 4.10 for more insight into the input parameters:

- $wing_{span}$ - The total wingspan of the structure
- $nsect$ - The number of sections along the wingspan
- $nSurf_{max}$ - The largest number of surfaces in any of the sections
- $nSurf_i$ with $i = 1 : nsect$ - The number of surfaces in a section
- $XSect_i$ with $i = 1 : nsect$ - X co-ordinate of section
- $YSect_{i,j}$ with $i = 1 : nsect$ and $j = 1 : nSurf_i$ - Y co-ordinate of section
- $ZSect_{i,j}$ with $i = 1 : nsect$ and $j = 1 : nSurf_i$ - Z co-ordinate of section

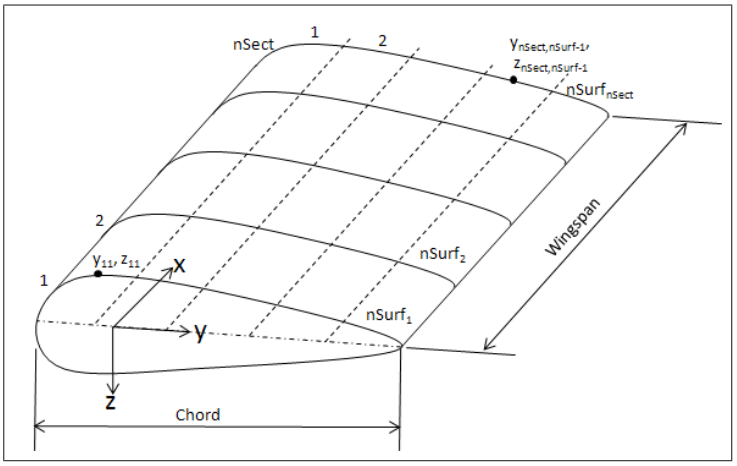

Figure 4.10: Aerodynamic Input Parameters

4.4.2 Section Parameters

The goal of the Section Parameters function is to determine the section zero lift angle, α_0, and the section lift slope, a_0. Let us assume the wing structure is broken up as shown in Figure 4.10, with a number of sections and each section made up of a number of surfaces. Keep in mind that the number of surfaces needed per section does not need to remain constant and may vary with section, i.e. $nSurf_{Max} = MAX(nSurf_{1...nSect})$

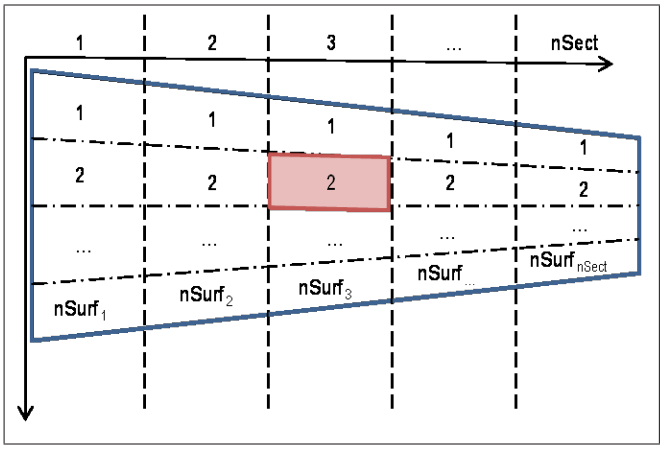

Figure 4.11: Sections and Surfaces for a generic wing-like structure.

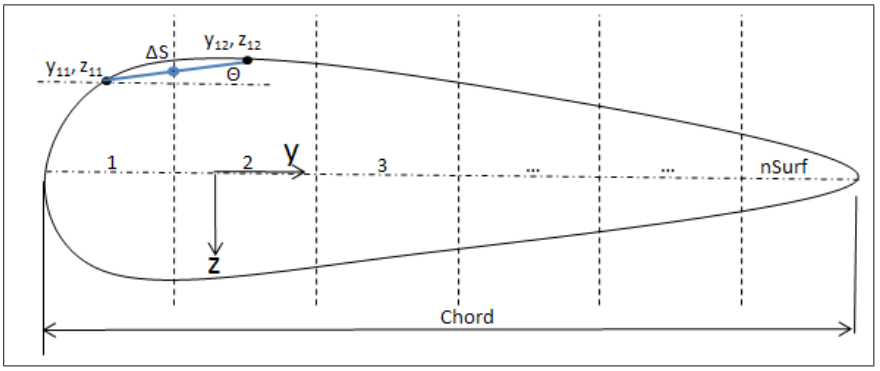

Figure 4.12: Parameters used in Algorithm 4.1

This function starts with the determination of surface centroids or control points,panel lengths and panel angles for each surface of each section.

Algorithm 4.1: Section Parameters, also refer to Figure 4.12.

for $i = 1$ **to** $nSect$ **do**
  for $j = 1$ **to** $nSurf_i$ **do**
    $yCent_{i,j} = \frac{1}{2}(YSect_{i,j} + YSect_{i,j-1})$
    $zCent_{i.j} = \frac{1}{2}(ZSect_{i,j} + ZSect_{i,j-1})$
    $\Delta S_{i,j} = \sqrt{(ZSect_{i,j} - ZSect_{i,j-1})^2 + (YSect_{i,j} - YSect_{i,j-1})^2}$
    $\Theta_{i,j} = \arctan\left(\frac{ZSect_{i,j} - ZSect_{i,j-1}}{YSect_{i,j} - YSect_{i,j-1}}\right)$
  end
end

The next step is calculating the influence coefficients,i.e. the effect of each surface on the other surfaces in a specific section. Let us assume we are looking at section p.

Algorithm 4.2: Influence Coefficients

for $j = 1$ **to** $nSurf_p$ **do**
  for $k = 1$ **to** $nSurf_p$ **do**
    if $j = k$ **then**
      $\text{inflC}_{j,k} = Im(-\pi) \cdot e^{Im(-\Theta_{p,j})}$
    else if $j \neq k$ **then**
      $\text{inflC}_{j,k} = e^{Im(-\Theta_{p,j})} \cdot \log\left(\frac{Re(yCent_{p,k})+Im(zCent_{p,k})-Re(ySect_{p,j-1})-Im(zSect_{p,j-1})}{Re(yCent_{p,k})+Im(zCent_{p,k})-Re(ySect_{p,j})-Im(zSect_{p,j})}\right)$
  end
end

These influence coefficients are used to create a weighting matrix Σ which quantifies the effect of a surface on the surrounding surfaces. Algorithm 4.3 shows how the coefficient matrices are created. This system of equations can then be solved to determine Σ using Gauss Elimination, which is discussed in Section 4.4.3. Assume we are looking at a specific section p.

Algorithm 4.3: Influence Coefficient Matrices to be used with Gauss Elimination to solve for the Weighting Matrix Σ

for $k = 1$ **to** $nSurf_p$ **do**
  $LHS_{k,nSurf_p+1} = 0.0$
  for $j = 1$ **to** $nSurf_p$ **do**
    $LHS_{k,j} = Re(\text{inflC}_{j,k} \cdot \sin(\Theta_{p,k})) + Im(\text{inflC}_{j,k} \cdot \cos(\Theta_{p,k}))$
    $LHS_{k,nSurf_p+1} =$
    $LHS_{k,nSurf_p+1} - Re(\text{inflC}_{j,k} \cdot \cos(\Theta_{p,k})) + Im(\text{inflC}_{j,k} \cdot \sin(\Theta_{p,k}))$
  end
  $RHS_{k,1} = -\sin(\Theta_{p,k})$
  $RHS_{k,2} = \cos(\Theta_{p,k})$
end
$LHS_{nSurf_p+1,nSurf_p+1} = 0.0$
for $y = 1$ **to** $nSurf_x$ **do**
  $LHS_{nSurf_p+1,j} = Re(\text{inflC}_{j,1} \cdot \cos(\Theta_{p,1})) + Re(\text{inflC}_{j,nSurf_p} \cdot \cos(\Theta_{p,nSurf_p})) - Im(\text{inflC}_{j,1} \cdot \sin(\Theta_{p,1})) - Im(\text{inflC}_{j,nSurf_p} \cdot \sin(\Theta_{p,nSurf_p}))$
  $LHS_{nSurf_p+1,nSurf_p+1} =$
  $LHS_{nSurf_p+1,nSurf_p+1} + Re(\text{inflC}_{j,1} \cdot \sin(\Theta_{p,1})) + Re(\text{inflC}_{j,nSurf_p} \cdot \sin(\Theta_{p,nSurf_p})) + Im(\text{inflC}_{j,1} \cdot \cos(\Theta_{p,1})) + Im(\text{inflC}_{j,nSurf_p} \cdot \cos(\Theta_{p,nSurf_p}))$
end
$RHS_{nSurf_p+1,1} = -\cos(\Theta_{p,1}) - \cos(\Theta_{p,nSurf_p})$
$RHS_{nSurf_p+1,2} = -\sin(\Theta_{p,1}) - \sin(\Theta_{p,nSurf_p})$

Once Σ has been determined, we can calculate the resulting perturbation velocities.

Algorithm 4.4: Perturbation Velocities.

for $j = 1$ **to** $nSurf_p$ **do**
  for $k = 1$ **to** $nSurf_p$ **do**
    for $dim = 1$ **to** 2 **do**
      $VSect_{p,k,dim} = VSect_{p,k,dim} + Re(\text{inflC}_{j,k} \cdot \Sigma_{j,dim})$
      $+Im(\text{inflC}_{j,k} \cdot \Sigma_{nSurf_p+1,dim})$
      $WSect_{p,k,dim} = WSect_{p,k,dim} + Re(\text{inflC}_{j,k} \cdot \Sigma_{nSurf_p+1,dim})$
      $-Im(\text{inflC}_{j,k} \cdot \Sigma_{j,dim})$
    end
  end
end

Then, using a reference initial angle, the lift and drag forces can be calculated at each section.

Algorithm 4.5: Lift and Drag Forces

for $j = 1$ **to** $nSurf_p$ **do**

$Press_{j,1} = 1 - [(1 + VSect_{p,j,1})\cos(\alpha_{ref}) - Vsect_{p,j,2}\sin(\alpha_{ref})]^2 - [WSect_{p,j,1}\cos(\alpha_{ref}) - (1 + WSect_{p,j,2})\sin(\alpha_{ref})]^2$

$Press_{j,2} = 1 - [(1 + VSect_{p,j,1})\cos(\alpha_{ref}) + Vsect_{p,j,2}\sin(\alpha_{ref})]^2 - [WSect_{p,j,1}\cos(\alpha_{ref}) + (1 + WSect_{p,j,2})\sin(\alpha_{ref})]^2$

$Lift_{p,1} = Lift_{p,1} - Press_{j,1} \cdot \cos(\Theta_{p,j} + \alpha_{ref}) \cdot \Delta S_{p,j}$

$Lift_{p,2} = Lift_{p,2} - Press_{j,2} \cdot \cos(\Theta_{p,j} - \alpha_{ref}) \cdot \Delta S_{p,j}$

$Drag_{p,1} = Drag_{p,1} + Press_{j,1} \cdot \cos(\Theta_{p,j} + \alpha_{ref}) \cdot \Delta S_{p,j}$

$Drag_{p,2} = Drag_{p,2} + Press_{j,2} \cdot \cos(\Theta_{p,j} - \alpha_{ref}) \cdot \Delta S_{p,j}$

end

Using the Lift calculated in Algorithm 4.5, the section zero lift angle, α_0, and the section lift slope, a_0, can be calculated according to Algorithm 4.6

Algorithm 4.6: Sectional Lift Parameters

for $p = 1$ **to** $nSect$ **do**

$\alpha_0(p) = \arctan\left[\frac{\tan(\alpha_{ref})(Lift_{p,1}+Lift_{p,2})}{Lift_{p,1}-Lift_{p,2}}\right]$

$a_0(p) = \frac{1}{2}\sqrt{\left(\frac{Lift_{p,0}-Lift_{p,1}}{\sin(\alpha_{ref})}\right)^2 + \left(\frac{Lift_{p,0}+Lift_{p,1}}{\sin(\alpha_{ref})}\right)^2}$

end

4.4.3 Gauss Elimination

Gaussian Elimination is a tool for solving sets of linear equations. Unlike the Gauss-Jordon elimination method, it only reduces the matrix to have only components on the diagonal and above and not to an identity matrix. Back substitution is then used to solve the set of equations [34]. The algorithm can be seen below. Let us assume our systems of equations looks as follows: $Ax = b$ with A being a square matrix with dimensions nxn

Algorithm 4.7: Gauss Forward Elimination

```
for r = 1 to n − 1 do
    s = r
    for t = r + 1 to n do
        if |A_{t,r}| = |A_{s,r}| then
            s = t
    end
    if s ≠ r then
        for u = r to n do
            Swop (A_{r,u}, A_{s,u})
        end
        Swop (b_r, b_s)
    for t = r + 1 to n do
        factor = A_{t,r}/a_{r,r}
        for u = r + 1 to n do
            A_{t,u} = A_{t,u} − factor · A_{r,u}
        end
        b_t = b_t − factor · b_r
    end
end
```

Algorithm 4.8: Backward Substitution

```
for t = n to 1 do
    x_t = b_t
    for u = t + 1to n do
        x_t = x_t − factor · x_u
    end
    x_t = x_t/A_{tt}
end
```

4.4.4 Lifting Line Analysis

This function implements the Prandtl Lifing Line equations discussed in Section 4.2.1. It determines the induced angle of attack by means of a Fourier Series, from which it is possible to determine the lift and drag distributions on the wing.

Algorithm 4.9 starts by mapping the semi-span position, to the angle Θ by ma-

nipulating Equation 4.5. This Θ differs from the angle used when calculating the Section Parameters. The parameter Ψ is sub-step used to simplify the formula used in Algorithm 4.10.

Algorithm 4.9: Solve for Θ and Ψ

for $p = 1$ **to** $nSect$ **do**
    $\Theta_p = \arccos(\frac{2xSect_p}{wing_{span}})$
    $\Psi_p = \frac{\frac{1}{4}cClAmpl_p}{wing_{span}}$
end

Equation 4.12 can now be split into a LH and a RH matrix so that Gauss Elimination, refer to Section 4.4.3, can be used to solve for the Fourier Coefficients. Algorithm 4.10 creates these matrices.

Algorithm 4.10: Setting up of Equations to solve for Fourier Coefficients.

for $p = 1$ **to** $nSect$ **do**
    for $j = 1$ **to** $nSect$ **do**
        $LHS_{p,j} = (\sin(\Theta_p) + (2j-1)\Psi_p) \cdot \sin((2j-1)\Theta_p)$
    end
    $RHS_{p,1} = (\alpha_p - \alpha 0_p)\Psi_p \sin(\Theta_p)$
end

Once solved, the Fourier coefficients are used in conjuction with Equation 4.8 to determine the downwash or induced angle of attack, see Algorithm 4.11.

Algorithm 4.11: Downwash Angle

for $p = 1$ **to** $nSect$ **do**
    for $j = 1$ **to** $nSect$ **do**
        $\alpha I_p = \alpha I_p + (2j-1)\text{Coeff}_{j,1} \cdot \sin((2j-1)\Theta_p)$
    end
    $\alpha I_p = \frac{\alpha I_p}{\Theta_p}$
end

Finally, Equations 4.13 and 4.14 can be used to determine the lift and induced drag coefficients of the wing which lead to the detailed force distribution of Algorithm 4.13.

Algorithm 4.12: Lift and Drag Coefficients

$cL = \pi \text{Coeff}_{1,1}$
$cDi = 0.0$
for $j = 1$ **to** $nSect$ **do**
    $cDi = cDi + (2j - 1)\text{Coeff}_{j,1}^2$
end
$cDi = \pi \cdot cDi$

We now calculate the detailed force distribution.

Algorithm 4.13: Detailed Force Distribution

for $p = 1$ **to** $nSect$ **do**
    $\alpha_{eff} = \alpha_p - \alpha I_p$
    for $j = 1$ **to** $nSurf_p$ **do**
        $Press = 1 - [(1 + VSect_{p,j,1})\cos(\alpha_{eff}) + Vsect_{p,j,2}\sin(\alpha_{eff})]^2 - [WSect_{p,j,1}\cos(\alpha_{eff}) + (1 + WSect_{p,j,2}\sin(\alpha_{eff}))]^2$
        $LiftDist_{p,j} = -Press\cos(\Theta_{p,j} - \alpha_p)\Delta S_{p,j}$
        $DragDist_{p,j} = Press\sin(\Theta_{p,j} - \alpha_p)\Delta S_{p,j}$
    end
end

Chapter 5

Experimental Work

5.1 Introduction

This chapter describes all aspects pertaining to the testing of a wing-like structure in a low speed wind tunnel. Details of the physical model as well as the procedures followed for data capture will be discussed. Experimental work is an important factor in simulation validation and verification.

5.2 Experimental Model

The literature provided several possible configurations for the evaluation of a wing-like structure in a wind tunnel as discussed in Chapter 2. The method that was implemented makes use of a half-span wing mounted to the roof of the wind-tunnel test section. This method was chosen since the low-speed wind tunnel, found at the Department of Mechanical and Mechatronic Engineering, has perspex side panels on the test section. This would make mounting the wing horizontally, as in flight, impossible. Mounting to the roof instead of the floor removes gravitational effects due to the structures own mass and eccentricity. The model co-ordinate system is oriented such that the x-axis of the model runs along the length of the span. The y-axis is in the chordwise direction and the z-axis is out of plane, refer to Figure 5.1. The following sections describe the three main components of the model; the spar or support structure, the sensor setup and the airfoil profile.

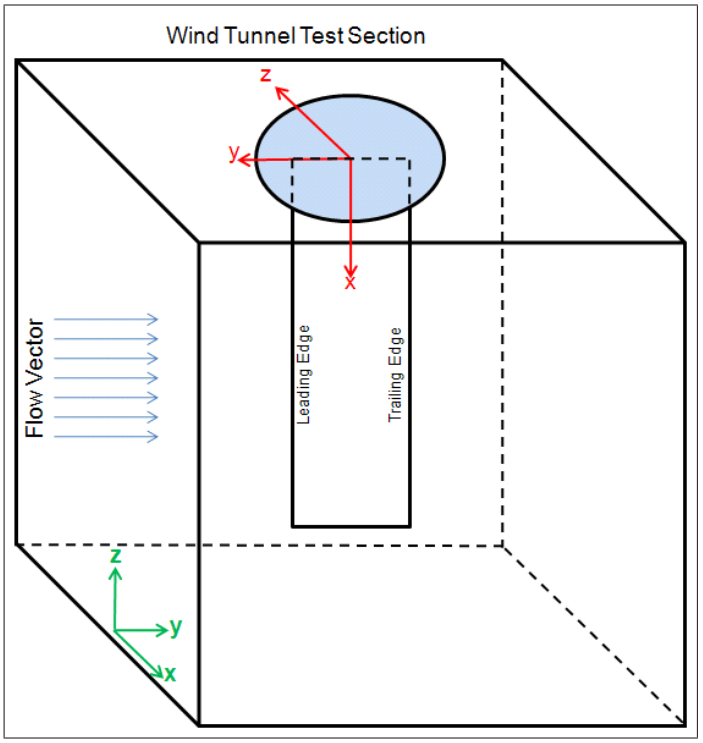

Figure 5.1: Reference co-ordinate systems used during the experimental phase. The green co-ordinate system is in reference to the wind tunnel test section while the red co-ordinate system refers to the experimental model.

5.2.1 The Spar

In this experimental setup, the spar is designed to carry all the weight and stiffness of the model wing while the airfoil is designed to transfer the aerodynamic forces. The position and structure of the spar is therefore critical to the behaviour of the wing. Three configurations for the spar have been considered, a single spar, a double spar and a flat plate. We want a simplified model that will give the same bending and torsional stiffness as the real structure. It is, therefore, customary to have all the stiffness in the spar with the covering providing only the aerodynamic shape. A static deflection test, i.e. cantilevered beam, is usually used to characterise the spar.

Single Spar A single spar could be positioned along the span at the quarter chord position. A valid assumption would be that all the aerodynamic forces act on this quarter chord position. This beam-like spar would need to have a small cross-section, typically symmetrical, in comparison with its length. Typical behaviour of a wing includes bending and torsion, however, with a single spar, the torsion component would not be visible. Even with a 2-axis sensor, the behaviour could not be accurately captured. If a single spar were to be used,

the cross-section would be that of square/rectangular tubing. This would allow placement of the sensors inside the tubing and make the fixing of the profile quite easy.

Double Spar This configuration would have a spar along the span at the quarter chord position, like that mentioned above, and include a second spar at the three-quarter chord position. From this information, the bending in the beam and some of the torsion can be extracted from the phase difference of the sensors. If single axis sensors are used it would be unclear if the profile deforms during the experiment. Dual-axis sensors would be able to pick up the movement in the horizontal or lateral planes.

Flat Plate Support This support would run the width of the chord and the length of the wing. This configuration would clearly show the behaviour of the wing under bending and torsion. This configuration would also allow the placement of many more sensors, at any location on the model and not be limited to the quarter chord position. However, the sensors would be mounted to the top or bottom surface of the plate and would, therefore, not be protected from aerodynamic forces as would a sensor in a single spar hollow tube.

Initially it was thought the complexity of the analysis when using a flat plate would be unnecessary and that a first iteration using a single spar would suffice. However, upon further investigation of the structural properties of the spar this view was modified. The ideal spar would have natural frequencies that were reasonably slow and easily excited. A structural analysis was performed on all the possible configurations of spar using *Nastran*. From this analysis, natural frequencies were obtained and showed the single spar solution to be too rigid to illustrate the deflection in the wing due to aerodynamic loading. Variations of the spar included changes in material, Table 5.1, cross-section, wall thickness and making use of laminate structures. Figure 5.2 indicates the forms of the various cross-sections that were analysed.

Results of these analyses can be seen in Table 5.2 and showed relatively high natural frequencies for the single spar configurations. Since one of the advantages of experimental work is the visualisation of the behaviour of the structure, it was felt that lower natural frequencies were preferred. This would also make data capture simpler since the range of the excitation would be larger and high tolerance sensors for very small variations would not be necessary. This would also mean the necessary sensors would be cheaper. Similarly, the Aluminium is more flexible than the steel and would therefore, produce more visible and measurable deflections.

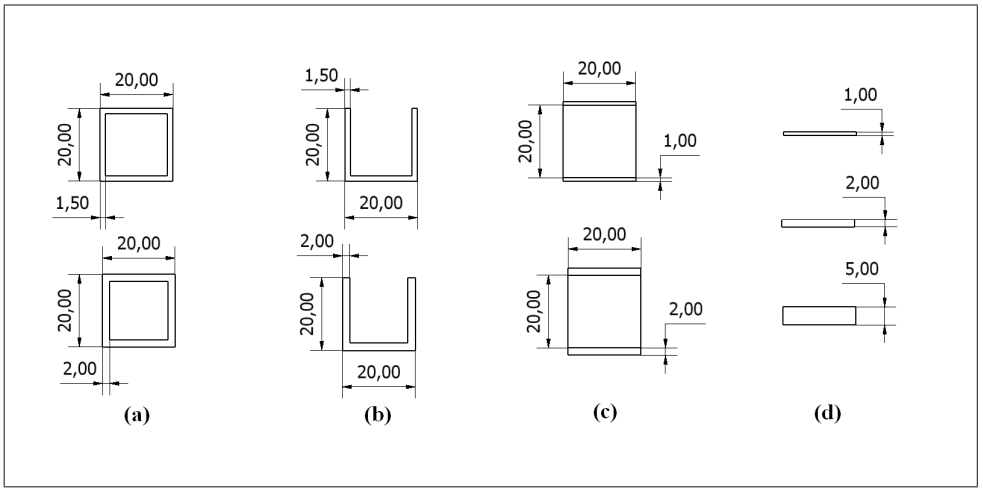

Figure 5.2: Cross-sections were created with a length of 500 mm and 600 mm: (a) Aluminium square tubing with wall thicknesses of 1.5 mm and 2 mm. (b) Aluminium U-tubing with wall thicknesses of 1.5 mm and 2 mm. (c) A laminate with combinations of Aluminium and Balsa Wood, Copper and Balsa Wood, Perspex and Balsa Wood with thicknesses of 1 mm and 2 mm. (d) Aluminium and Steel plates with a breadth of 100 mm and thicknesses of 1 mm, 2 mm and 5 mm.

Material	Young's Modulus	Shear Modulus	Poisson's Ratio	Density
Steel	208 GPa	79 GPa	0.3	7800 kg/m^3
Aluminium	79 GPa	29 GPa	0.33	2650 kg/m^3
Copper	105 GPa	39 GPa	0.34	7500 kg/m^3
Balsa Wood	3 GPa	250 MPa	0.45	170 kg/m^3
Perspex	2.5 GPa	900 MPa	0.39	1188 kg/m^3

Table 5.1: Material Properties comparison for Spar Beam

The flat plate proved to be more suitable for this type of experimental work. The figures below show the final configuration of the supporting spar for the wing. A bracket was also designed to fix the wing to the test-section of the wind tunnel.

Material Cross-section	Configuration	Frequency of First Mode [Hz]
Aluminium □	20mm x 20mm x 1.5mm length 500mm	92
Aluminium □	20mm x 20mm x 2.0mm length 500mm	90
Aluminium □	20mm x 20mm x 1.5mm length 600mm	64
Aluminium □	20mm x 20mm x 2.0mm length 600mm	62
Steel □	20mm x 20mm x 1.5mm length 500mm	87
Aluminium ⊔	20mm x 20mm x 1.5mm length 500mm	78
Aluminium ⊔	20mm x 20mm x 2.0mm length 500mm	77
Aluminium −	100mm x 5mm length 500mm	18
Aluminium −	100mm x 2mm length 500mm	7
Aluminium −	100mm x 1mm length 500mm	4*
Al-Balsa-Al ≡	1mm x 20mm x 1mm length 500mm	65
Al-Balsa-Al ≡	2mm x 20mm x 2mm length 500mm	67
Cu-Balsa-Cu ≡	1mm x 20mm x 1mm length 500mm	49
Perspex-Balsa-Perspex ≡	1mm x 20mm x 1mm length 500mm	43
Perspex-Balsa-Perspex ≡	2mm x 20mm x 2mm length 500mm	38

Table 5.2: Frequency of the first natural mode of the spar for a variety of configurations. * being the configuration chosen for the experimental work.

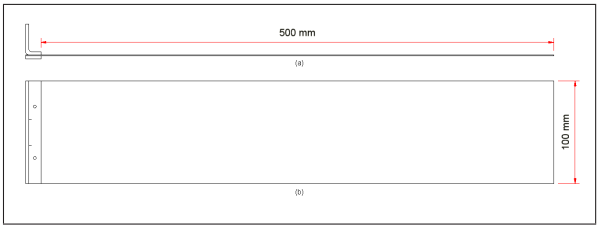

Figure 5.3: Wing Spar: (a) front view , (b) top view.

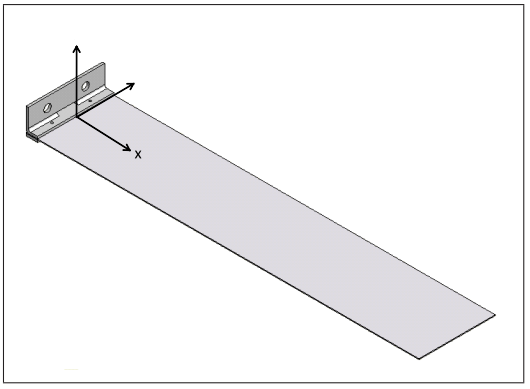

Figure 5.4: Wing Spar 3D.

5.2.2 Sensors

There are a variety of sensors that could be used to obtain the appropriate data. Some sensors would require more pre- or post-processing to convert the measured data into the relevant variables [11]. For this experimental setup we want to observe the displacement of the structure. To directly measure this parameter requires expensive video equipment. The decision was made to evaluate associated parameters and the displacements derived from the results.

Accelerometers Accelerometers where chosen as the sensor that would be able to provide details about the desired parameters. However, there are many types and sizes of accelerometers available. Once it had been decided that the plate would be the supporting structure, it became clear that several single axis accelerometers, if placed in the correct positions could gather all the relevant data. While a three-axis accelerometer might make post-processing calculations simpler, the added cost of purchasing the sensor outweighs the effort.

Since the aim is to observe deflection of the wing, information about movement in the z-direction is the most important. Single axis, out-of-plane accelerometers placed at the tip of the wing at the quarter chord and three-quarter chord positions could measure bending at the tip as well as rotation of the wing since the accelerations from the two sensors would be out of phase. Additionally, sensors are placed a third of the half-span from the tip. This will allow the sensors to capture the mode shapes, that would not be visible with only two sensors. This type of configuration can be seen in the figure below, where the accelerometers with their supporting circuitry are fixed to the plate supporting structure. The supporting circuitry is typically components that are needed to filter the output and regulate the power supply. These components are small and can easily be placed with the accelerometer on a small PCB at the desired position on the spar.

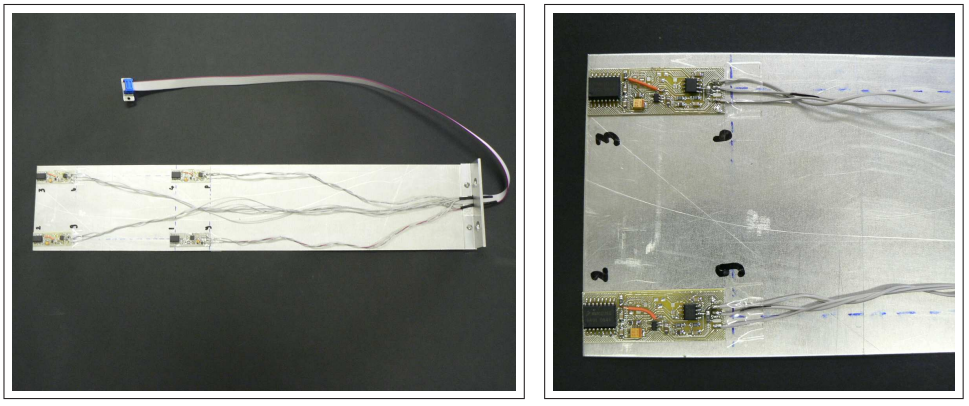

(a) Sensor Boards Attached to Wing Plate (b) Sensor Boards for Sensors 2 and 3

Figure 5.5: Sensor Boards.

Pitot-Static Tube A device used to determine total head and static pressure of a stream which can be used to calculate the stream velocity [23]. The low-speed wind tunnel has no speed control on the fans. The air velocity is controlled by hydraulic flaps which can be opened and closed at a constant rate, however,

the exact position of the flaps is not clear. The Pitot-Static Tube is used to indirectly calculate the stream velocity.

A standard configuration would have the Total Pressure Port reading $(p + \frac{1}{2}\rho V^2)$ and the Static Pressure Port reading p. The pressure difference between these two ports will then be $\frac{1}{2}\rho V^2$.

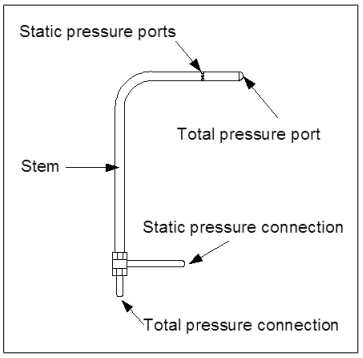

Figure 5.6: Pitot-Static Tube.

Since the wind tunnel is a low speed wind tunnel, the changes due to air velocity produce small changes in pressure. A pressure transducer transforms the pressure changes into a voltage reading which is proportional to the pressure change. The pressure transducer first needs to be calibrated by making use of a Betz Manometer.

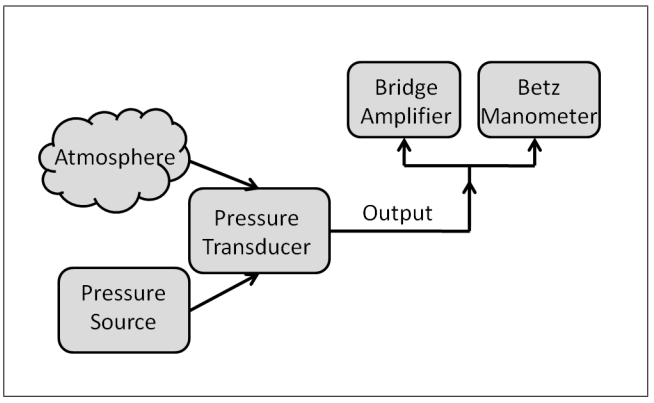

Figure 5.7: Flow diagram for air distribution during calibration of the pressure transducers.

A bridge amplifier, as can be seen in Figure 5.8, is used to give scaled readings that accurately indicate changes in pressure. The bridge amplifier needs to be set for the specific range of readings measured and the specific type of sensor that is connected to it while the pressure transducer needs to calibrated, i.e. a calibration curve for each pressure transducer needs to be created. The bridge

amplifier is set to give an output from 0-10 V at sampling frequency which is determined by the type of pressure transducer used, in this case 125Hz. Additionally, a Betz manometer is setup. The zero values of the bridge amplifier and the Betz Manometer are noted. By blowing into the pressure transducer a pressure difference is created between the high and low ports of the pressure transducer. The readings from the amplifier and the manometer are noted for five different pressures as can be seen in the Table 5.3 for two different pressure transducers. The readings from the bridge amplifier are in mV while the Betz Manometer gives readings in Pascals. The curve fitted through the data points obtained gives the calibration curve for the specific transducer. The curves can be seen in Figure 5.10.

$$P = \frac{1}{2}\rho V^2 \tag{5.1}$$

Using Equation 5.1 the already converted pressure reading can be converted into freestream velocity, with ρ the air density equal to $1.2\,\mathrm{kg/m^3}$. Conditions at the wind tunnel were assumed to be standard, i.e. 20℃ and 101.325 kPa. Unfortunately, due to limitations of the data logger, the pressure readings could not be logged but were noted every thirty seconds during an experimental run and changes to the system were made to coincide with notation of the velocity readings.

Figure 5.8: Bridge Amplifier.

(a) Pressure Transducer. (b) Betz Manometer.

Figure 5.9: Supporting Data Capture Equipment.

(a) Pressure Transducer 1

Amplifier (mV)	**Betz (x10 Pa)**
-2	-2
930	83.4
2280	210
3670	341
4790	444

(b) Pressure Transducer 2

Amplifier (mV)	**Betz (x10 Pa)**
0	-2
1538	144
2330	220.4
3200	304.4
4350	415

Table 5.3: Data Points for Calibration Curves of pressure transducers.

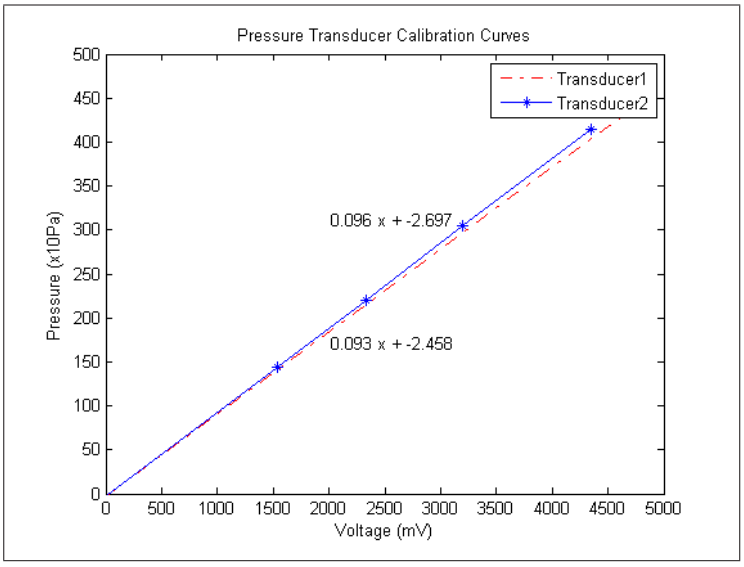

Figure 5.10: Calibration Curves.

5.2.3 Airfoil

The Clark-Y airfoil was chosen for its simple profile that is easy to manufacture with the bottom surface defined with a straight line after the 30% chord position [6]. It is also an airfoil that has been repeatedly used in experimental work and there is a lot of characterisation and documentation on this airfoil.

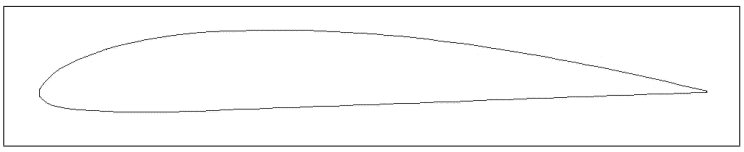

Figure 5.11: Profile of the Clark-Y airfoil.

The experimental model airfoil profile is made from a rectangular block of Polystyrene and was cut with a CNC wire cutter by a George based company, *PolyProducts*. Figure 5.12 shows a sample of the profile. The outer surface was created in one action and the inner slot was created in a second action. The slot runs the length of the experimental model and is thick enough to slide the support plate and sensor boards inside the profile without damage to either the sensor boards or the Polystyrene profile.

A higher density foam would have given a better surface finish, however, the added heat needed to cut the profile would deform such a small shape, especially at the trailing edge. Limitations imposed by the wind-tunnel test section also influenced the profile size. All these limitations affected the manner in which the profile could be

cut. Initial drawings had a separate top and bottom component but this was modified to a single component when it was clear the leading and trailing edge accuracy were compromised. The airfoil was also made larger than the chord defined by the supporting structure so that the inner slot, needed for the supporting structure, would not adversely affect the leading and trailing edge. Once the support plate and sensors are inside the profile, the split in the profile at the leading edge is filled with off-cut Polystyrene. The whole profile is then covered with Solar-Film as seen in Figure 5.13. Solar-Film is a heat sensitive material used in the activity of building model aeroplanes. The film is ironed onto the profile and shrinks slightly. This keeps it fixed to the support plate and seals the slit while provided a clean smooth surface.

Figure 5.12: Sample Styrofoam Profile.

Figure 5.13: Solar Film Covering Full Wing Profile.

5.3 Wind-Tunnel Facilities

The large wind-tunnel at the Department of Mechanical and Mechatronic Engineering is an Open-Circuit wind tunnel. An open-circuit wind-tunnel draws fresh air when in use, unlike closed-circuit wind tunnels which circulate the air already in the system. The characteristics of an open-circuit wind tunnel need to be taken into consideration when performing experimental analysis. The list below indicates some of the more influential characteristics of this type of wind tunnel.

- Since the wind-tunnel is open to the environment it is subject to gusts which cause changes in dynamic pressure across the section. These disturbances are reduced by making use of honey comb grids and flow control screens to help straighten flow.

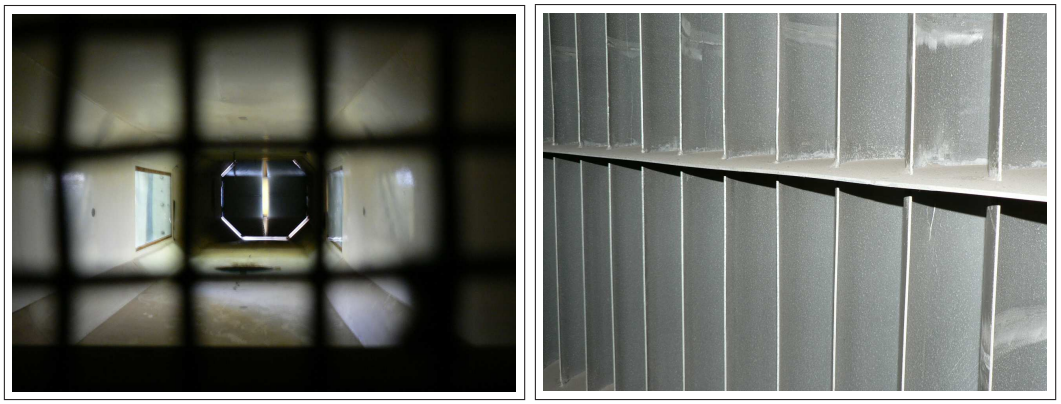

(a) Honey Comb Grid (b) Inlet Guide Vanes

Figure 5.14: Flow Straightening Devices implemented on the Low Speed Wind Tunnel.

- The noise levels are very high since the fan motor is open to the environment. This is dangerous for the people executing the experiment and some scientists feel that the noise levels could interfere with the flow pattern and cause turbulence. However, in low-speed wind-tunnels, like the one used in this experiment, this effect can be considered negligible. Health and Safety procedures also need to be followed with regard to the noise levels and appropriate safety gear, i.e. ear plugs.

- Environmental disturbances like rain, temperature and humidity will have an effect on the results. These external parameters need to be noted and no result set is complete unless it has a complete description of the environment during testing.

- The test section is below ambient pressure which is a function of the tunnel speed and the fact that the fans are downstream of the test section. This must be taken into consideration when taking pressure measurements to calculate air velocity and when performing post-run calculations.
- The fan of the wind tunnel is situated behind the test section and model failure could damage the fan. This implies a thorough analysis of the model before it is allowed into the wind tunnel and the scope of the experiment needs to be determined, i.e. the range of air speeds at which the model is "stable".

5.3.1 The Test Section

The test section is 1.2 m wide and 1.0 m high. The wind tunnel is able to reach speeds of 100 m/s. Below are pictures indicating the key aspects of the wind tunnel.

Figure 5.15: Wind Tunnel Test Section.

There are two test-sections that are available for use at the Department Mechanical and Mechatronic Engineering. This meant that while other students were busy running experiments, the setup for this experimental work could be done without interfering with their work. The test-section that was used can allow changes in angle of attack which will expand the scope of the experimental work. The test-section makes use of circular base plates made from wood and tailored to the specific model being tested. For this experiment the base would need to attach to the spar, which ever configuration is chosen, as well as the airfoil profile. This configuration can be assumed to create a cantilever type fixed-end structure. Provision will also need to be made for the supporting circuitry from the sensors to leave the model and connect

to the data capture unit. It would also be this base plate that would connect to the mechanism used for changes in angle of attack. The mechanism can be seen in the figure below.

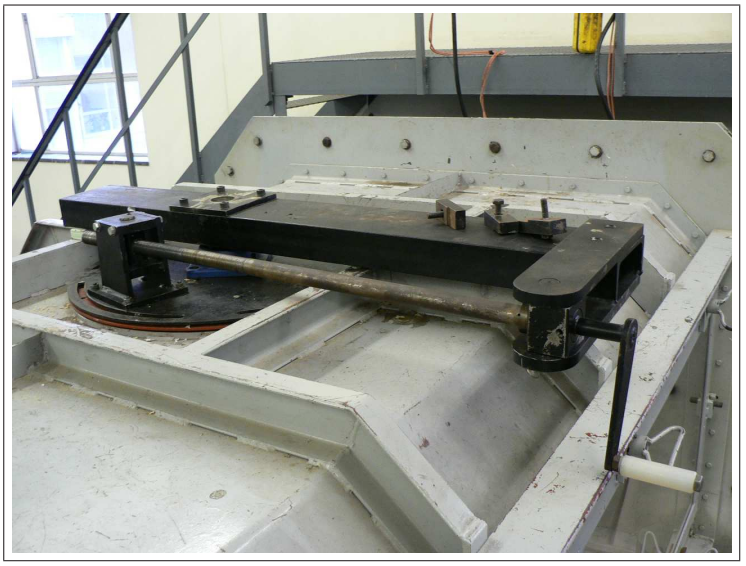

Figure 5.16: Mechanism to change angle of attack.

5.4 Supporting Equipment and Calibration

5.4.1 Data Logger and Computer

The data logger must be able to sample fast enough to pick up the highest frequency occuring in the model and picked up by the sensor.. Let us say the maximum frequency the sensor will see is, f_{max}, is 10 kHz. Then the sampling frequency needs to be at least twice that speed, preferably faster, $f_s > 2f_{max}$. Let us then define the voltage range over which the device will operate as E_{FSR} and the rate of data capture as M. The resolution of the device is then defined as

$$Q = \frac{E_{FSR}}{2^M} \tag{5.2}$$

The resolution of the device is the smallest voltage increment that will cause a bit change [35].

While the data logger converts the analog signal into a digital one, the data still needs to be recorded for analysis at a later stage. Most data loggers come with software that enables easy transfer of the experimental data into a usable format. For this we need a computer to run the software and store the results. The main

criteria for the computer is that it has the correct connection ports and runs the data logger software.

5.4.2 Sensor Parameter Quantization

With the sensor boards built and checked for errors, the bias of the sensor needs to be accurately quantified. This is done in conjunction with determining the gain on the sensor board. At this stage the sensor boards are attached to the wing so the gains and bias can be determined for all four sensors at the same time. The gains are affected by the tolerances on the components used in the amplification circuitry, while the bias of each sensor is defined as sitting at 2.5 V. Since the sensors are out of plane, a 1 g reading should be logged when the wing is lying flat on the table. The data at this position is logged for a reasonable length of time so that a steady state reading is obtained. The wing is then turned over so that a negative 1 g is being logged. The figure below shows the acceleration readings from the four sensors. It is clear that the bias of the sensors are all different.

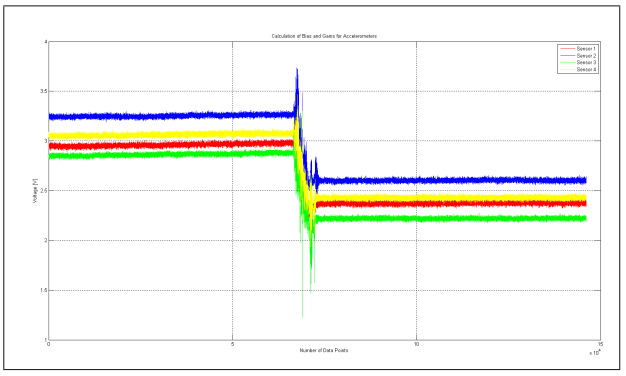

Figure 5.17: Acceleration readings used for the calculation of the bias and gains for each sensor.

Sensor	Bias [mV]	Gain
1	2.6663	7.3049
2	2.9268	8.0903
3	2.5407	8.0185
4	2.7453	7.9200

Table 5.4: Bias and Gains of the Accelerometer sensors based on the results of Figure 5.17.

Let us look at the procedure followed for calculating the bias and gain for sensor 1, i.e. the red graph. The mean for the first forty percent of the data points and the mean for the last forty percent of the data points is taken. We know that the acceleration range between these two means is 2 g. The two means are therefore

added and divided by two. This gives us the bias of the sensors which should be near 2.5 V. The difference between the bias and the reading for either the positive or negative g of acceleration is then compared with the rating of the acceleration sensor. The data sheet for the 1213EG accelerometer from *Freescale* measures 40 mV/g. The ratio of the voltage read to the rated voltage is the gain of the sensor. Table 5.4 shows the bias and gains for the four sensors used during the experimental work.

5.5 Post-Processing of Experimental Data

The procedures followed during the experimental data capture can be seen in Appendix B

5.5.1 Uncertainty Analysis

The main sources of error that occur during experimental work are

- calibration errors,
- data-acquisition errors and
- data-reduction errors

Each of these error sources need to be evaluated and minimised to ensure accurate results that are relevant to the experiment. The calibration errors are associated with the instruments used to obtain the data. Examples of some common elements of instrument error are:

Hysteresis error The difference between an upscale sequential test and a downscale sequential test.

Linearity error The difference between a linear curve fit and a calibration data set.

Sensitivity error A statistical measure of the random error in the estimate of the slope of the calibration curve. The static sensitivity of a device is also temperature dependent.

Zero-shift error The vertical shift of the calibration curve due to a drift in the zero intercept while at a constant sensitivity.

Repeatability error The ability of the system to indicate the same value upon repeated but independent application of the same input.

The overall instrument error is the combination of all known errors and will give the uncertainty of the device.

$$U_c = \sqrt{e_1^2 + e_2^2 + ... + e_n^2} \tag{5.3}$$

5.5.2 Quantization Effects

The data logger ($\mu DAQlite$ from $EagleTechnologies$) has two ways of capturing data from the input analog channels. The options are single ended or differential ended. It was noted during the calibration of the sensors that the quantization effects for these two settings are vastly different. When sampling is done in a single-ended manner, the reading is taken between the channel and the analog ground. The quantization step on this signal is 10 mV. While the differential ended method takes a reading between two channels, i.e. the difference between channel 0 and channel 1, and has a quantization step of 1 mV. The data logger has eight analog input channels, and since there are only four sensors, two of the channels were to be used to log the dynamic and atmospheric pressure. However, since the differential ended sampling needed to be used to reduce quantization errors, and the sampling is done between two channels, only four channels can be captured. This meant the pressure readings, which were used to calculate the air velocity had to be noted by hand at specific time intervals.

The need for the reduced quantization error is emphasised by the small output from the accelerometer which even though amplified is still small. Refer to Section 5.4.1

5.5.3 Filtering of Raw Data

From prior calculations and Nastran simulations of the wing-like structure it was determined that raw data with a frequency above 400 Hz was not relevant to the structural behaviour of the wing and could be considered negligible. A low pass Butterworth filter of 4th order was implemented. Figure 5.18 below shows the power spectral density of the acceleration data from sensor 1 before and after filtering. From these figures it is clear that frequencies above 400 Hz have been either reduced or removed. However, there is a large component of data near 0 Hz.

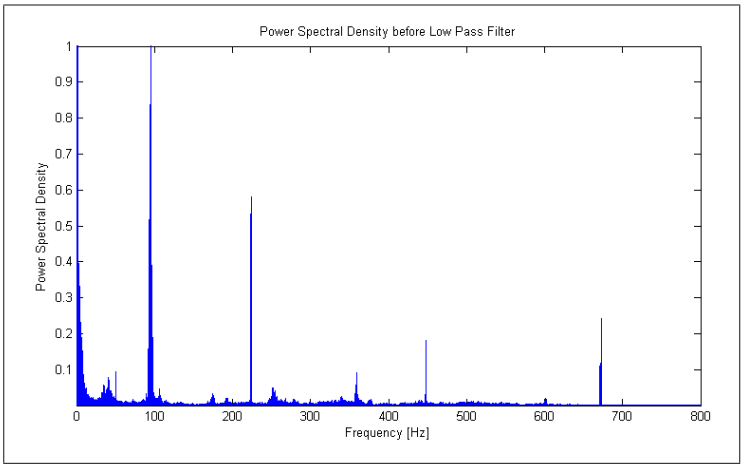

(a) Before Low Pass Filter

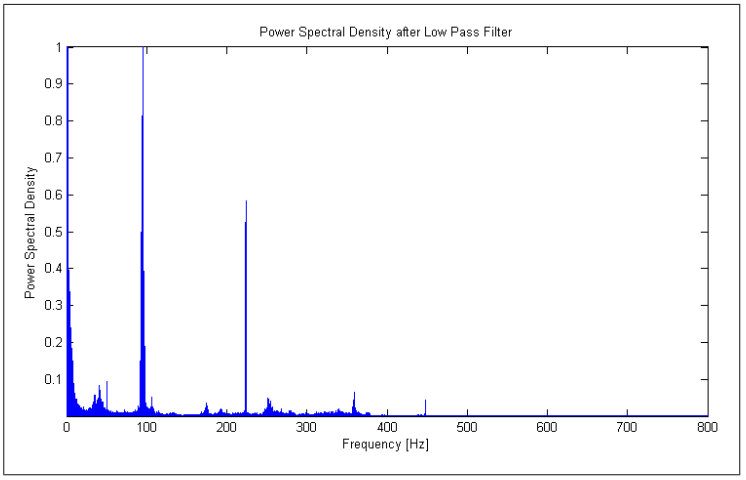

(b) After Low Pass Filter

Figure 5.18: Effect of a Low Pass Filter at 400Hz.

The component sitting at 0 Hz can be explained by the DC bias on the sensors and will be removed when the bias is removed from the raw data. However, even with the bias removed there is still slow frequency data which is unexplained. The first mode shape is identified at a frequency of 3 Hz. The data below this frequency could still be filtered, however, the source of the data obtained at the slower frequencies needs to be determined to ensure there is no loss of relevant data.

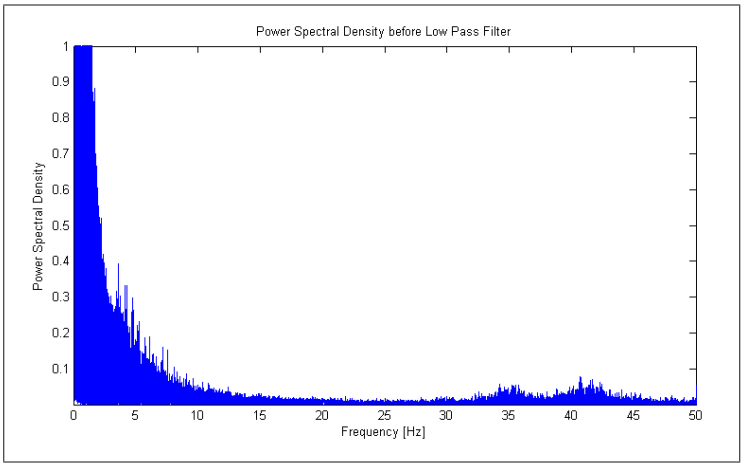

(a) Before High Pass Filter

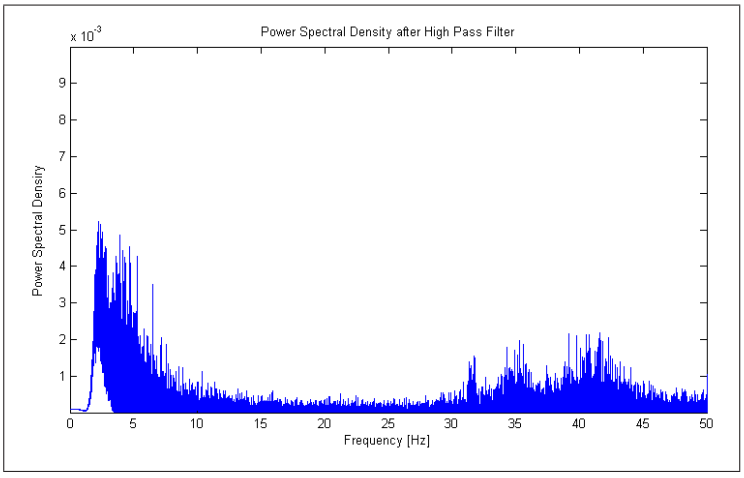

(b) After High Pass Filter

Figure 5.19: Effect of a High Pass Filter at 2Hz.

There were several possible sources. These included the Fluorescent lights, the hydraulic flaps used to control the velocity and the fan motor. The lights and the flaps were eliminated by sampling firstly with the lights on and off and then whilst moving the hydraulic flaps. Neither of these sources produced the low frequencies we were capturing during the experimental run. This left the fan motor as the only source of the disturbance. It is felt that there is coupling between the power source for the accelerometer boards and the 3-phase motors driving the fan. Lastly, a band stop filter at 50 Hz was used to remove noise generated by the sensor board power supply. The procedure followed to clean up the signal can be seen in Figure B.1 which was implemented in a Matlab script. Further details about the filters and their coefficients can be seen in Appendix B.

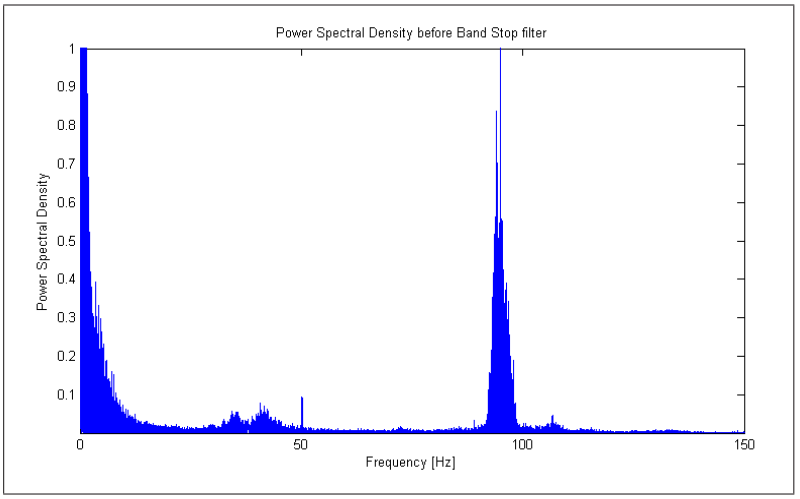

(a) Before Band Stop Filter

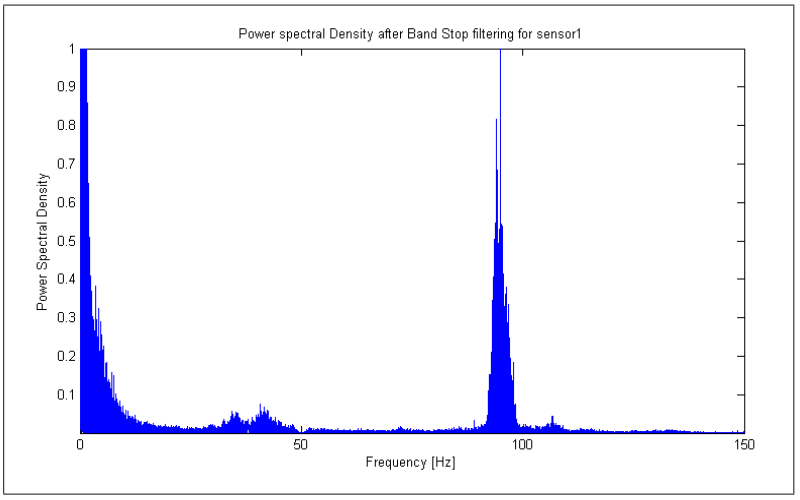

(b) After Band Stop Filter

Figure 5.20: Effect of a Band Stop Filter at 50Hz.

5.5.4 Integration of Acceleration Data

For the purposes of comparing the experimental data with the structural analysis, displacement data was needed. The accelerometer data, therefore, needed to be integrated twice to achieve these results. However, after using a simple integration function in Matlab, the results were unexpectedly biased and not representative of the behaviour witnessed during the experimental runs.

This is as a result of the double integration that was applied to the accelerometer data. Any slight drift or noise in the data captured can greatly influence firstly the velocity result, which provides incorrect data for the second integration which makes the error on the displacement results even larger. Post-processing of the accelerometer data becomes very important. The method described below through a worked

example was originally designed for the integration of analog seismic acceleration data. This process was implemented in a Matlab script.

The script was first tested with a simple sine wave to verify the algorithm before implementing it on the acceleration data. The process started by first assuming a displacement vector, differentiating twice to get an acceleration vector and then applying the proposed method to return to the original displacement vector.

$$\begin{aligned} \text{Displacement} &= \sin(10x) \\ \text{Velocity} &= \frac{\delta}{\delta x}\sin(10x) \\ \text{Acceleration} &= \frac{\delta^2}{\delta^2 x}\sin(10x) \end{aligned}$$

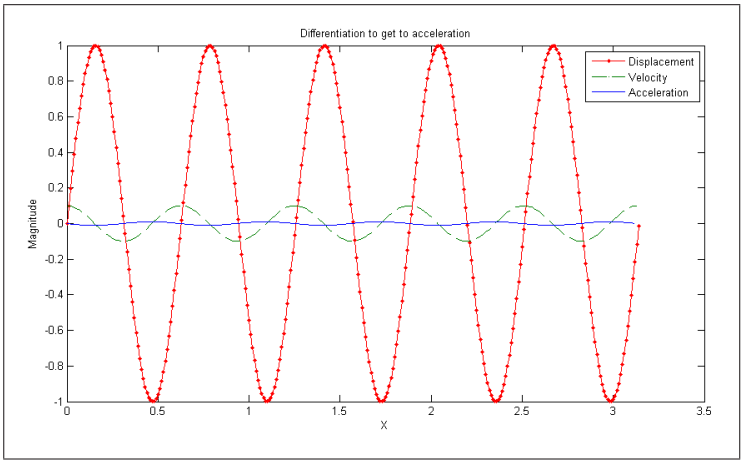

Figure 5.21: Sample data for the testing of the integration technique to be used on the filtered accelerometer data.

The first step is to determine the mean of the acceleration signal, remove this bias and shift the signal with one integration step.

Algorithm 5.1: Update Accelerometer signal with signal mean.

for $s = 1$ **to** Num_{Sensor} **do**
    $y_m(s) = mean(Acceleration(s)/Gain(s))$; /* Mean Ordinate */
    $tent_{Acc}(s) = Acceleration(s)/Gain(s) - y_m(s)$; /* Tentative algebraic ordinates of the acceleration */
    $y_{mshift}(s) = y_m(s) + (1/sampling_f)$; /* Mean of the acceleration plus one integration step */
    $tent_{Acc\_shift}(s) = Acceleration(s)/Gains(s) - y_{mshift}(s)$; /* new acceleration curve after the shift */
end

We then integrate the unbiased and shifted accelerometer signals to obtain an initial velocity signal.

Algorithm 5.2: Integrate Updated Acceleration Signal.

for $s = 1$ **to** Num_{Sensor} **do**
    $Vel(s) = \int tent_{Acc}(s)$
    $Vel_{shift}(s) = \int tent_{Acc\_shift}(s)$
end

Next, we create C_m and C_{mshift} which are constants for shifting the velocity signal so that its sum is near zero. This will ensure a well placed displacement result,

Algorithm 5.3: Velocity Shifting Coefficients.

for $s = 1$ **to** Num_{Sensor} **do**
    $C_m(s) = mean(Vel(s))$
    $C_{mshift}(s) = mean(Vel_{shift}(s))$
end

Now we need to integrate to get a temporary displacement signal by making use of the calculated Velocities and shifting constants.

Algorithm 5.4: Integrate Shifted Velocity.

for $s = 1$ **to** Num_{Sensor} **do**
    $Temp(s) = Vel(s) + C_m(s)$
    $Displ(s) = \int Temp(s)$
    $Temp_{shift}(s) = Vel_{shift}(s) + C_{mshift}(s)$
    $Displ_{shift}(s) = \int Temp_{shift}(s)$;
end

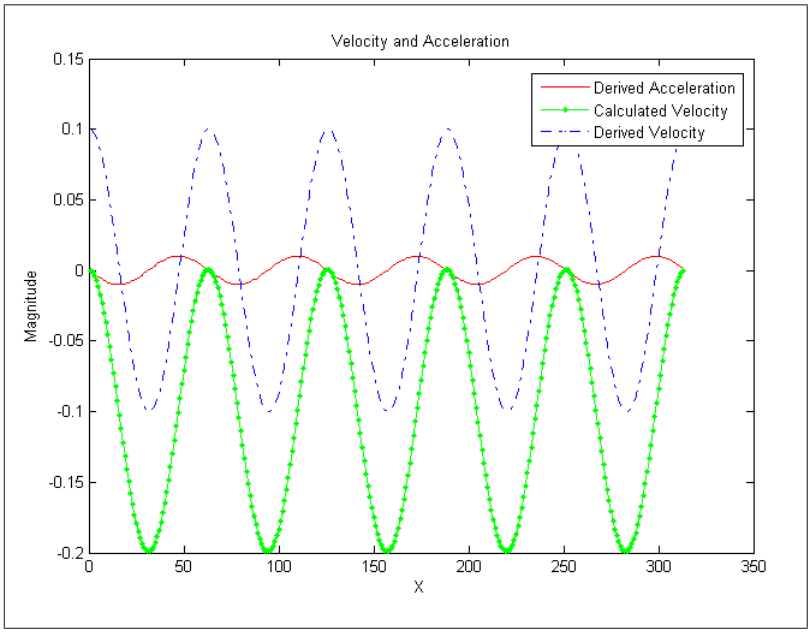

Figure 5.22: Comparison between the original derived velocity and the integrated velocity from the acceleration data.

From Figure 5.22 we can clearly see the Velocity signal matches the originally derived velocity signal but is still shifted so that the start and end of the signal co-incide with the accelerometer signal. The next step is to fit a parabola through the displacement data and tilt it to define the new central axis. This tilt produces another coefficient that applies to the acceleration and velocity signals.

Algorithm 5.5: Inclusion of all Shifting Coefficients in Integration of Accelerometer Data.

```
for y = 1 to Num_Sensor do
    for ss = 1 to size(Displ(y)) do
        pp(ss, y) = Coeff(y, 3)ss^2 + textCoeff(y, 2)ss + Coeff(y, 1)
        pp_Shift(ss, y) = Coeff_Shift(y, 3)ss^2 + Coeff_Shift(y, 2)ss + Coeff_Shift(y, 1)
    end
    Displacement(y) = Displ(y) − pp(y)
    Displacement_Shift(y) = Displ_shift(y) − pp_Shift(y)
    y_p(y) = mean(pp(y)/pp_Shift(y))
    for ss = 1to size(Displ(y)) do
        C_p(ss, y) = y_p(y)(ss + 1)/2
    end
end
for s = 1 to Num_Sensor do
    step = (1/sampling_f)
    axis = pp(size(Displ), s)/step
end
if pp(s) < pp_Shift(s) then
    C_e(s) = −axis/size(Displ);          /* Correction must be negative */
else
    C_e(s) = axis/size(Displ);           /* Correction must be positive */
end
for s = 1 to Num_Sensor do
    Acceleration_Gradient(s) = y_m(s) + y_p(s);
end
for y = 1to Num_Sensor do
    for ss = 1 to size(Vel(y)) do
        Vel_Grad(ss, y) = C_m(y) + C_p(ss, y) + C_e(y)
    end
end
```

Algorithm 5.6: Last step in integration of accelerometer experimental data.

for $y = 1$ **to** Num_{Sensor} **do**
  $Temp(y) = Acceleration(y)/Gain(y)$
  $Q(y) = \int Temp(y)$
  $mQ(y) = mean(Q(y))$
  for $s = 1$ **to** *size(Acceleration)* **do**
    $meanQ(s, y) = Q(s, y) + Vel_{Grad}(s, y) - mQ(y)$
  end
  $P(y) = \int Q(y)$
  $\Delta X = Acceleration(1)$
  $\Delta Y = abs(P(1, y) - P(Acceleration(1), y))$
  for $s = 1$ **to** *size(Acceleration,y)* **do**
    $meanP(s, y) = P(s, y) + (-\Delta Y/\Delta X(-s) - P(Acceleratiom(y), y))$
  end
  mP(y) = mean(P(y))
  for $s = 1$ **to** *size(Acceleration,s)* **do**
    $meanP(s, y) = P(s, y)+(-\Delta Y/\Delta X(size(Acceleration)-s)-P(tf(1), y))$
    $mP(y) = mean(P(y))$
  end
end

Now that we have all the shifting coefficients, we can integrate the accelerometer data without producing unwanted bias effects. Further discussion of the experimental results can be found in Chapter 6.

Chapter 6

Verification of Program

6.1 Introduction

There were various stages during the completion of the code that needed to be verified before moving on to further development. Firstly, the static structural component of the code was verified by means of commercial software. The natural frequencies of the wing-structure are compared with the PSD of the experimental accelerometer data to verify the validity of the experimental data. The aerodynamic component of the code is verified against the characterization with AVL. The displacement data is then compared with the structural component and characterization of the airfoil.

6.2 Static Structural Verification

Once the structural algorithm had been completed, results were verified by making use of MSC.Nastran (available to the University under a student licence) to create the same model and apply the same loads. Initially the structural algorithm implemented an 8-noded element but it was quickly discovered that this type of element could not accurately portray the quadratic behaviour of the deflections, even when the mesh was highly refined. A 20-noded element was then used and for the same refinement of mesh, the structural algorithm and the MSC.Nastran results correlated as can be seen in Table 6.2 and Figures 6.1 to 6.8. The wing was constrained in all six degrees of freedom at the one end and a vertical load was applied to the free end. The table below further describes the four configurations.

Setup	Span [m]	Thickness [m]	Chord [m] Root	Chord [m] Tip	Num Elm X	Num Elm Y	Point Load [N]	Percentage Chord
1 - Straight	0.865	0.01	0.3	0.3	20	2	10.5	50
3 - Tapered	0.865	0.01	0.3	0.1	50	2	10.5	50
5 - Straight	0.865	0.01	0.3	0.3	50	2	10.5	25
7 - Tapered	0.865	0.01	0.3	0.15	50	2	10.5	25

Table 6.1: Verification Setups.

The choice of the four setups used for verification were designed to test several aspects of the structural algorithm. The first setup was kept as simple as possible so that a hand calculation could verify its results. To this end, the load was applied at the centre of the free end of the beam. The third setup had a varying cross-section, which tapered towards the free end. This setup was used to verify that the element definitions were correct and that the global stiffness matrix was correctly assembled. The fifth and seventh setups were created to see the twisting effect of a load that was not applied to the centre of the beam, as one would see with a lifting load applied to the quarter chord position.

Model		Displacement X $\times 10^{-06}$	Y$\times 10^{-07}$	Z$\times 10^{-04}$	Resultant $\times 10^{-04}$
Setup 01	Nastran	3.687	2.286	4.171	4.171
	Code	3.687	2.286	4.171	4.171
Setup 03	Nastran	4.611	2.585	4.941	4.942
	Code	4.568	2.843	4.915	4.915
Setup 05	Nastran	3.787	4.569	4.325	4.325
	Code	3.750	4.355	4.305	4.305
Setup 07	Nastran	4.595	3.140	4.958	4.958
	Code	4.581	4.454	4.977	4.977

Table 6.2: Results summary for the maximum wing tip displacement of four test setups for the validation of the structural algorithm.

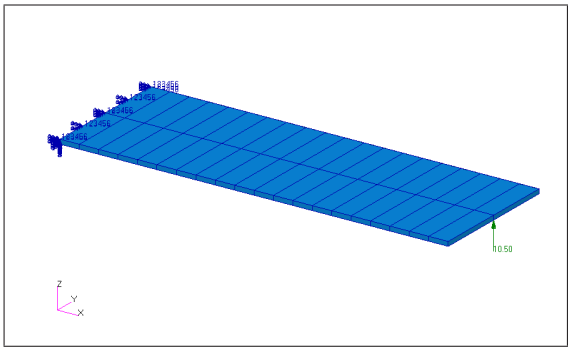

Figure 6.1: Setup 1 boundary conditions and loading.

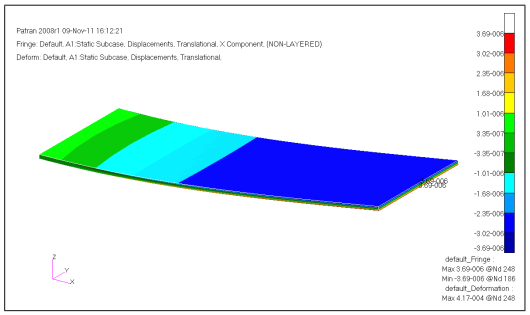

(a) Nastran X-displacment.

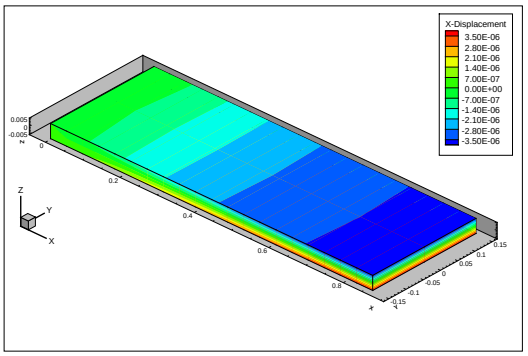

(b) Code X-displacement.

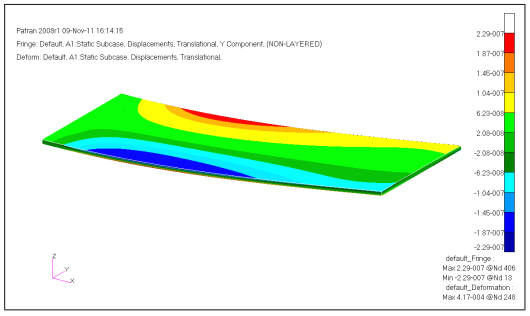

(c) Nastran Y-displacement.

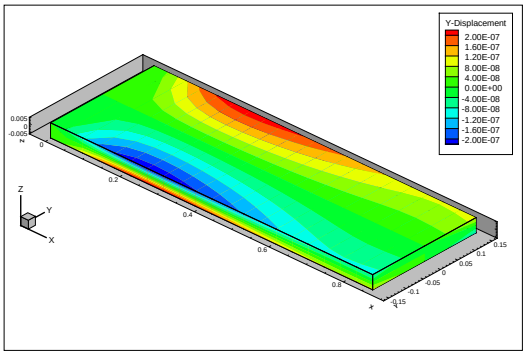

(d) Code Y-displacement.

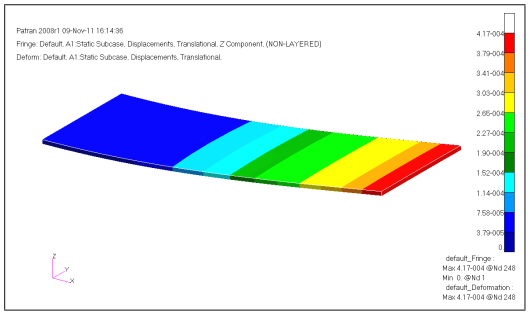

(e) Nastran Z-displacement.

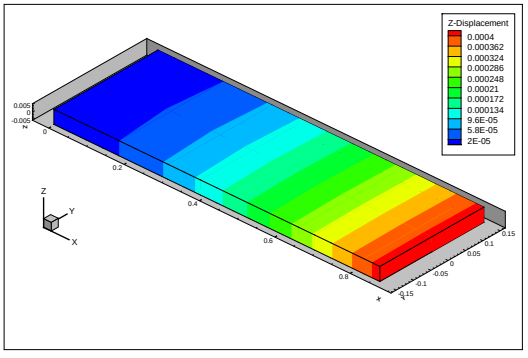

(f) Code Z-displacement.

Figure 6.2: Setup 1 Displacement Results.

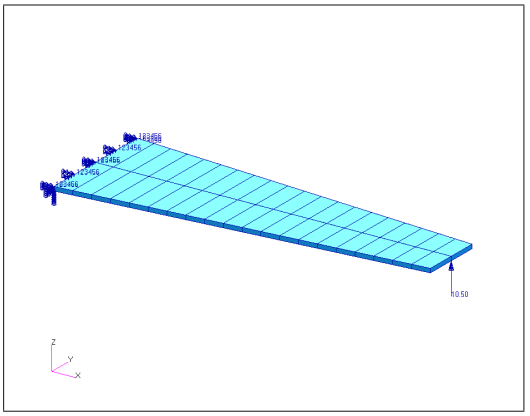

Figure 6.3: Setup 3 boundary conditions and loading.

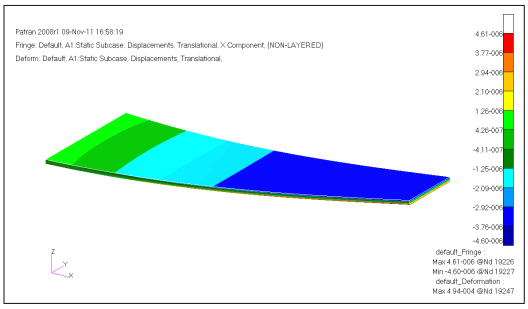

(a) Nastran X-displacement.

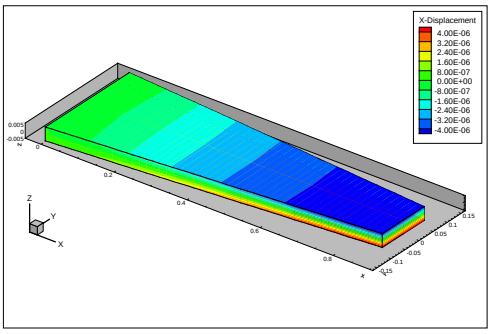

(b) Code X-displacement.

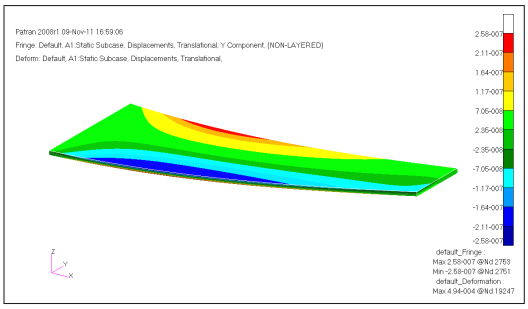

(c) Nastran Y-displacement.

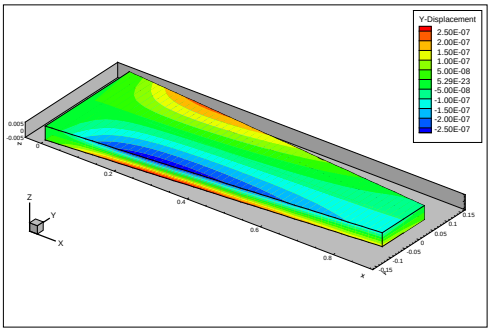

(d) Code Y-displacement.

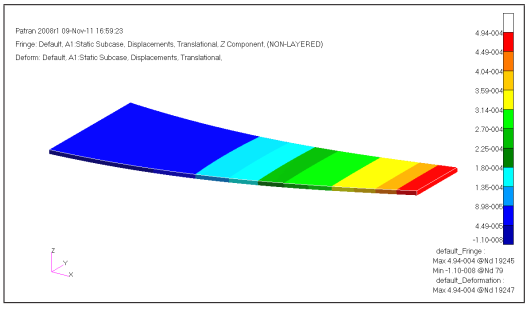

(e) Nastran Z-displacement.

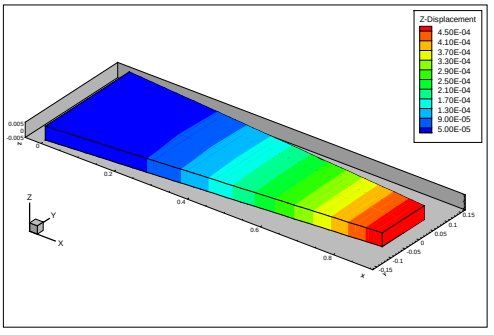

(f) Code Z-displacement.

Figure 6.4: Setup 3 Displacement Results.

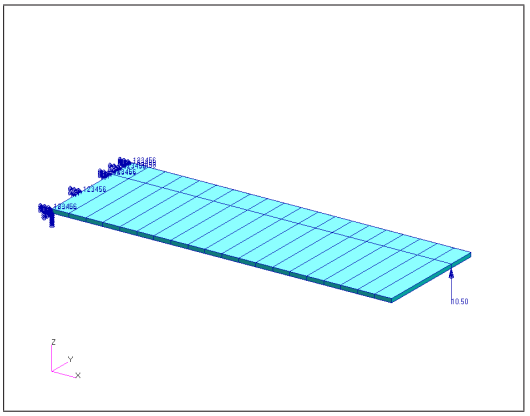

Figure 6.5: Setup 5 boundary conditions and loading.

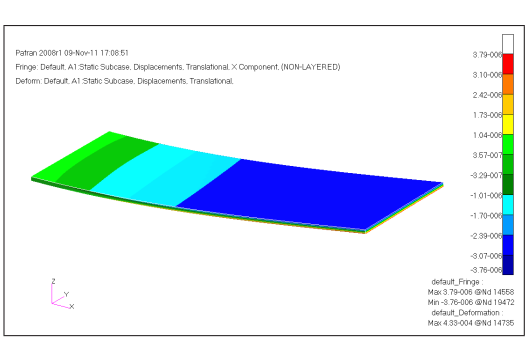

(a) Nastran X-displacement.

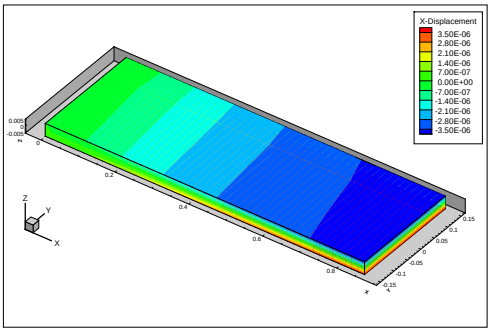

(b) Code X-displacement.

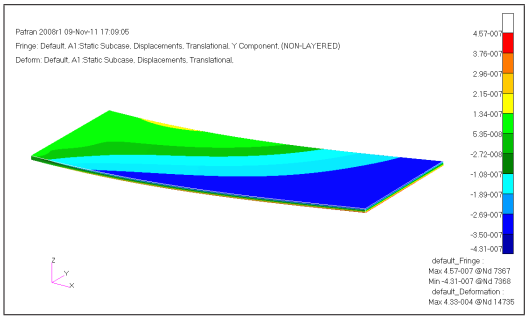

(c) Nastran Y-displacement.

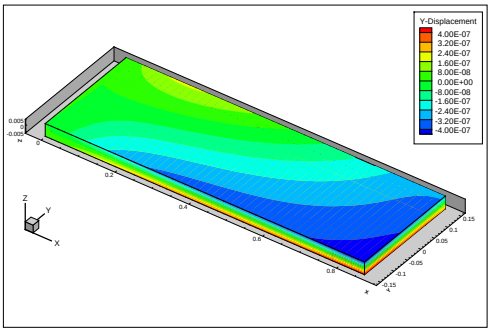

(d) Code Y-displacement.

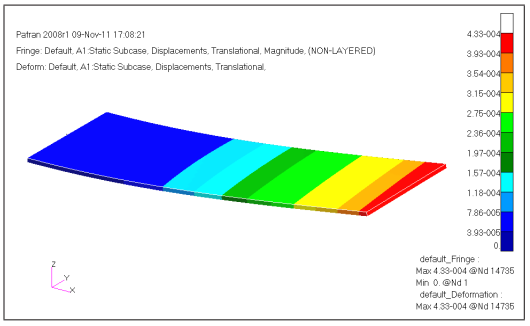

(e) Nastran Z-displacement.

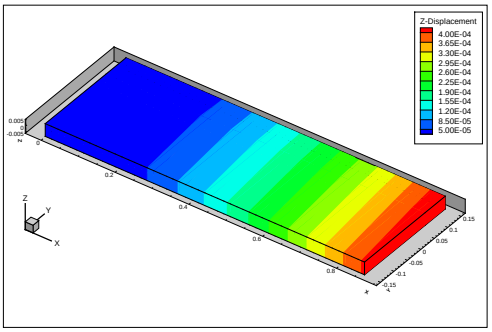

(f) Code Z-displacement.

Figure 6.6: Setup 5 Displacement Results.

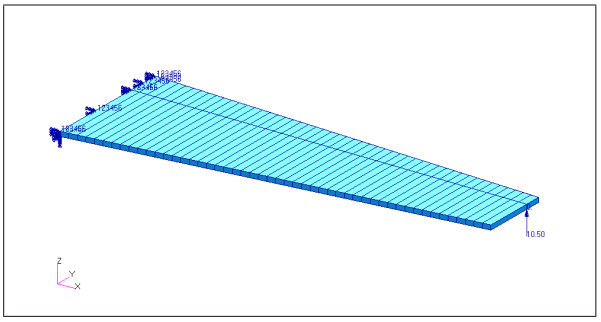

Figure 6.7: Setup 7 boundary conditions and loading.

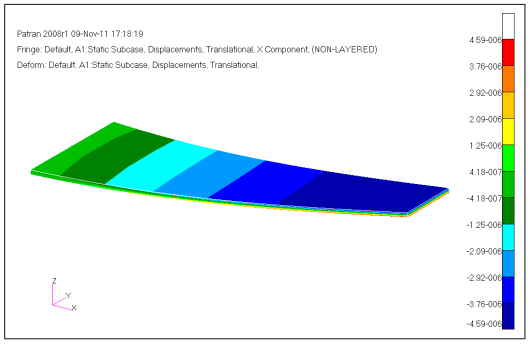

(a) Nastran X-displacement.

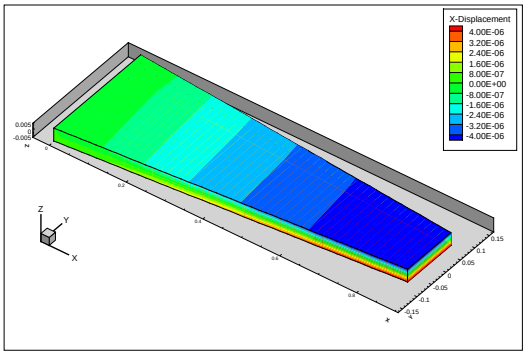

(b) Code X-displacement.

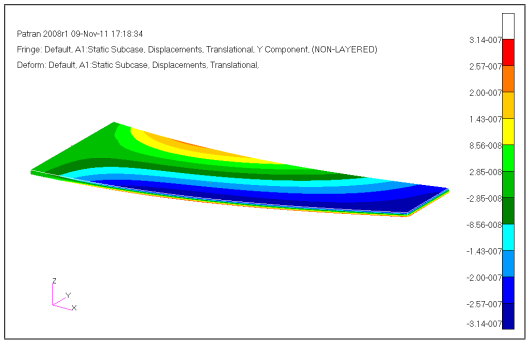

(c) Nastran Y-displacement.

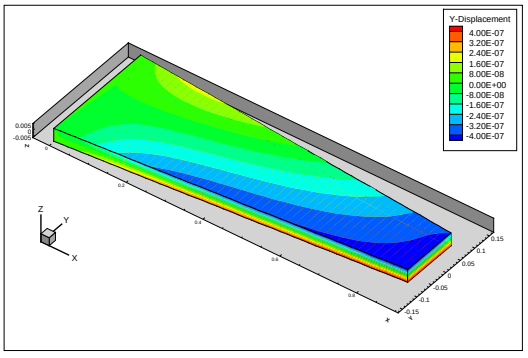

(d) Code Y-displacement.

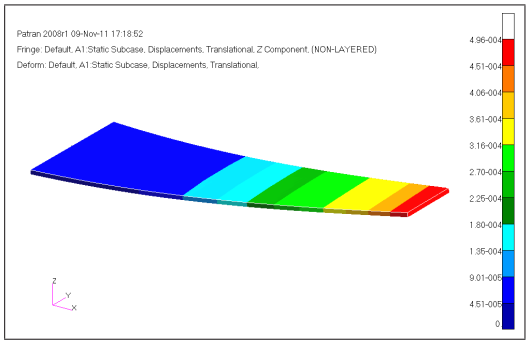

(e) Nastran Z-displacement.

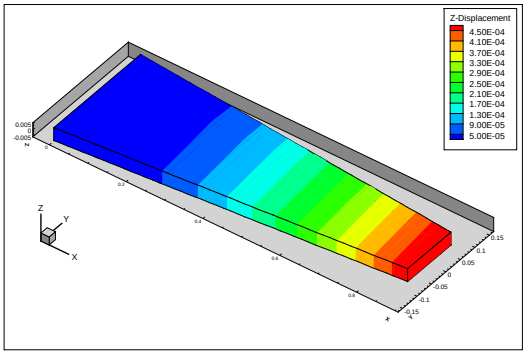

(f) Code Z-displacement.

Figure 6.8: Setup 7 Displacement Results.

6.3 Natural Frequency Comparison

After the experimental data was obtained, the raw data was reduced to relevant material (discussed in Chapter 5). The first stage of verification is to establish if the acceleration data is valid and that it is comparable to the simplified model that we are using for simulation.

A natural modes analysis shows the typical behaviour of a structure when excited at a resonant frequency, while a power spectral density plot of the acceleration data will be able to indicate which frequencies react with more intensity. This would coincide with a natural frequency that was excited.

An important consideration when determining the accelerometer positioning was the mode shapes of the wing-like structure. This is due to the fact that an accelerometer sitting on a position where there is zero deflection for a specific mode shape would not indicate that frequency as a natural mode. Figure 6.9 shows the modes shapes for the first two modes of a beam like structure.

If we recall from Chapter 5, two accelerometers (sensor 2 and 3) are placed at the free end of the beam and two accelerometers were placed a third of the beam length from the free end (sensors 1 and 4). Comparing these locations with the first mode shape we can see that all four accelerometers should pick up the first mode frequency, with the sensors at the free end having a larger magnitude than the others.

Looking at the second mode shape, the two accelerometers sitting at a third of the beam length coincide with the point of zero deflection of the mode shape. Therefore, this frequency should not be excited in a power spectral density plot for these two sensors but should still be noticed on the free end sensors.

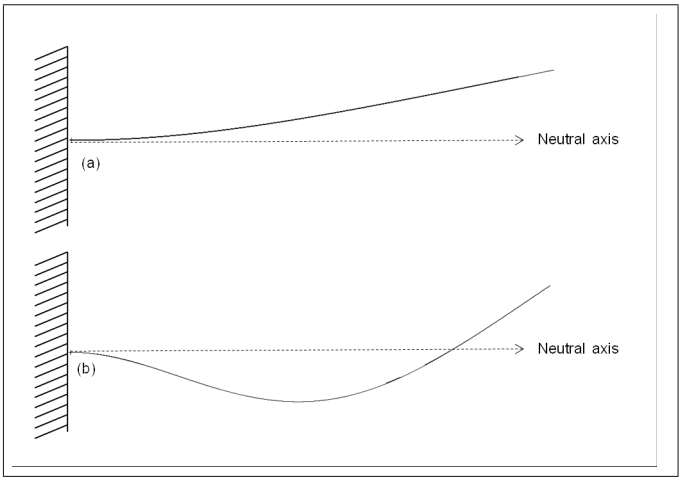

Figure 6.9: Natural Mode Shapes for a Cantilever Beam Structure.

Figures 6.10, 6.11 and 6.12 show the first three natural frequencies and mode shapes for the experimental model. The first ten natural frequencies are listed in Table 6.3.

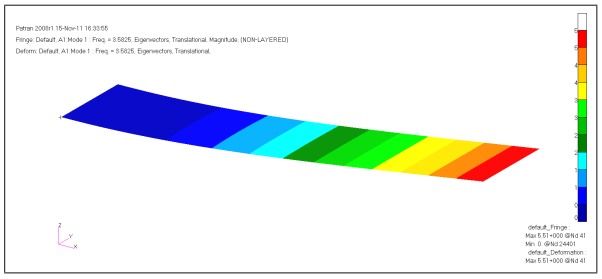

(a) ISO View.

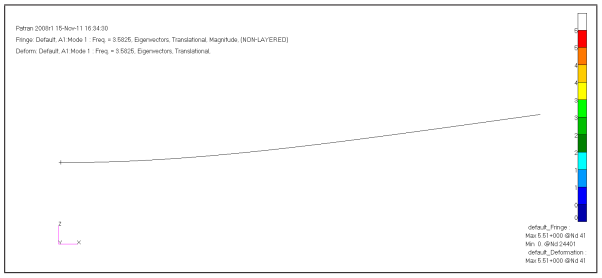

(b) Side View.

Figure 6.10: First mode shape of the experimental wing structure - 3.5825Hz - Bending.

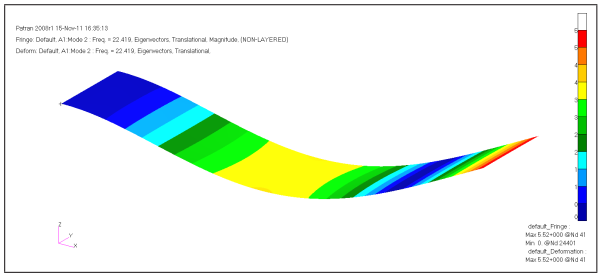

(a) ISO View.

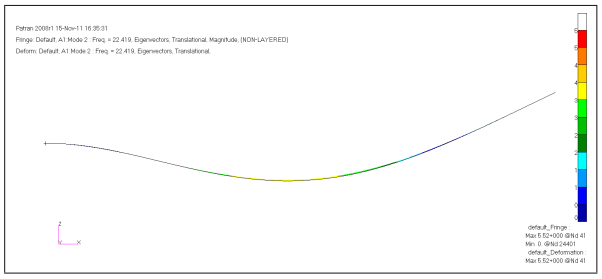

(b) Side View.

Figure 6.11: Second mode shape of the experimental wing structure - 22.419Hz - Bending.

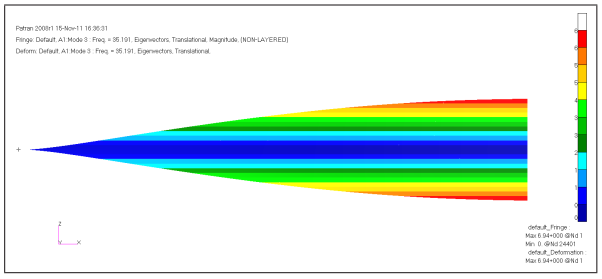

(a) Side View.

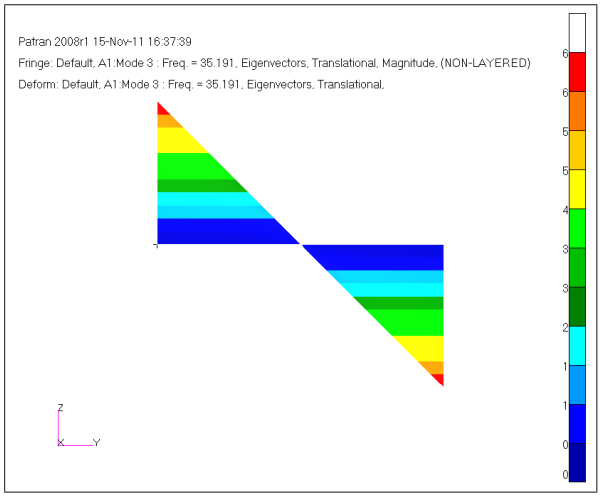

(b) Front View.

Figure 6.12: Third mode shape of the experimental wing structure - 35.191Hz - Twisting.

Mode	Frequency [Hz]
1	3.58
2	22.42
3	35.19
4	62.9
5	107.7
6	123.8
7	186.5
8	205.46
9	275.02
10	307.9

Table 6.3: The first ten natural frequencies of the experimental model, obtained through analysis with MSC.Nastran.

Figure 6.13 to 6.17 show the PSD plots for all of the sensors for all the test cases. Let us look at the results for the test case at 0° AOA (Figure 6.13). It is clear that all

four sensors pick up the first natural mode of the structure, around 3 Hz. However, the high pass filter has slightly distorted the data around the $2 - 3$ Hz region so the absolute magnitude of the intensity of the peak should not be considered, only the fact that it is present.

The second natural frequency occurs around 22 Hz. However, none of the PSD plots seem to indicate an elevated intensity in this area. This could be due to the type of loading on the wing structure. Static loading of the wing produces a shape similar to that of the first mode. Therefore, only a small amount of additional energy at the first mode frequency is needed to induce the first mode shape. However, the second mode shape does not match the statically deformed shape, therefore, a lot of energy at the second mode frequency is needed to produce the second mode shape.

However, mode three at 35 Hz, which is a twisting mode is definitely present. The natural frequencies determined through the experimental results will vary slightly from the simulation results since there is added mass from the sensor boards and the airfoil profile. Additionally, the experimental wing is slightly longer due to its mounting bracket. This will cause the peak that coincides with a mode shape to shift either slightly higher or lower depending on the discrepancy with the simulation model.

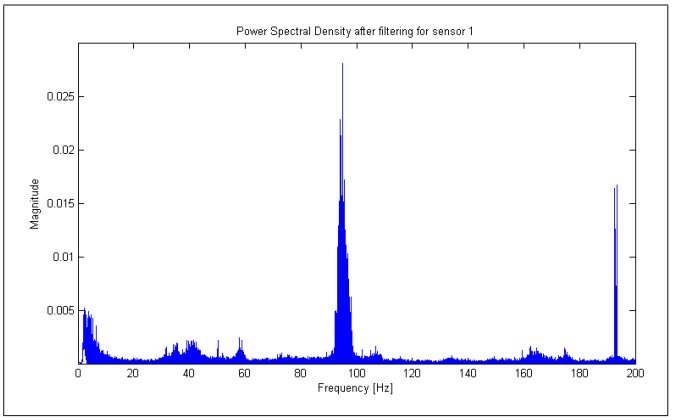

(a) Sensor 1

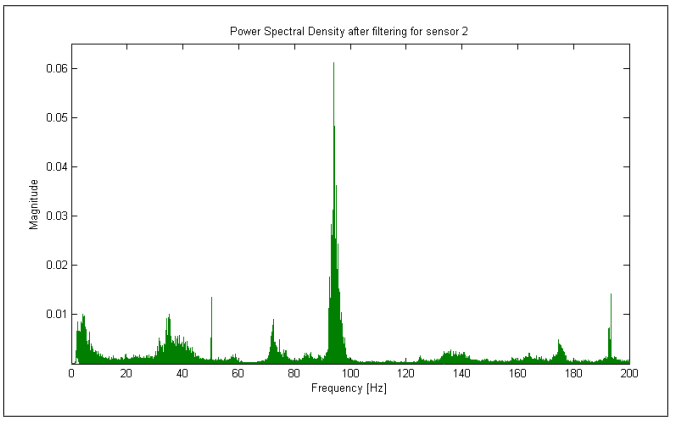

(b) Sensor 2

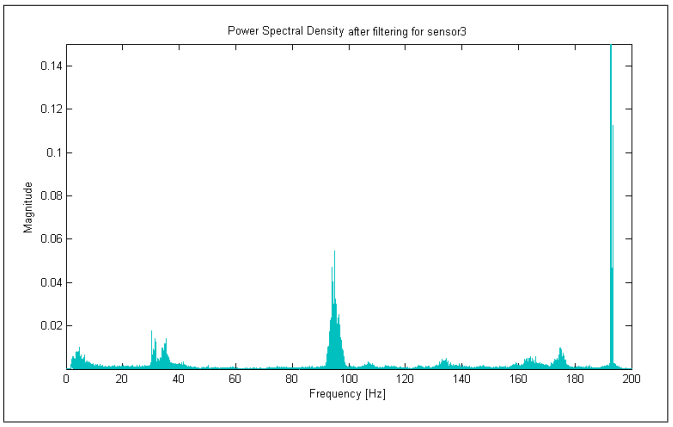

(c) Sensor 3

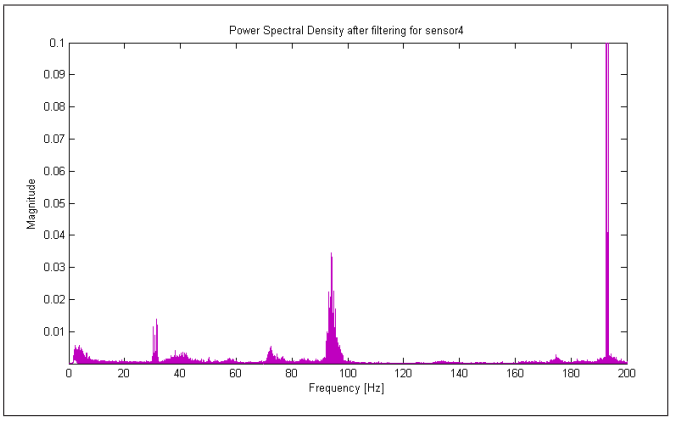

(d) Sensor 4

Figure 6.13: Power Spectral Density for 0° angle of attack.

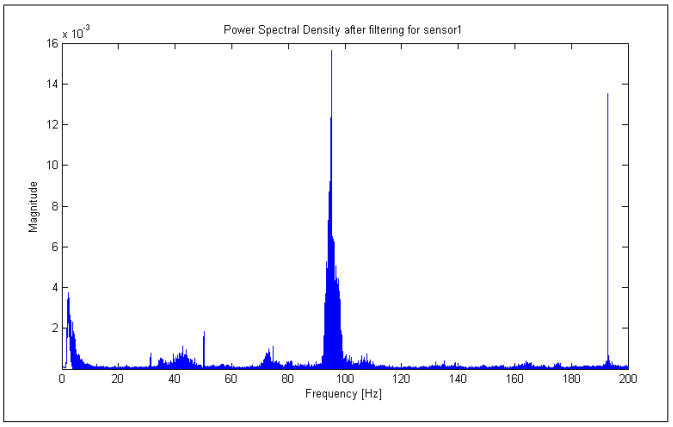

(a) Sensor 1

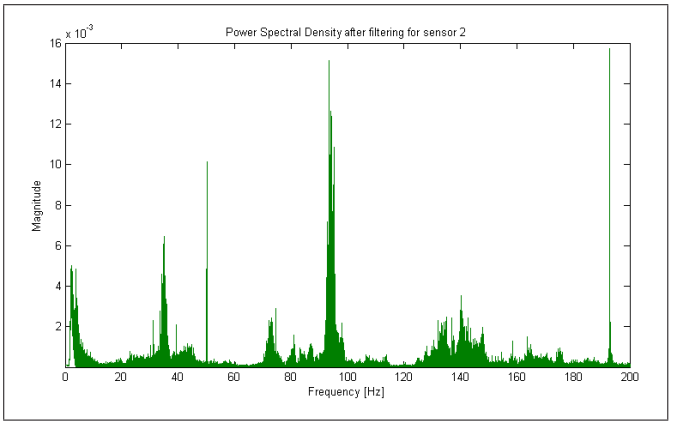

(b) Sensor 2

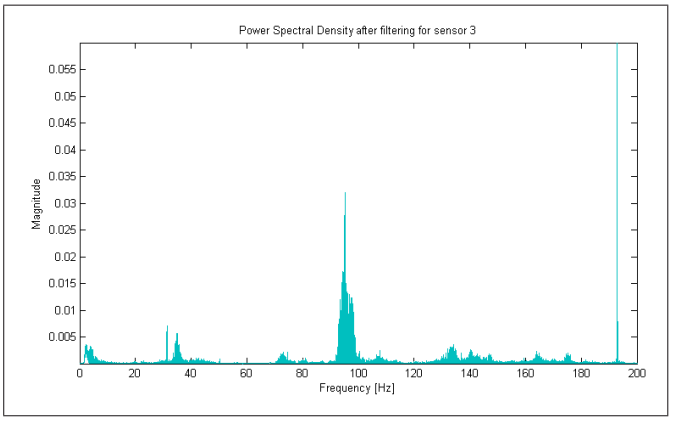

(c) Sensor 3

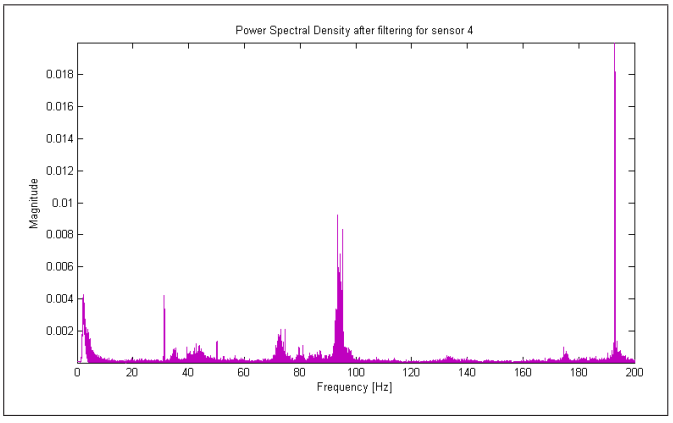

(d) Sensor 4

Figure 6.14: Power Spectral Density for $-5°$ angle of attack.

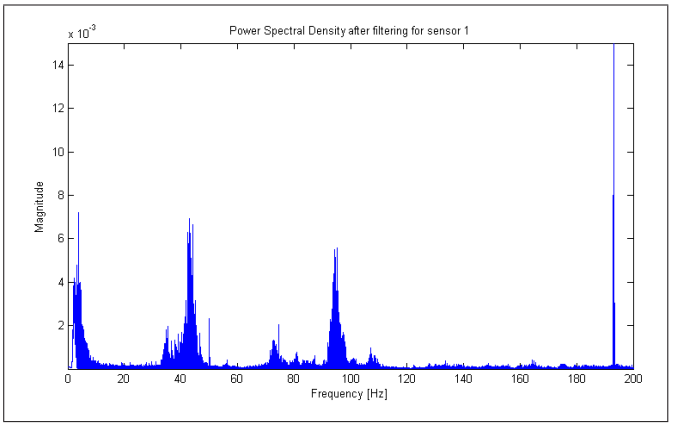

(a) Sensor 1

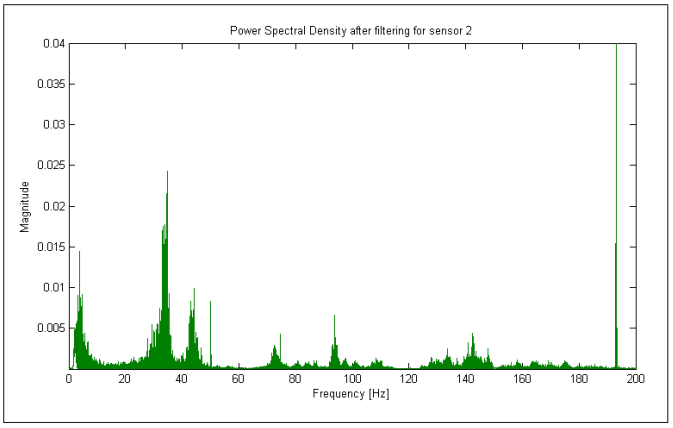

(b) Sensor 2

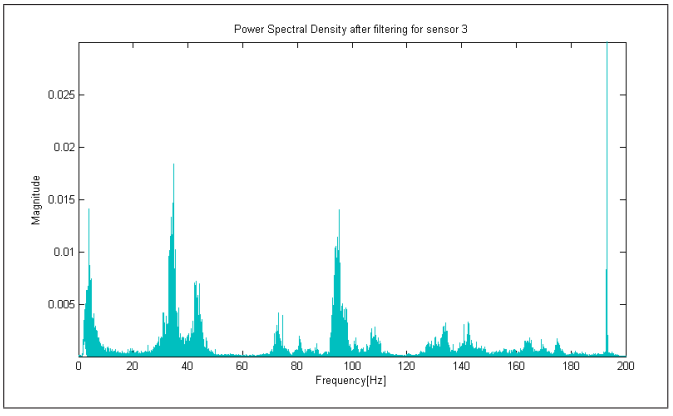

(c) Sensor 3

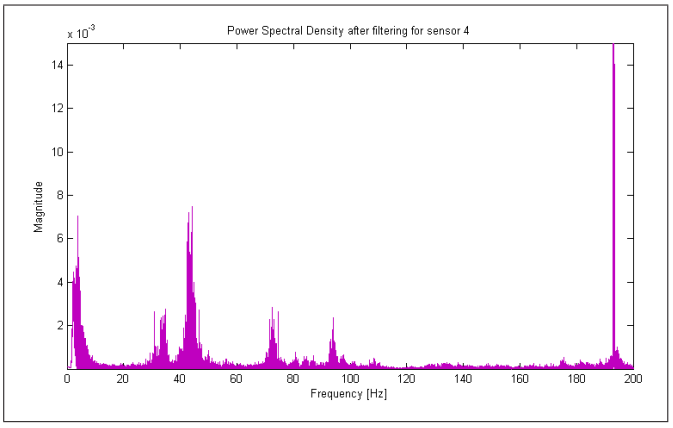

(d) Sensor 4

Figure 6.15: Power Spectral Density for $-10°$ angle of attack.

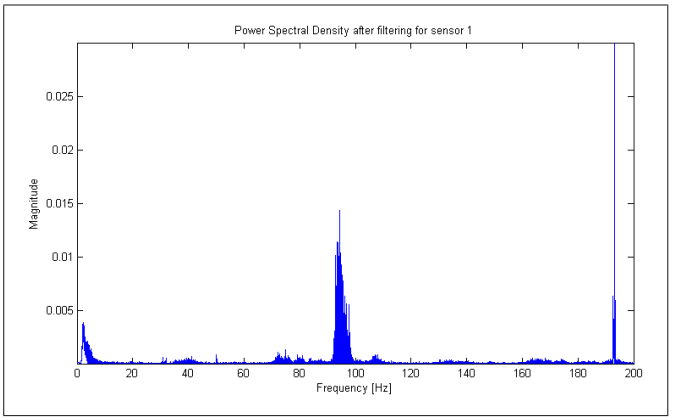

(a) Sensor 1

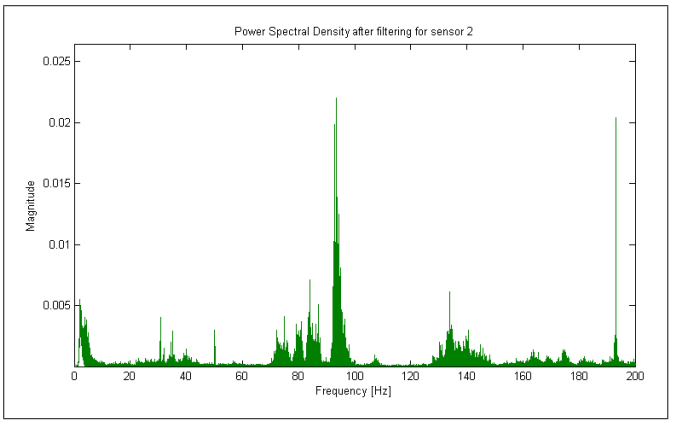

(b) Sensor 2

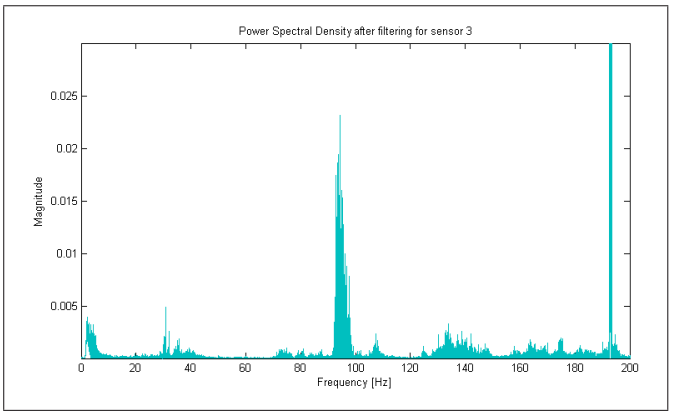

(c) Sensor 3

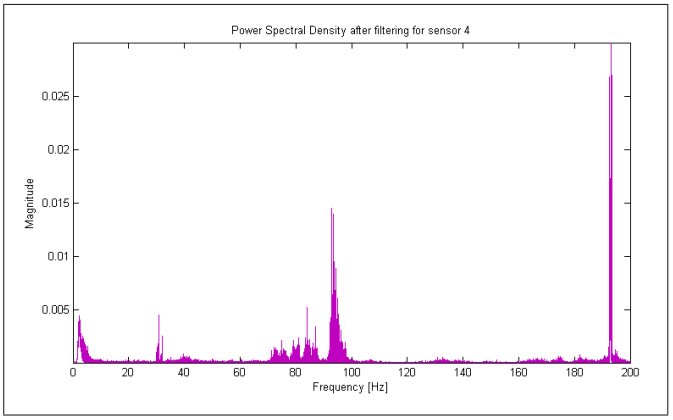

(d) Sensor 4

Figure 6.16: Power Spectral Density for +5° angle of attack.

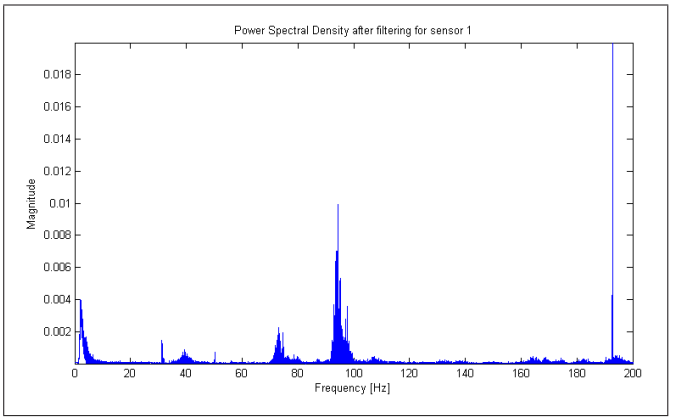

(a) Sensor 1

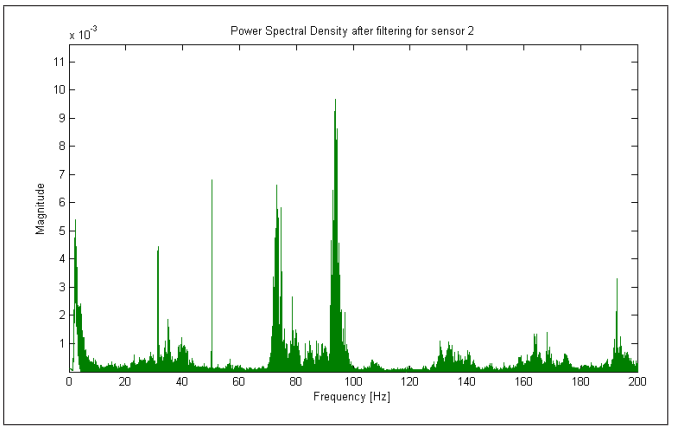

(b) Sensor 2

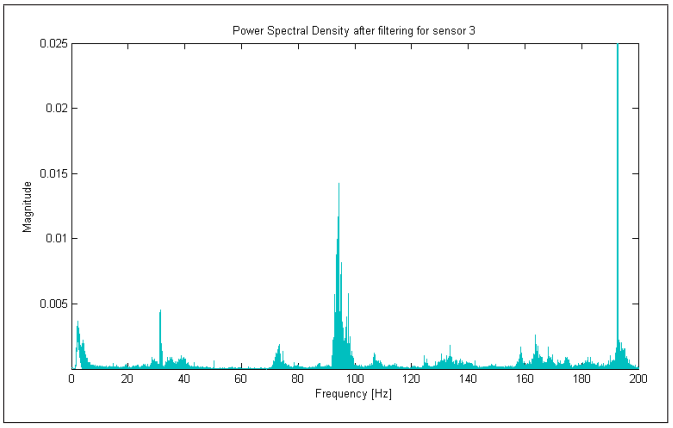

(c) Sensor 3

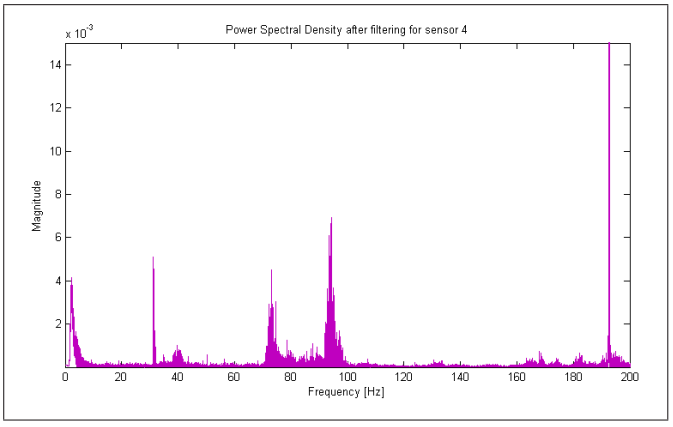

(d) Sensor 4

Figure 6.17: Power Spectral Density for +10° angle of attack.

6.4 Experimental Velocity and Displacement

Once the raw accelerometer data has been filtered and reduced to usable results as discussed in Section 5.5.3, we can discuss the resulting velocity and displacements. Figure 6.18 shows the air speed through the Wind Tunnel for the five experimental runs. As described in Chapter 5 and B, the airspeed was gradually increased until the desired velocity was reached. Data was captured for the entire length of the run, however, we are only interested in the small region when the airspeed was at a steady maximum for the specific run. For the 0° AOA run, this coincides with the region between 390 sec and 420 sec. For the −5°, −10°, +5° and +10° AOA runs, the region is between 120 sec and 150 sec.

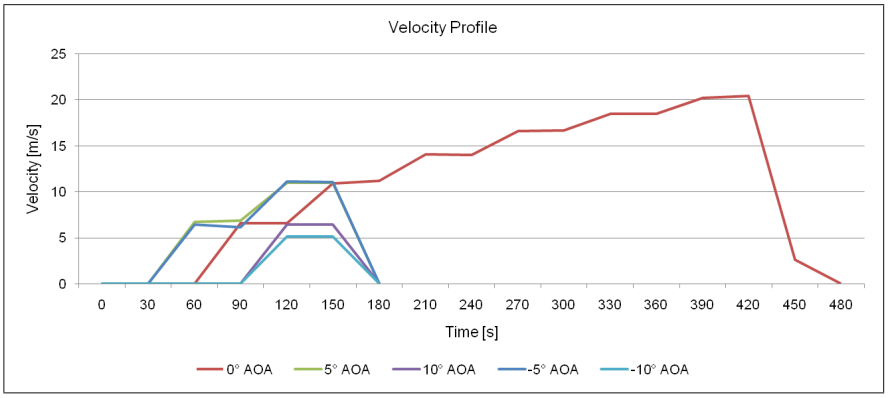

Figure 6.18: Air speed in the Low-speed Wind Tunnel for each of the five experimental runs.

The data sets obtained were then further reduced to a 1 sec interval in the middle of the data region. The velocity and displacement profiles can be seen in Figures 6.19 to 6.23. It is clear in all the displacement results, that a 3 Hz sinusoidal signal is present, i.e. three obvious peaks. This corresponds to the first natural frequency discussed in the previous section.

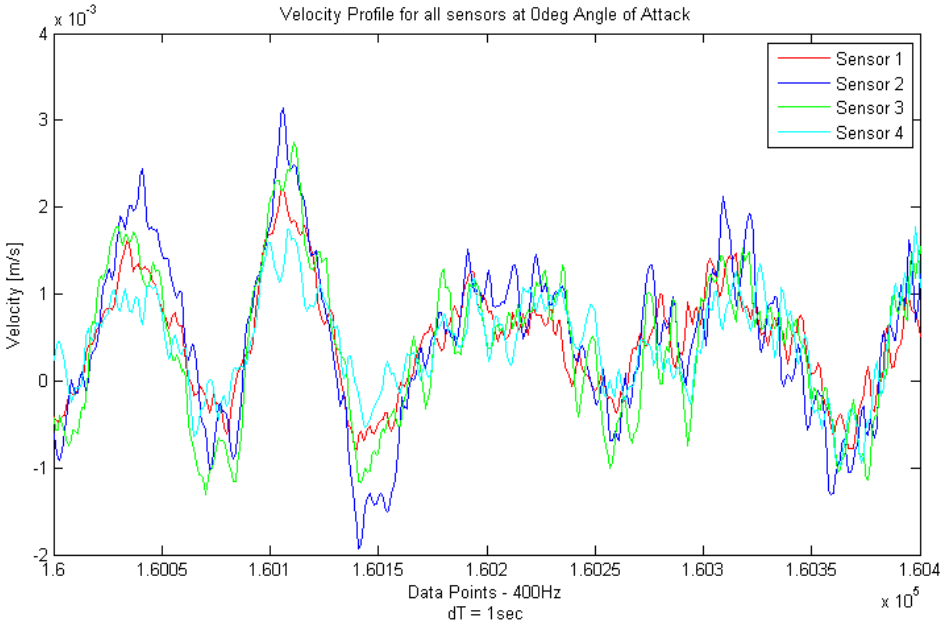

(a) Velocity Profile

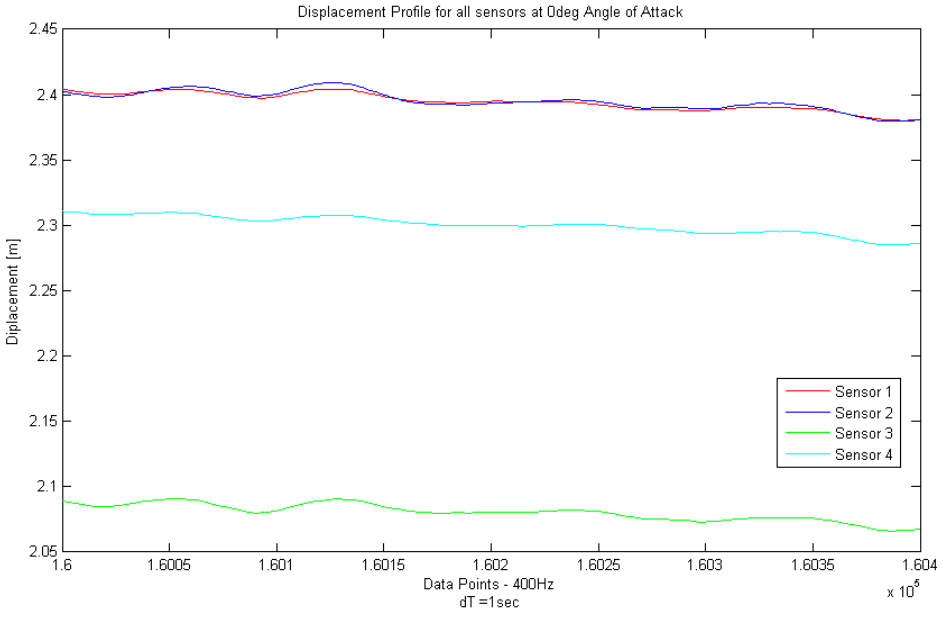

(b) Displacement Profile

Figure 6.19: Velocity and Displacement Profile for all four Accelerometers at 0° Angle of Attack.

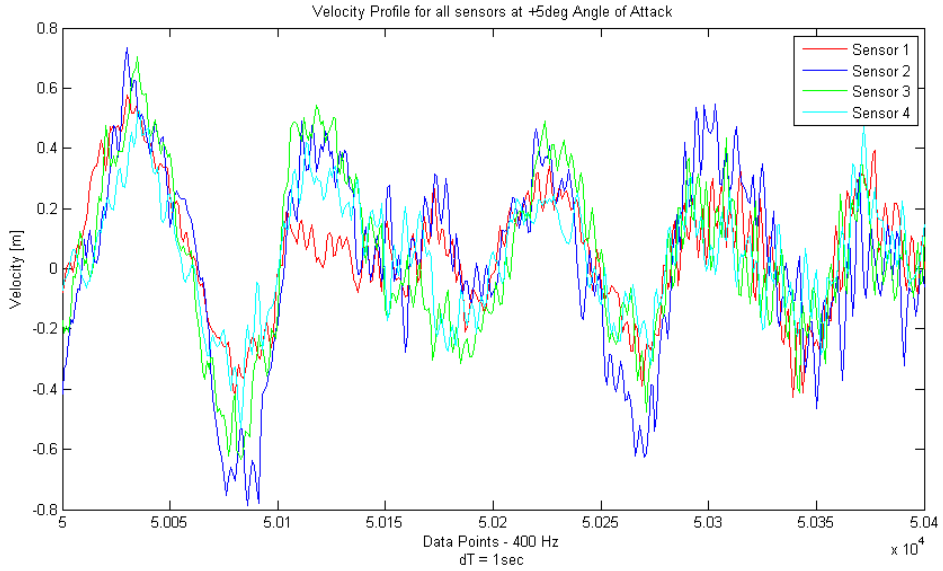

(a) Velocity Profile

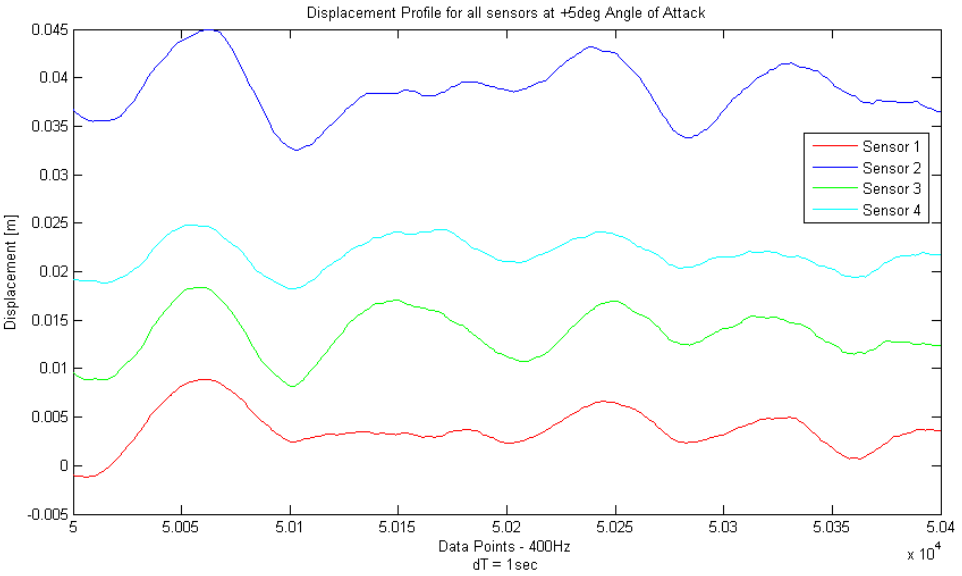

(b) Displacement Profile

Figure 6.20: Velocity and Displacement Profile for all four Accelerometers at 5° Angle of Attack.

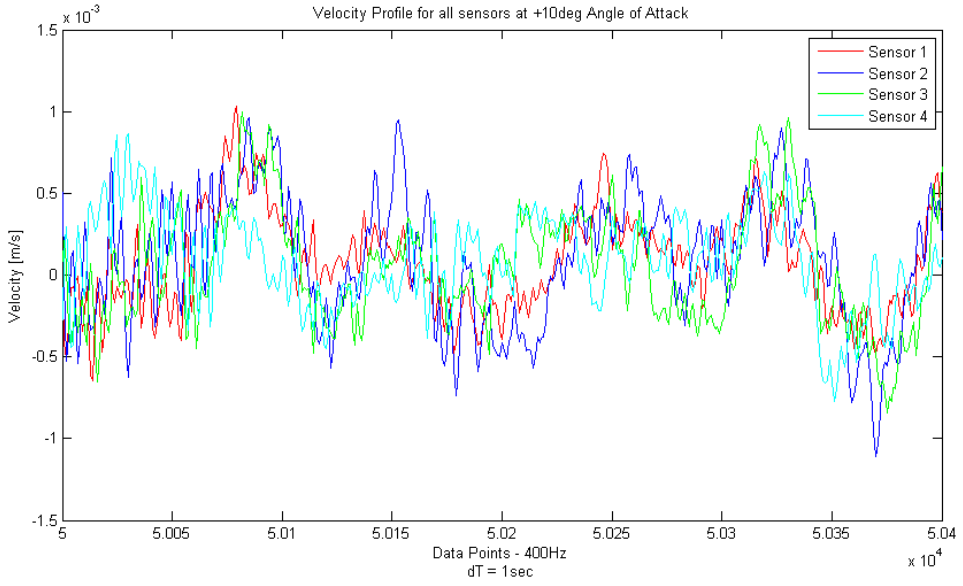

(a) Velocity Profile

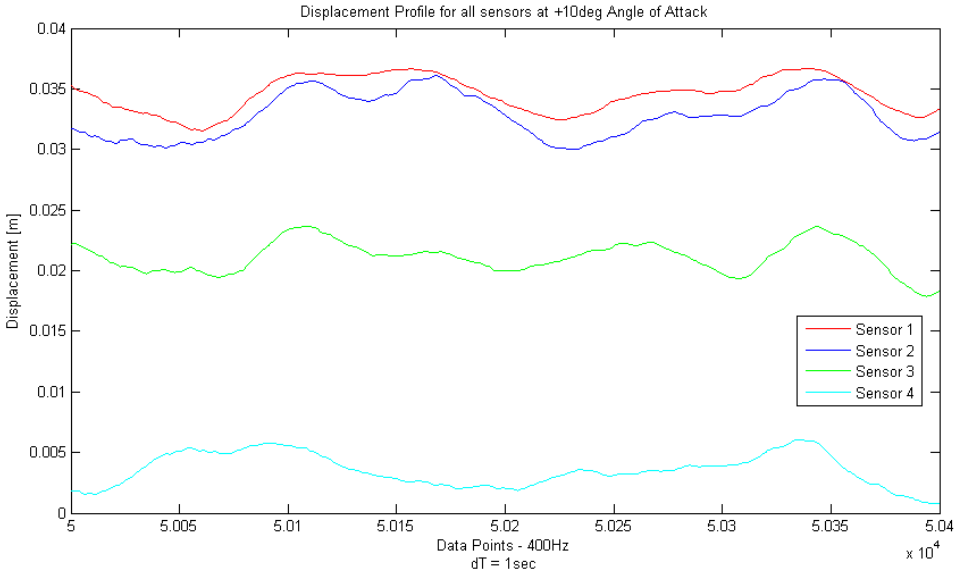

(b) Displacement Profile

Figure 6.21: Velocity and Displacement Profile for all four Accelerometers at 10° Angle of Attack.

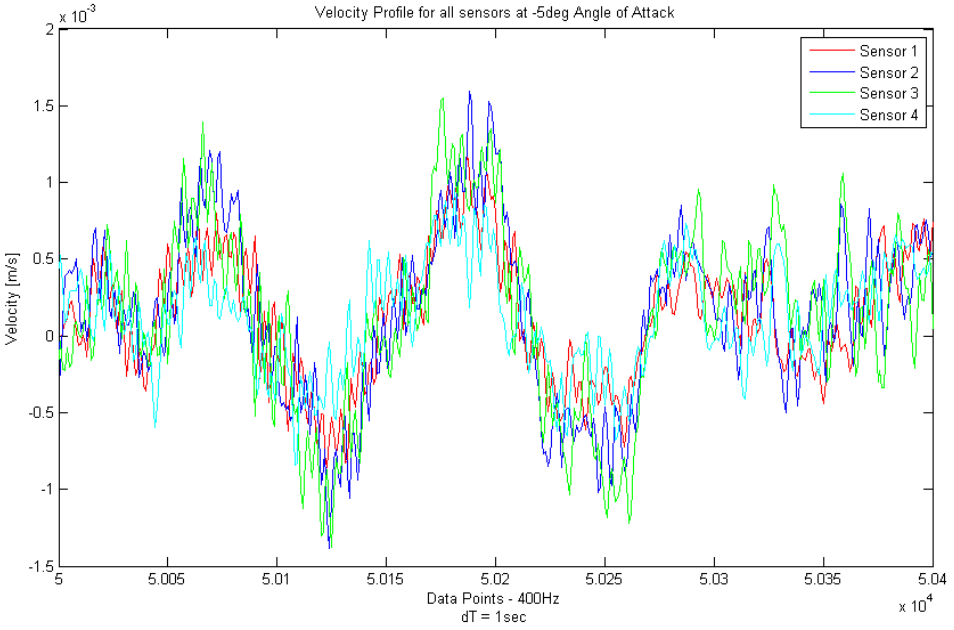

(a) Velocity Profile

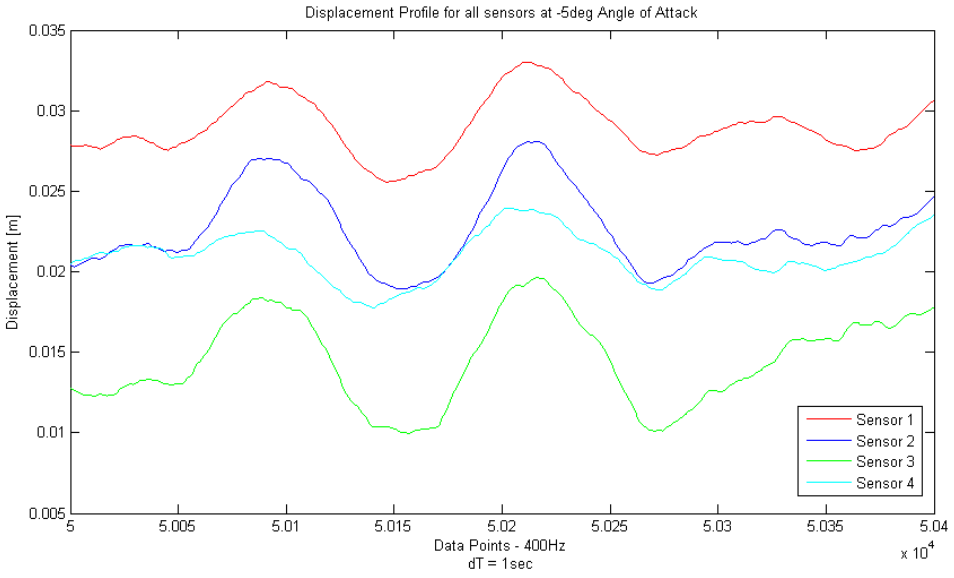

(b) Displacement Profile

Figure 6.22: Velocity and Displacement Profile for all four Accelerometers at $-5°$ Angle of Attack.

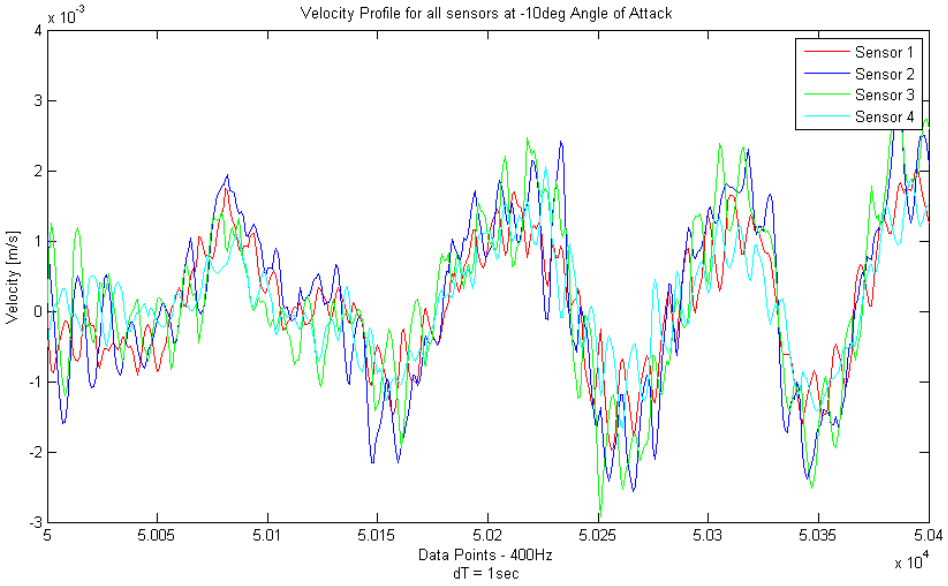

(a) Velocity Profile

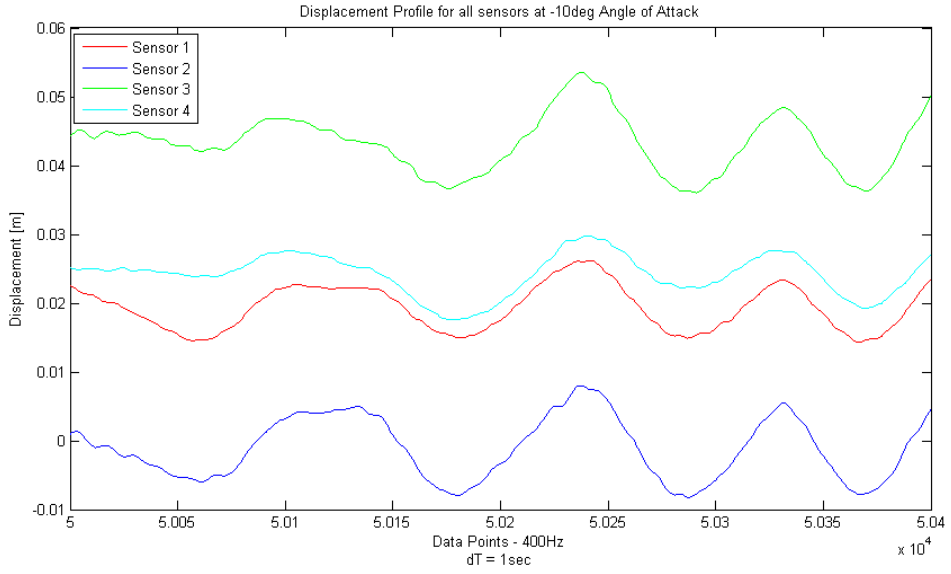

(b) Displacement Profile

Figure 6.23: Velocity and Displacement Profile for all four Accelerometers at $-10°$ Angle of Attack.

We see good correlation between the Velocity results between the four sensors. However, the absolute magnitude of the displacements are not realistic. The shape of the displacement plots correspond between the sensors,however, there is still a factor between the sensors. These displacments are occuring under steady-state conditions and the displacements are relative to the initial unloaded condition. If we look at

the displacement result at 0° AOA (Figure 6.19) we see that sensors 1 and 2 have displaced together, while sensors 3 and 4 are showing some twist (the magnitude of sensor 3 is smaller than the magnitude of sensor 4). This deformed shape corresponds to the first mode shape of the structure. When at 5° AOA (Figure 6.20), the magnitude of sensor 1 and 3 are much smaller than sensors 2 and 4. This is indicating more twist in the steady-state deformed shape. This clearly indicates that the wing structure is not a rigid body and that large amounts of relative motion are present in the structure.

6.4.1 Combining Aerodynamic and Structural

In an attempt to bring the aerodynamic component together with the structural component, the characteristics of the Clark Y profile, as determined by AVL and summarised in Table A.2 below, are used to determine the lift force on the wing under conditions similar to the test runs. The force is then applied to a FEM model and the resultant displacements documented. Ideally, the displacements should correspond to the steady-state deformations of the experimental work. Unfortunately, the magnitude of the experimental displacement results is not adequate and can therefore not be directly compared.

We assume,

$$\text{Lift} = \frac{1}{2}\rho V^2 \cdot CL \cdot A \tag{6.1}$$

$$\text{Drag} = \frac{1}{2}\rho V^2 \cdot CD \cdot A \tag{6.2}$$

$$\text{Pitching Moment} = \frac{1}{2}\rho V^2 \cdot Cm \cdot A \tag{6.3}$$

Property	0° **AOA**	5° **AOA**	10° **AOA**
CL	0.950	1.341	1.713
CD	0.045	0.089	0.146
Cdi	0.045	0.090	0.148
Cm	-0.486	-0.570	-0.644
e	0.958	0.967	0.972
A	0.100	0.100	0.100
ρ	1.225	1.225	1.225

Table 6.4: Characterization of the Clark-Y airfoil using AVL.

Since Equations 6.1 to 6.3 are developed for the full wing span, we need to divide the resulting Lift and Drag by two for half the span before applying the load to the

structural model as seen in Table 6.5. The load was applied at the free end as a point load at the quarter chord position.

Force [N]	0° **AOA**	5° **AOA**	10° **AOA**
Lift	15.208	5.907	2.494
Drag	1.721	0.899	0.472

Table 6.5: Resulting Lift and Drag loads on half the wing span.

	0° **AOA**	5° **AOA**	10° **AOA**
Displacement [m]	0.133	0.051	0.021

Table 6.6: Resulting Displacement in the Z-axis (out of plane) on half the wing span.

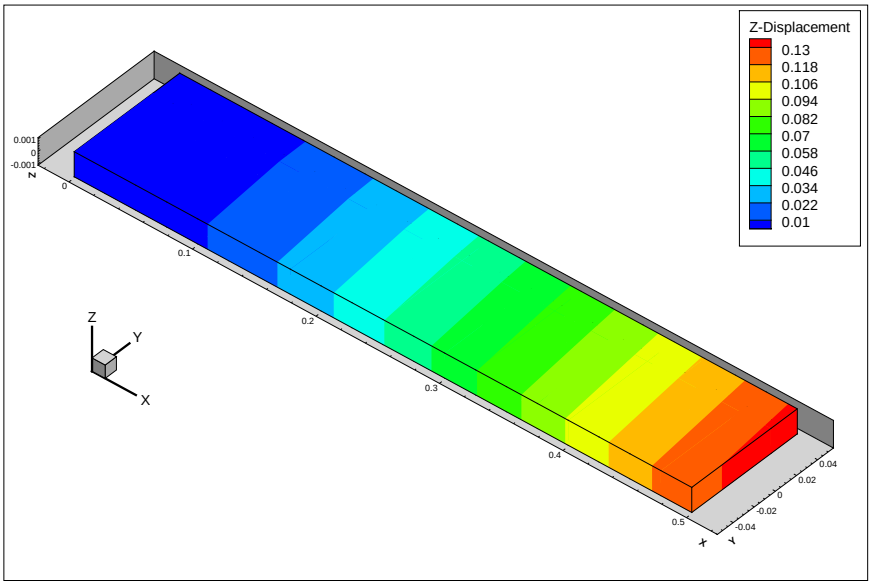

(a) Displacement at 0° Angle of Attack

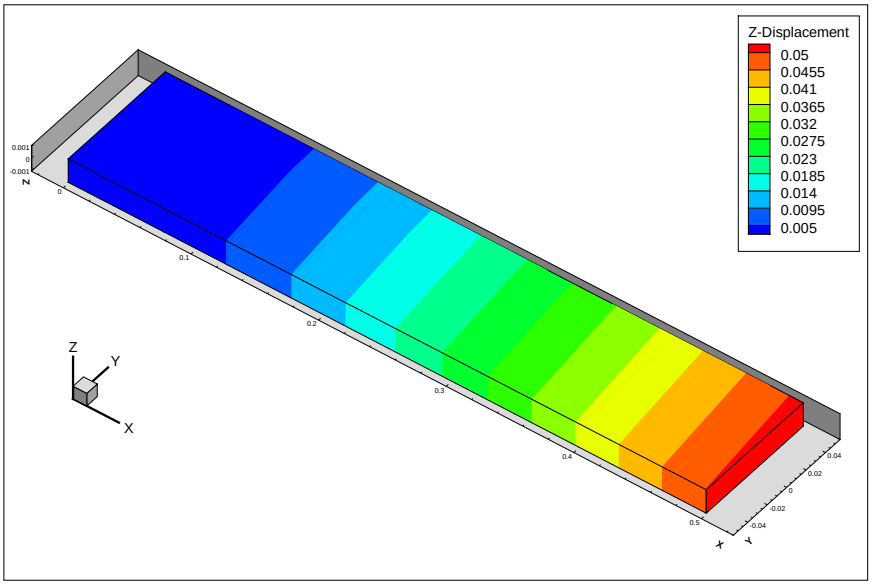

(b) Displacement at 5° Angle of Attack

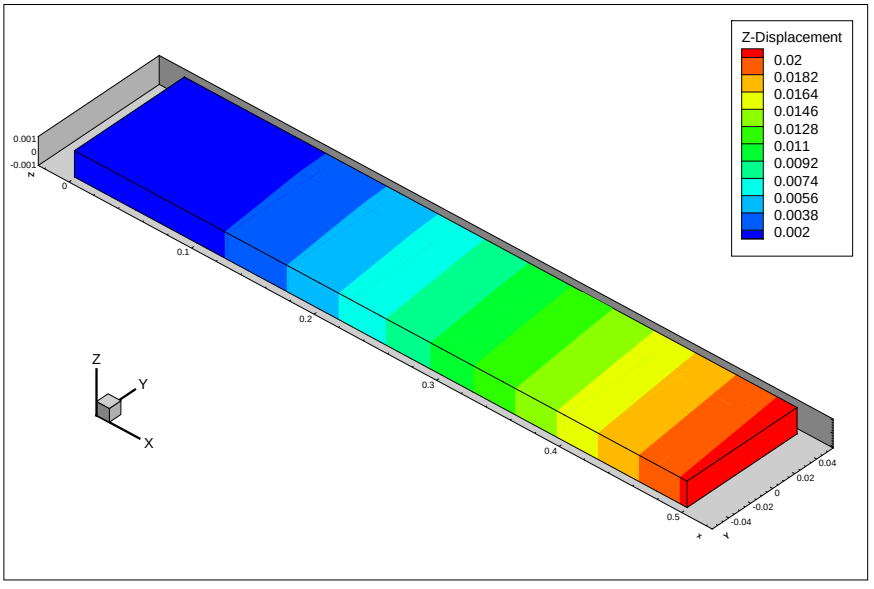

(c) Displacement at 10° Angle of Attack

Figure 6.24: Displacement results for Applied Lifting Load.

Chapter 7

Conclusion

This thesis describes the theoretical and experimental investigation that was conducted as part of the degree Master of Science in Electrical and Electronic Engineering. The aim was to investigate the feasibility of including such an analysis in the development of control systems for UAV's within the ESL at the Department of Electrical and Electronic Engineering at Stellenbosch University.

The investigation includes the development of a structural analysis algorithm using the Finite Element Method, an aerodynamic algorithm for Prandtl's Lifting Line Theory and experimental work in the Low-speed Wing Tunnel.

The structural algorithm is verified by means of commercial software (MSC.Nastran) that was made available to the University. Four test setups were evaluated and the results produced by the structural algorithm correspond quite well. Setup 1 has results that are within 1% of the commercial software. Setup 3 is within 10%, Setup 5 is within 5% and Setup 7 results are within 42% of the results produced by the Nastran. The higher deviance in Setup 7 occurs in the magnitude of the y-displacement. The magnitude of this displacement is very small in comparison to the other direction vectors and due to the type of loading it is felt that the magnitudes for the displacement in the z-direction are most relevant. If we only look at results in the z-direction, we see that for all setups the results are within 1%.

However, the duration of a calculation for such a single static load with a relatively simple model is several seconds. Already at this stage there is an indication that inclusion of even just the structural algorithm in a control system environment, which works in real time, is not a viable option, as modern control systems do not have the luxury of several seconds for processing. Additionally, the higher frequency responses found in a real time analysis will require higher precision. As described in Section 3.4.6, this increase in computational cost outweighs gain in implementation.

With regard to the experimental work, we see that the natural frequencies occurring in the structure during simulation correspond well to the frequencies with

high intensity peaks in the PSD of the accelerometer data. The deviations in these results can be attributed to the difference in mass between the simulation model and the experimental model due to the addition of sensors and the profile. Additionally, the experimental model is constructed slightly longer, 2cm, so as to accommodate mounting to the roof of the test section. Lastly, the connection between the model and the test section is not perfectly rigid as assumed in the simulation.

Due to the difficulties associated with the integrating of the accelerometer data to produce displacement results, this aspect cannot be compared directly with the structural algorithm at this stage. However, in Figures 6.6 and 6.8 we can see the twisting deflection of the structure in when a load is applied to a location other than the center of the beam, which influences the AOA. Additionally, the experimental displacements show offsets between the sensors indicating relative twisting of the plat-spar.

This confirms that the structural and aerodynamic components cannot be separated when analysing a wing-like structure.

7.1 Future Work and Recommendations

Many of the conclusions and comments mentioned above lend themselves to areas of future investigation.

The structural algorithm can be improved in complexity to include more diverse and complex structures with options as to the type of elements used. Additional solution methods and techniques should be investigated to see if there might be a more suitable method for solving large sparse matrices and other aspects of the algorithm that could reduce the simulation time. Refinement of the programming technique should also be conducted.

Similarly, the aerodynamic algorithm should be versatile enough to accommodate a variety of wing configurations. Integration between the aerodynamic and structural algorithms should also be investigated. It would be informative to see this time dependent interaction in simulation since finer details at higher frequencies could be identified that might be missed during experimental analysis. However, it is again clear that limitations to our current hardware implies that implementation of an aeroelastic component as part of a control system is not yet viable.

With regard to the experimental work, additional study of the flow behaviour and characteristics of the Low-Speed Wind Tunnel will aid in understanding the aerodynamic behaviour noted during experimental runs. This will also lead to better post-processing capabilities, since if all the causes of noise and disturbance have been identified, methods can be found to minimise their impact. Additional research into

the appropriate type of sensors and other methods of data capture would also expand the capabilities of this research group.

Appendix A

AVL Input Files

Clark Y						
♯Mach						
0.0						
♯IYsym	IZsym	Zsym				
0	0	0.0				
♯Sref	Cref	Bref				
0.15	0.15	1.0				
♯Xref	Yref	Zref				
0.0	0.0	0.0				
SURFACE						
Wing						
♯Nchordwise	Cspace	Nspanwise	Sspace			
32	1.0	40	1.0			
YDUPLICATE						
0.0						
ANGLE						
0.0						
SECTION						
♯Xle	Yle	Zle	Chord	Ainc	Nspanwise	Sspace
0.0	0.0	0.0	0.15	0.0		
AFILE						
clarkY.dat						
CLAF						
1.09384						
SECTION						
♯Xle	Yle	Zle	Chord	Ainc	Nspanwise	Sspace
0.0	0.5	0.	0.15	0.0		
AFILE						
clarkY.dat						
CLAF						
1.09384						

Table A.1: Input File - *ClarkY_NC32_NS40.avl*

Clark Y Airfoil Profile - Top Surface			
X Co-ordinate	Y Co-ordinate	X Co-ordinate	Y Co-ordinate
0.15	0	0.066	0.013457625
0.15	0.000089895	0.063	0.013584855
0.1485	0.00044535	0.06	0.01367568
0.147	0.000800025	0.057	0.01372818
0.1455	0.00115302	0.054	0.01374399
0.144	0.00150348	0.051	0.013726185
0.141	0.002193585	0.048	0.013677855
0.138	0.00286734	0.045	0.01360206
0.135	0.003525375	0.042	0.01350024
0.132	0.004168365	0.039	0.0133626
0.129	0.0047961	0.036	0.01317462
0.126	0.00540804	0.033	0.012921495
0.123	0.006003675	0.03	0.01258803
0.12	0.00658254	0.027	0.012160305
0.117	0.007144215	0.024	0.011635605
0.114	0.007688475	0.021	0.0110154
0.111	0.008215125	0.018	0.01029306
0.108	0.008723985	0.015	0.009449715
0.105	0.009214935	0.012	0.00846462
0.102	0.009687645	0.009	0.007313565
0.099	0.01014069	0.0075	0.006641295
0.096	0.01057233	0.006	0.005869245
0.093	0.010980825	0.0045	0.004953225
0.09	0.011364495	0.003	0.003806025
0.087	0.011721765	0.0018	0.002678715
0.084	0.0120522	0.0012	0.00206025
0.081	0.01235568	0.0006	0.00133857
0.078	0.012632175	0.0003	0.000870375
0.075	0.01288158	0.00015	0.000559065
0.072	0.01310358	0.000075	0.00035085
0.069	0.013296405		

Clark Y Airfoil Profile - Lower Surface			
X Co-ordinate	Y Co-ordinate	X Co-ordinate	Y Co-ordinate
0	0	0.069	-0.003065295
0.000075	-0.0007005	0.072	-0.00295479
0.00015	-0.00089127	0.075	-0.002844285
0.0003	-0.001171695	0.078	-0.00273393
0.0006	-0.00157689	0.081	-0.00262371
0.0012	-0.00214293	0.084	-0.00251358
0.0018	-0.002545995	0.087	-0.00240348
0.003	-0.003040845	0.09	-0.002293395
0.0045	-0.00339084	0.093	-0.002183265
0.006	-0.003678165	0.096	-0.002073105
0.0075	-0.00390678	0.099	-0.00196293
0.009	-0.004069155	0.102	-0.001852725
0.012	-0.004268925	0.105	-0.001742535
0.015	-0.00440679	0.108	-0.001632345
0.018	-0.004494495	0.111	-0.00152217
0.021	-0.00453606	0.114	-0.001411995
0.024	-0.00453819	0.117	-0.00130182
0.027	-0.00450735	0.12	-0.001191645
0.03	-0.00444984	0.123	-0.00108147
0.033	-0.004371675	0.126	-0.000971295
0.036	-0.004277715	0.129	-0.00086112
0.039	-0.00417246	0.132	-0.000750945
0.042	-0.00406044	0.135	-0.00064077
0.045	-0.003946185	0.138	-0.000530595
0.048	-0.003833475	0.141	-0.00042042
0.051	-0.00372264	0.144	-0.000310245
0.054	-0.00361305	0.1455	-0.000255165
0.057	-0.00350409	0.147	-0.000200085
0.06	-0.003395115	0.1485	-0.00014499
0.063	-0.00328563	0.15	0
0.066	-0.00317562		

Table A.2: Input File for Airfoil Profile - *ClarkY.dat*

Appendix B

Experimental Work

B.1 Experimental Procedure

This section discusses the tasks performed in preparation for the day of testing as well as the specific tasks during data capture.

B.1.1 Before the Day of Testing

- Build experimental model, including mounting bracket and base plate.
- Check sensors are generating usable data.
- Determine the sensor gains.
- Prepare wind tunnel test section.

B.1.2 The Day of Testing

- Transport supporting equipment to Low-speed Wind Tunnel.
- Open the roll doors.
- Check for water in fan enclosure.
- Check/clear airflow area and clean out leaves.
- Check that the experimental model is correctly and securely fixed to the test section.
- Setup supporting equipment and ensure all sensors are in working order.
- Calibrate pressure transducers.
- Mount the static pitot tube in the test section

B.1.3 Data Capture

- Clear the test area.
- Ensure the speed control flaps are closed.
- Document the angle of attack. The angle of attack was varied between $+10°$ and $-10°$ in increments of $5°$.
- Start the data logger.
- Start the fan.
- Gradually open the speed control flaps until desired air speed reached.
- Allow steady state conditions to be reached.
- Continuously document pressure readings.
- Stop the fan.
- Stop data logger once the air velocity is zero.
- Repeat the process at varying angles of attack.

B.2 Filtering Coefficients

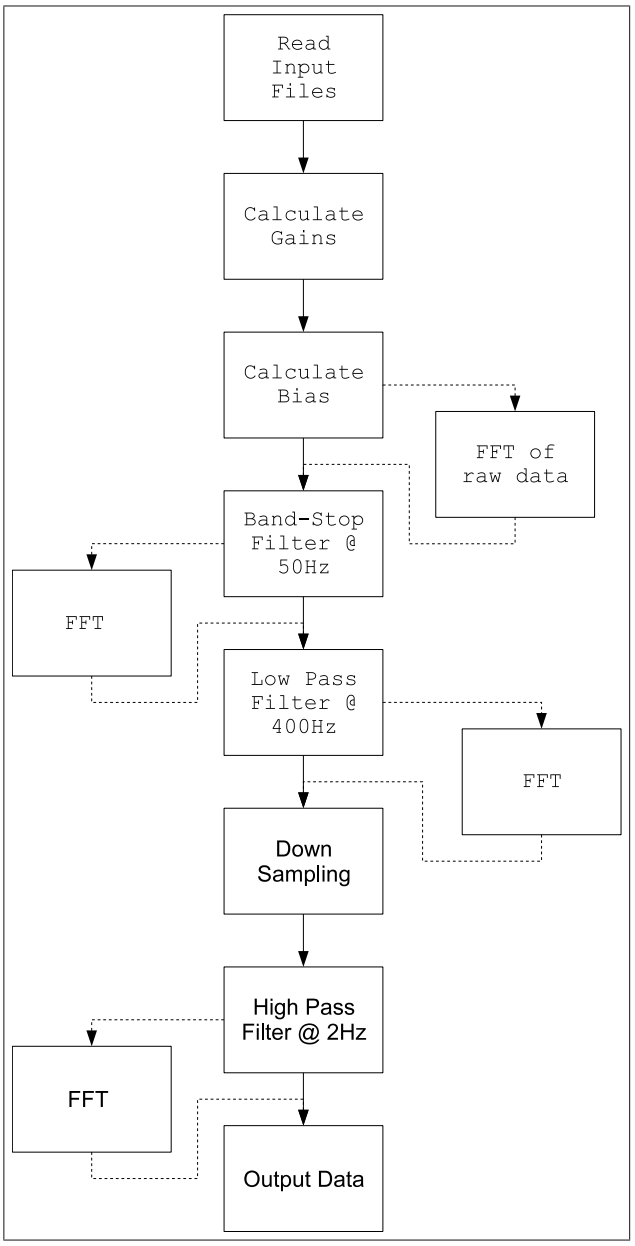

Figure B.1: Procedure for reducing the raw accelerometer data to useable results

Filter type	Low Pass
Filter model	Butterworth
Filter order	4
Sampling Frequency	2.5 KHz
Cut Frequency	0.400 KHz
ACoef	0.022869681785594270
	0.0914787271423770780
	0.137218090713565610
	0.0914787271423770780
	0.022869681785594270
BCoef	1.00
	-1.41198350119657730
	1.12276608082121920
	-0.408070951880239790
	0.0632116957162536240

Table B.1: Description and Coefficients for the Low Pass Filter

Filter type	Band Stop
Filter model	Butterworth
Filter order	2
Sampling Frequency	2.5 KHz
Fc1	0.049 KHz
Fc2	0.051 KHz
ACoef	0.983251330614836160
	-3.90200472435127830
	5.83775113931181270
	-3.90200472435127830
	0.983251330614836160
BCoef	1.00
	-3.96141878685919480
	5.91611346498272270
	-3.94736363944446020
	0.992916593713265680

Table B.2: Description and Coefficients for the Band Stop Filter

Filter type	High Pass
Filter model	Butterworth
Filter order	6
Sampling Frequency	416 Hz
Cut Frequency	2 Hz
ACoef	0.944470027127426780 -5.66682016276456050 14.1670504069114020 -18.8894005425485360 14.1670504069114020 -5.66682016276456050 0.944470027127426780
BCoef	1.00 -5.88328758253404690 14.4232293179070150 -18.8597917328772160 13.8728812129831290 -5.44286649243345980 0.889835277671631060

Table B.3: Description and Coefficients for the High Pass Filter

Appendix C

Datasheet - MMA1213D

Freescale Semiconductor
Technical Data

MMA1213D
Rev 2, 03/2006

Surface Mount Micromachined Accelerometer

MMA1213

The MMA series of silicon capacitive, micromachined accelerometers feature signal conditioning, a 4-pole low pass filter and temperature compensation. Zero-g offset full scale span and filter cut-off are factory set and require no external devices. A full system self-test capability verifies system functionality.

MMA1213D: Z AXIS SENSITIVITY MICROMACHINED ACCELEROMETER ±50g

Features

- Integral Signal Conditioning
- Linear Output
- Ratiometric Performance
- 4th Order Bessel Filter Preserves Pulse Shape Integrity
- Calibrated Self-test
- Low Voltage Detect, Clock Monitor, and EPROM Parity Check Status
- Transducer Hermetically Sealed at Wafer Level for Superior Reliability
- Robust Design, High Shocks Survivability

Typical Applications

- Vibration Monitoring and Recording
- Impact Monitoring

D SUFFIX
EG SUFFIX (Pb-FREE)
16-LEAD SOIC
CASE 475-01

ORDERING INFORMATION			
Device Name	**Temperature Range**	**Case No.**	**Package**
MMA1213D	–40° to 125°C	475-01	SOIC-16
MMA1213DR2	–40° to 125°C	475-01	SOIC16, Tape & Reel
MMA1213EG	–40° to 125°C	475-01	SOIC-16
MMA1213EGR2	–40° to 125°C	475-01	SOIC16, Tape & Reel

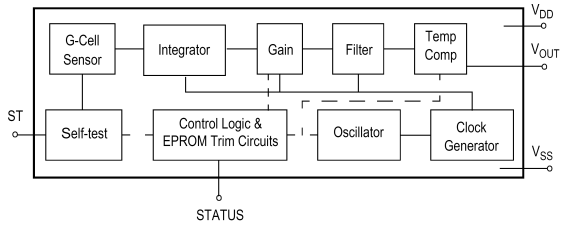

Figure 1. Simplified Accelerometer Functional Block Diagram

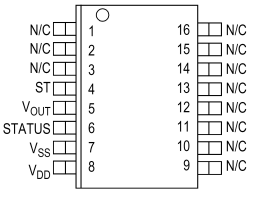

Figure 2. Pin Connections

freescale semiconductor

Figure C.1: Datasheet - MMA1213 - Page 01

Table 1. Maximum Ratings
(Maximum ratings are the limits to which the device can be exposed without causing permanent damage.)

Rating	Symbol	Value	Unit
Powered Acceleration (all axes)	G_{pd}	1500	g
Unpowered Acceleration (all axes)	G_{upd}	2000	g
Supply Voltage	V_{DD}	–0.3 to +7.0	V
Drop Test (1)	D_{drop}	1.2	m
Storage Temperature Range	T_{stg}	–40 to +125	°C

1. Dropped onto concrete surface from any axis.

ELECTRO STATIC DISCHARGE (ESD)

WARNING: This device is sensitive to electrostatic discharge.

Although the Freescale accelerometers contain internal 2kV ESD protection circuitry, extra precaution must be taken by the user to protect the chip from ESD. A charge of over 2000 volts can accumulate on the human body or associated test equipment. A charge of this magnitude can alter the performance or cause failure of the chip. When handling the accelerometer, proper ESD precautions should be followed to avoid exposing the device to discharges which may be detrimental to its performance.

Figure C.2: Datasheet - MMA1213 - Page 02

Table 2. Operating Characteristics
(Unless otherwise noted: –40°C ≤ T_A ≤ +105°C, 4.75 ≤ V_{DD} ≤ 5.25, Acceleration = 0g, Loaded output.(1))

Characteristic	Symbol	Min	Typ	Max	Unit
Operating Range (2)					
Supply Voltage(3)	V_{DD}	4.75	5.00	5.25	V
Supply Current	I_{DD}	3.0	—	6.0	mA
Operating Temperature Range	T_A	–40	—	+125	C
Acceleration Range	g_{FS}	—	56.3	—	g
Output Signal					
Zero g (T_A = 25°C, V_{DD} = 5.0 V)(4)	V_{OFF}	2.35	2.5	2.65	V
Zero g	$V_{OFF,V}$	0.46 V_{DD}	0.50 V_{DD}	0.54 V_{DD}	V
Sensitivity (T_A = 25°C, V_{DD} = 5.0 V)(5)	S	38	40	42	mV/g
Sensitivity	S_V	7.44	8	8.56	mV/g/V
Bandwidth Response	f_{-3dB}	360	400	440	Hz
Nonlinearity	NL_{OUT}	–1.0	—	1.0	% FSO
Noise					
RMS (0.1-1 kHz)	n_{RMS}	—	—	2.8	mVrms
Power Spectral Density	n_{PSD}	—	110	—	$\mu V/(Hz^{1/2})$
Clock Noise (without RC load on output)(6)	n_{CLK}	—	2.0	—	mVpk
Self-Test					
Output Response	g_{ST}	24	30	36	g
Input Low	V_{IL}	V_{SS}	—	0.3 × V_{DD}	V
Input High	V_{IH}	0.7 × V_{DD}	—	V_{DD}	V
Input Loading(7)	I_{IN}	–30	–100	–260	μA
Response Time(8)	t_{ST}	—	2.0	10	ms
Status(9), (10)					
Output Low (I_{load} = 100 μA)	V_{OL}	—	—	0.4	V
Output High (I_{load} = 100 μA)	V_{OH}	V_{DD} –.8	—	—	V
Minimum Supply Voltage (LVD Trip)	V_{LVD}	2.7	3.25	4.0	V
Clock Monitor Fail Detection Frequency	f_{MIN}	50	—	260	kHz
Output Stage Performance					
Electrical Saturation Recovery Time(11)	t_{DELAY}	—	0.2	—	ms
Full Scale Output Range (I_{OUT} = 200 μA)	V_{FSO}	–0.25	—	V_{DD} –0.25	V
Capacitive Load Drive(12)	C_L	—	—	100	pF
Output Impedance	Z_O	—	300	—	W
Mechanical Characteristics					
Transverse Sensitivity(13)	$V_{XZ,YZ}$	—	—	5.0	% FSO
Package Resonance	f_{PKG}	—	10	—	kHz

1. For a loaded output the measurements are observed after an RC filter consisting of a 1 kΩ resistor and a 0.01 μF capacitor to ground.
2. These limits define the range of operation for which the part will meet specification.
3. Within the supply range of 4.75 and 5.25 V, the device operates as a fully calibrated linear accelerometer. Beyond these supply limits the device may operate as a linear device but is not guaranteed to be in calibration.
4. The device can measure both + and – acceleration. With no input acceleration the output is at mid supply. For positive acceleration the output will increase above V_{DD}/2 and for negative acceleration the output will decrease below V_{DD}/2.
5. The device is calibrated at 20g.
6. At clock frequency ≅70 kHz.
7. The digital input pin has an internal pull-down current source to prevent inadvertent self test initiation due to external board level leakages.
8. Time for the output to reach 90% of its final value after a self-test is initiated.
9. The Status pin output is not valid following power-up until at least one rising edge has been applied to the self-test pin. The Status pin is high whenever the self-test input is high, as a means to check the connectivity of the self-test and Status pins in the application.
10. The Status pin output latches high if a Low Voltage Detection or Clock Frequency failure occurs, or the EPROM parity changes to odd. The Status pin can be reset low if the self-test pin is pulsed with a high input for at least 100 μs, unless a fault condition continues to exist.
11. Time for amplifiers to recover after an acceleration signal causes them to saturate.
12. Preserves phase margin (60°) to guarantee output amplifier stability.
13. A measure of the device's ability to reject an acceleration applied 90° from the true axis of sensitivity.

Figure C.3: Datasheet - MMA1213 - Page 03

PRINCIPLE OF OPERATION

The Freescale accelerometer is a surface-micromachined integrated-circuit accelerometer.

The device consists of a surface micromachined capacitive sensing cell (g-cell) and a CMOS signal conditioning ASIC contained in a single integrated circuit package. The sensing element is sealed hermetically at the wafer level using a bulk micromachined “cap" wafer.

The g-cell is a mechanical structure formed from semiconductor materials (poly silicon) using semiconductor processes (masking and etching). It can be modeled as two stationary plates with a moveable plate in-between. The center plate can be deflected from its rest position by subjecting the system to an acceleration (Figure 3).

When the center plate deflects, the distance from it to one fixed plate will increase by the same amount that the distance to the other plate decreases. The change in distance is a measure of acceleration.

The g-cell plates form two back-to-back capacitors (Figure 4). As the center plate moves with acceleration, the distance between the plates changes and each capacitor's value will change, ($C = A\varepsilon/D$). Where A is the area of the plate, ε is the dielectric constant, and D is the distance between the plates.

The CMOS ASIC uses switched capacitor techniques to measure the g-cell capacitors and extract the acceleration data from the difference between the two capacitors. The ASIC also signal conditions and filters (switched capacitor) the signal, providing a high level output voltage that is ratiometric and proportional to acceleration.

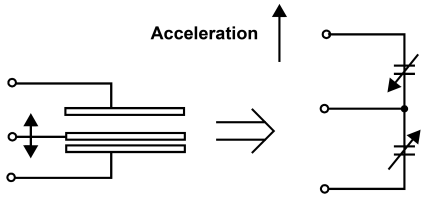

Figure 3. Transducer Physical Model

Figure 4. Equivalent Circuit Model

SPECIAL FEATURES

Filtering

The Freescale accelerometers contain an on board 4-pole switched capacitor filter. A Bessel implementation is used because it provides a maximally flat delay response (linear phase) thus preserving pulse shape integrity. Because the filter is realized using switched capacitor techniques, there is no requirement for external passive components (resistors and capacitors) to set the cut-off frequency.

Self-Test

The sensor provides a self-test feature that allows the verification of the mechanical and electrical integrity of the accelerometer at any time before or after installation. This feature is critical in applications such as automotive air bag systems where system integrity must be ensured over the life of the vehicle. A fourth “plate" is used in the g-cell as a self-test plate. When the user applies a logic high input to the self-test pin, a calibrated potential is applied across the self-test plate and the moveable plate. The resulting electrostatic force ($Fe = {}^1/_2\, AV^2/d^2$) causes the center plate to deflect. The resultant deflection is measured by the accelerometer's control ASIC and a proportional output voltage results. This procedure assures that both the mechanical (g-cell) and electronic sections of the accelerometer are functioning.

Ratiometricity

Ratiometricity simply means that the output offset voltage and sensitivity will scale linearly with applied supply voltage. That is, as you increase supply voltage the sensitivity and offset increase linearly; as supply voltage decreases, offset and sensitivity decrease linearly. This is a key feature when interfacing to a microcontroller or an A/D converter because it provides system level cancellation of supply induced errors in the analog to digital conversion process.

Status

Freescale accelerometers include fault detection circuitry and a fault latch. The Status pin is an output from the fault latch, OR'd with self-test, and is set high whenever one (or more) of the following events occur:

- Supply voltage falls below the Low Voltage Detect (LVD) voltage threshold
- Clock oscillator falls below the clock monitor minimum frequency
- Parity of the EPROM bits becomes odd in number.

The fault latch can be reset by a rising edge on the self-test input pin, unless one (or more) of the fault conditions continues to exist.

Figure C.4: Datasheet - MMA1213 - Page 04

BASIC CONNECTIONS

Pinout Description

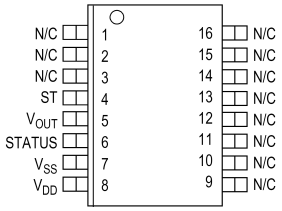

Table 3. Pin Descriptions

Pin No.	Pin Name	Description
1 thru 3	—	Leave unconnected
4	ST	Logic input pin used to initiate self-test
5	V_{OUT}	Output voltage of the accelerometer
6	STATUS	Logic output pin to indicate fault
7	V_{SS}	The power supply ground
8	V_{DD}	The power supply input
9 thru 13	Trim pins	Used for factory trim. Leave unconnected
14 thru 16	—	No internal connection. Leave unconnected

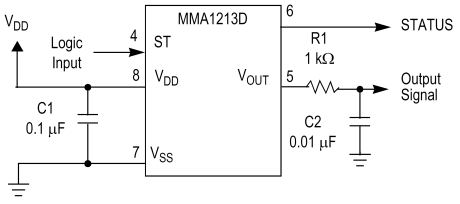

Figure 5. SOIC Accelerometer with Recommended Connection Diagram

PCB Layout

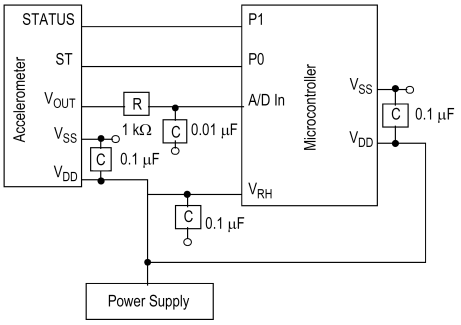

Figure 6. Recommended PCB Layout for Interfacing Accelerometer to Microcontroller

NOTES:

1. Use a 0.1 µF capacitor on V_{DD} to decouple the power source.
2. Physical coupling distance of the accelerometer to the microcontroller should be minimal.
3. Place a ground plane beneath the accelerometer to reduce noise, the ground plane should be attached to all of the open ended terminals shown in Figure 6.
4. Use an RC filter of 1 kΩ and 0.01 µF on the output of the accelerometer to minimize clock noise (from the switched capacitor filter circuit).
5. PCB layout of power and ground should not couple power supply noise.
6. Accelerometer and microcontroller should not be a high current path.
7. A/D sampling rate and any external power supply switching frequency should be selected such that they do not interfere with the internal accelerometer sampling frequency. This will prevent aliasing errors.

Figure C.5: Datasheet - MMA1213 - Page 05

Dynamic Acceleration Sensing Direction

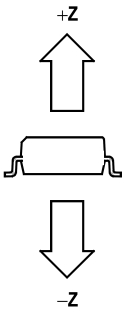

Acceleration of the package in the +Z direction (center plate moves in the –Z direction) will result in an increase in the output.

Activation of Self test moves the center plate in the –Z direction, resulting in an increase in the output.

Side View

Static Acceleration Sensing Direction

Direction of Earth's gravity field(1)

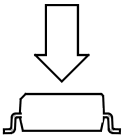

Side View

1. When positioned as shown, the Earth's gravity will result in a positive 1g output.

Figure C.6: Datasheet - MMA1213 - Page 06

MINIMUM RECOMMENDED FOOTPRINT FOR SURFACE MOUNTED APPLICATIONS

Surface mount board layout is a critical portion of the total design. The footprint for the surface mount packages must be the correct size to ensure proper solder connection interface between the board and the package. With the correct footprint, the packages will self-align when subjected to a solder reflow process. It is always recommended to design boards with a solder mask layer to avoid bridging and shorting between solder pads.

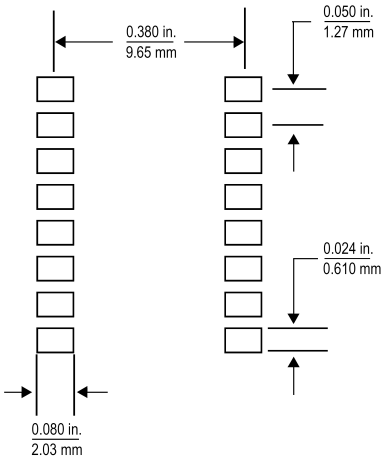

Figure 7. Footprint SOIC-16 (Case 475-01)

Figure C.7: Datasheet - MMA1213 - Page 07

PACKAGE DIMENSIONS

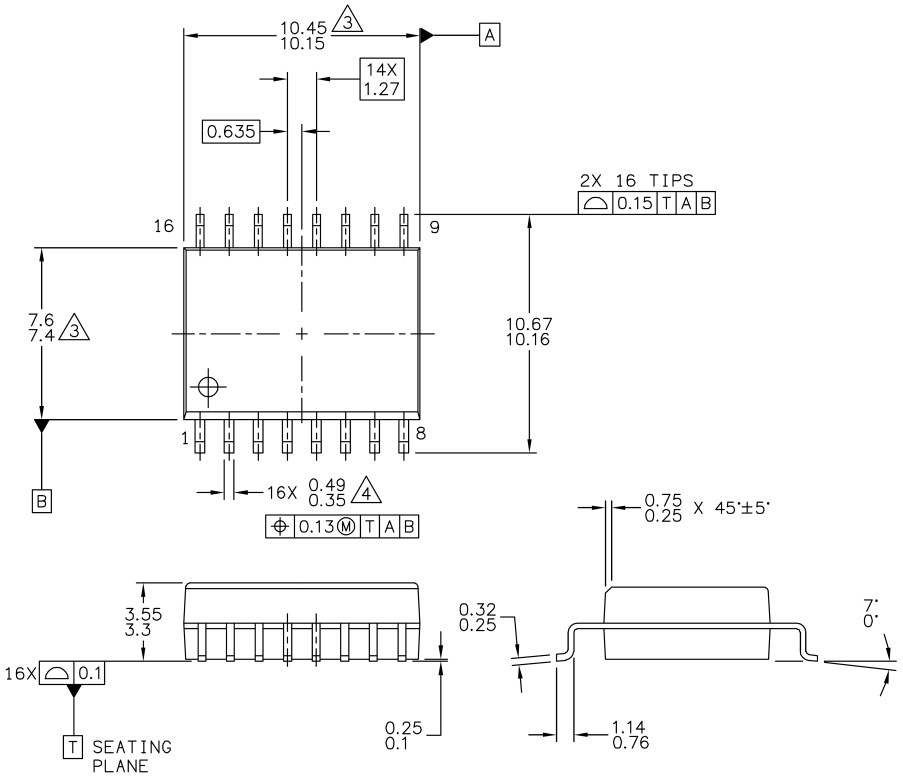

© FREESCALE SEMICONDUCTOR, INC. ALL RIGHTS RESERVED.	MECHANICAL OUTLINE	PRINT VERSION NOT TO SCALE
TITLE: 16 LEAD SOIC ACCELEROMETER	DOCUMENT NO: 98ASB16926C	REV: C
	CASE NUMBER: 475–01	17 MAR 2005
	STANDARD: NON–JEDEC	

PAGE 1 OF 2

CASE 475-01
ISSUE C
16-LEAD SOIC

MMA1213D

Figure C.8: Datasheet - MMA1213 - Page 08

PACKAGE DIMENSIONS

NOTES:

1. ALL DIMENSONS ARE IN MILLIMETERS.

2. INTERPRET DIMENSIONS AND TOLERANCES PER ASME Y14.5M–1994.

3. THESE DIMENSIONS DO NOT INCLUDE MOLD FLASH OR PROTRUSIONS. MOLD FLASH OR PROTRUSIONS SHALL NOT EXCEED 0.15 PER SIDE.

4. THIS DIMENSION DOES NOT INCLUDE DAMBAR PROTRUSION. PROTRUSIONS SHALL NOT CAUSE THE LEAD WIDTH TO EXCEED 0.75

MECHANICAL OUTLINE	PRINT VERSION NOT TO SCALE

TITLE:	DOCUMENT NO: 98ASB16926C	REV: C
16 LEAD SOIC ACCELEROMETER	CASE NUMBER: 475–01	17 MAR 2005
	STANDARD: NON–JEDEC	

PAGE 2 OF 2

CASE 475-01
ISSUE C
16-LEAD SOIC

MMA1213D

Figure C.9: Datasheet - MMA1213 - Page 09

How to Reach Us:

Home Page:
www.freescale.com

E-mail:
support@freescale.com

USA/Europe or Locations Not Listed:
Freescale Semiconductor
Technical Information Center, CH370
1300 N. Alma School Road
Chandler, Arizona 85224
+1-800-521-6274 or +1-480-768-2130
support@freescale.com

Europe, Middle East, and Africa:
Freescale Halbleiter Deutschland GmbH
Technical Information Center
Schatzbogen 7
81829 Muenchen, Germany
+44 1296 380 456 (English)
+46 8 52200080 (English)
+49 89 92103 559 (German)
+33 1 69 35 48 48 (French)
support@freescale.com

Japan:
Freescale Semiconductor Japan Ltd.
Headquarters
ARCO Tower 15F
1-8-1, Shimo-Meguro, Meguro-ku,
Tokyo 153-0064
Japan
0120 191014 or +81 3 5437 9125
support.japan@freescale.com

Asia/Pacific:
Freescale Semiconductor Hong Kong Ltd.
Technical Information Center
2 Dai King Street
Tai Po Industrial Estate
Tai Po, N.T., Hong Kong
+800 2666 8080
support.asia@freescale.com

For Literature Requests Only:
Freescale Semiconductor Literature Distribution Center
P.O. Box 5405
Denver, Colorado 80217
1-800-441-2447 or 303-675-2140
Fax: 303-675-2150
LDCForFreescaleSemiconductor@hibbertgroup.com

RoHS-compliant and/or Pb-free versions of Freescale products have the functionality and electrical characteristics of their non-RoHS-compliant and/or non-Pb-free counterparts. For further information, see http://www.freescale.com or contact your Freescale sales representative.

For information on Freescale's Environmental Products program, go to http://www.freescale.com/epp.

Information in this document is provided solely to enable system and software implementers to use Freescale Semiconductor products. There are no express or implied copyright licenses granted hereunder to design or fabricate any integrated circuits or integrated circuits based on the information in this document.

Freescale Semiconductor reserves the right to make changes without further notice to any products herein. Freescale Semiconductor makes no warranty, representation or guarantee regarding the suitability of its products for any particular purpose, nor does Freescale Semiconductor assume any liability arising out of the application or use of any product or circuit, and specifically disclaims any and all liability, including without limitation consequential or incidental damages. "Typical" parameters that may be provided in Freescale Semiconductor data sheets and/or specifications can and do vary in different applications and actual performance may vary over time. All operating parameters, including "Typicals", must be validated for each customer application by customer's technical experts. Freescale Semiconductor does not convey any license under its patent rights nor the rights of others. Freescale Semiconductor products are not designed, intended, or authorized for use as components in systems intended for surgical implant into the body, or other applications intended to support or sustain life, or for any other application in which the failure of the Freescale Semiconductor product could create a situation where personal injury or death may occur. Should Buyer purchase or use Freescale Semiconductor products for any such unintended or unauthorized application, Buyer shall indemnify and hold Freescale Semiconductor and its officers, employees, subsidiaries, affiliates, and distributors harmless against all claims, costs, damages, and expenses, and reasonable attorney fees arising out of, directly or indirectly, any claim of personal injury or death associated with such unintended or unauthorized use, even if such claim alleges that Freescale Semiconductor was negligent regarding the design or manufacture of the part.

Figure C.10: Datasheet - MMA1213 - Page 10

References

[1] Dhatt, G. and Touzot, G.: *The Finite Element Method Displayed*. John Wiley & Sons, 1985.

[2] Cook, R.D., Malkus, D.S. and Plesha, M.E.: *Concepts and Applications of Finite Element Analysis*. 3rd edn. John Wiley & Sons, 1989.

[3] Cook, R.: *Finite Element Modeling for Stress Analysis*. John Wiley & Sons, Inc., 1995.

[4] Akin, J.: *Application and Implementation of Finite Element Methods*. Academic Press, 1982.

[5] Heinze, S.: Aeroelastic concepts for flexible wing structures. Royal Institute of Technology, Stockholm, Sweden, 2005.

[6] Bispilinghoff, R. and Ashley, H.: *Principles of Aeroelasticity*. John Wiley & Sons, Inc, 1962.

[7] Schuster, D., Liu, D. and Huttsell, L.: Computational aeroelasticity: Success, progress, challenge. *Journal of Aircraft*, vol. 40, no. 5, pp. 843–856, Sep-Oct 2003.

[8] Dowell, E., Crawley, E., Curtis, H., Peters, D., Scanlan, R. and Sisto, F.: *A Modern Course in Aeroelasticity*. Kluwer Academic Publishers, London, 1995.

[9] Waszak, M. and Schmidt, D.: Flight dynamics of aeroelastic vehicles. *Journal of Aircraft*, vol. 25, no. 6, pp. 563–571, 1988.

[10] Hancock, G., Wright, J. and Simpson, A.: On the teaching of the principles of wing flexure-torsion. *Aeronautical Journal*, Oct 1985.

[11] Qin, Z. and Librescu, L.: Aeroelastic instability of aircraft wings modelled as anisotropic composite thin-walled beams in incompressible flow. *Journal of Fluids and Structures*, , no. 18, pp. 43–61, 2003.

[12] J.Cai, F.Liu, Zhu, Y., Tsai, H. and Wong, A.: Calculation of wing flutter by a coupled fluid-structure method. *Journal of Aircraft*, vol. 38, no. 2, pp. 334–342, March-April 2001.

[13] Garza, A. and Butuk, N.: Time marching kernel aprroximated pde solutions for mesh-free computational fluid dynamics. In: *The 2006 International Conference on Scientific Computing*. 2006.

[14] S'uli, E. and Mayers, D.: *An Introduction to Numerical Analysis*. Cambridge University PRess, 2003.

[15] Drela, M.: Method for simultaneous wing aerodynamic and structural load prediction. *Journal of Aircraft*, vol. 27, no. 8, pp. 692–699, 1990.

[16] Bertin, J.: *Aerodynamics for Engineers*. Prentice Hall. Fourth Edition.

[17] Karamcheti, K.: *Principles of Ideal-Fluid Aerodynamics*. John Wiley & Sons, Inc, 1966.

[18] Rodden, W., Harder, R. and Bellinger, E.: Aeroelastic addition to nastran. Tech. Rep. NAS1-13034, NASA Langley Research Center, 1979.

[19] Bookstein, F.: Principal warps: Thin-plate splines and the decomposition of deformations. *IEEE Transactions on Pattern Analysis and Machine Intelligence*, vol. II, no. 6, pp. 567 – 585, June 1989.

[20] Barnwell, W.: Distributed actuation and sensing on an uninhabited aerial vehicle. North Caolina State University, 2003.

[21] Bobbitt, P.: The pros and cons of code validation. Tech. Rep. NASA TM-100657, NASA Langley Research Center, July 1988.

[22] Ifju, P.: Experimental characterization of a flexible wing micro air vehicle. University of Florida.

[23] A.Pope and J.J.Harper: *Low-Speed Wind Tunnel Testing*. John Wiley and Sons, 1966.

[24] White, F.: *Fluid Mechanics*. McGraw Hill, 2003. Fifth Edition.

[25] Maritz, G., van Rooyen, G. and Heyman, F.: Sterkteleer 142-144. Universiteit van Stellenbosch, Departement Siviele Ingenieurswese, 2004.

[26] Clough, R. and Penzien, J.: *Dynamics of Structures*. McGraw-Hill, Inc., 1975.

[27] Qin, Z. and Librescu, L.: Dynamic aeroelastic response of aircraft wings modelled as anisotropic this-walled beams. *Journal of Aircraft*, vol. 40, no. 3, pp. 532–543, May-June 2003.

[28] Bhardwaj, M.: A cfd/csd interaction methodology fr aircraft wings. Tech. Rep. NASA-97-206181, Virginia Polytechnic Institute and State University, Oct 1997.

[29] Fenner, R.: *Finite Element Methods for Engineers*. The Macmillan Press Ltd, 1975.

[30] Ring, M.: Mapm, a portable arbitraty precision math library in c. *C/C++ Users Journal*, 2001. Http://www.tc.umn.edu/ ringx004/mapm-main.html.

[31] Cook, M.: *Flight Dynamics Principles*. 3rd edn. Elsevier.

[32] Neiswander, B.: Prandtl's lifting line theory and finite wings lab. University of Notre Dame, 2010.

[33] Houghton, E. and Carruthers, N.: *Aerodynamics for Engineering Students*. Arnold, 1982. Third Edition.

[34] Press, W., Teukolsky, A., Vetterling, W. and Flannery, B.: *Numerical Recipes in C*. The Art of Scientific Computing, 2nd edn. Cambridge University Press, 1992.

[35] Figliola, R. and Beasley, D.: *Theory and Design for Mechanical Measurements*. 4th edn. John Wiley & Sons, Inc, 2006.